UNDERSTANDING THE NATURE OF ULTRA-FAINT DWARF GALAXIES THROUGH CHARACTERIZATION AND STATISTICAL INFERENCE

A Dissertation

by

SARAH A. CANTU

Submitted to the Graduate and Professional School of
Texas A&M University
in partial fulfillment of the requirements for the degree of

DOCTOR OF PHILOSOPHY

Chair of Committee,	Louis E. Strigari
Committee Members,	Jennifer Marshall
	Jonelle Walsh
	Sherry Yennello
Head of Department,	Grigory Rogachev

August 2021

Major Subject: Astronomy

ABSTRACT

We present deep g- and r-band Magellan/Megacam photometry of two dwarf galaxy candidates discovered in the Dark Energy Survey (DES), Grus I and Indus II. For the case of Grus I, we resolved the main sequence turn-off (MSTO) and ~ 2 mags below it. The MSTO can be seen at $g_0 \sim 24$ with a photometric uncertainty of 0.03 mag. We show Grus I to be consistent with an old, metal-poor (~ 13.3 Gyr, [Fe/H]~ -1.9) dwarf galaxy. We derive updated distance and structural parameters for Grus I using this deep, uniform, wide-field data set. We find an azimuthally averaged half-light radius more than two times larger ($\sim 151^{+21}_{-31}$ pc; $\sim 4\farcm16^{+0.54}_{-0.74}$) and an absolute V-band magnitude ~ -4.1 that is ~ 1 magnitude brighter than previous studies.

Although our photometry of Indus II is $\sim 2-3$ magnitudes deeper than the DES Y1 Public release, we find no coherent stellar population at its reported location. The original detection was located in an incomplete region of sky in the DES Y2Q1 data set and was flagged due to potential blue horizontal branch member stars. The best fit isochrone parameters are physically inconsistent with both dwarf galaxies and globular clusters. We conclude that Indus II is likely a false-positive, flagged due to a chance alignment of stars along the line of sight.

We present updated structural parameters of 13 UFDs in the DES footprint. We use the final Y6 coadded DES data that has a limiting magnitude of $g \sim 24.7$. In all cases, where the UFD is resolved, it is consistent with an old, metal poor stellar population. Tuc II and Cet II are found to be larger than previously thought.

We also present the slope of the Initial Mass Function (IMF), α of two UFD in the DES footprint. Both Ret II and Tuc III are well populated ~ 3 magnitudes below the Main Sequence (MS). Reticulum II was found to have $\alpha = 1.68 \pm 0.5$ and Tucana III was found to have $\alpha = 1.56 \pm 0.8$. These findings contribute to the broader scope of expanding our ability to constrain the IMF with noisy data on low-mass objects.

DEDICATION

To my future and to my son's future.

ACKNOWLEDGMENTS

I would like to thank my family for their support during this time. It would have been nigh impossible to do this without babysitters and love. I would like to thank my cohort who never gave up on me and my advisor who continually lit a fire underneath me.

I would be remiss if I ignored the impact that James N. Chirdo has had in my life these past couple of years. Particularly, by providing the shocking motivation for an incredible, single-minded drive to push through, finish, and succeed—I will never settle for less than I am worth.

Most of all though, I would like to acknowledge that none of this would have happened had it not been for the motivation inspired by a 1-year old little boy that I wanted to do right by and that has been by my side no matter what comes our way.

I would like to acknowledge support from the Texas A&M University and the George P. and Cynthia Woods Institute for Fundamental Physics and Astronomy. This research made use of Astropy,[1] a community-developed core Python package for Astronomy (1; 2). This research made extensive use of arXiv.org and NASA's Astrophysics Data System for bibliographic information.

Funding for the DES Projects has been provided by the U.S. Department of Energy, the U.S. National Science Foundation, the Ministry of Science and Education of Spain, the Science and Technology Facilities Council of the United Kingdom, the Higher Education Funding Council for England, the National Center for Supercomputing Applications at the University of Illinois at Urbana-Champaign, the Kavli Institute of Cosmological Physics at the University of Chicago, the Center for Cosmology and Astro-Particle Physics at the Ohio State University, the Mitchell Institute for Fundamental Physics and Astronomy at Texas A&M University, Financiadora de Estudos e Projetos, Fundação Carlos Chagas Filho de Amparo à Pesquisa do Estado do Rio de Janeiro, Conselho Nacional de Desenvolvimento Científico e Tecnológico and the Ministério da Ciência, Tecnologia e Inovação, the Deutsche Forschungsgemeinschaft and the Collaborating Institutions in the Dark Energy Survey.

[1] http://www.astropy.org

The Collaborating Institutions are Argonne National Laboratory, the University of California at Santa Cruz, the University of Cambridge, Centro de Investigaciones Energéticas, Medioambientales y Tecnológicas-Madrid, the University of Chicago, University College London, the DES-Brazil Consortium, the University of Edinburgh, the Eidgenössische Technische Hochschule (ETH) Zürich, Fermi National Accelerator Laboratory, the University of Illinois at Urbana-Champaign, the Institut de Ciències de l'Espai (IEEC/CSIC), the Institut de Física d'Altes Energies, Lawrence Berkeley National Laboratory, the Ludwig-Maximilians Universität München and the associated Excellence Cluster Universe, the University of Michigan, the National Optical Astronomy Observatory, the University of Nottingham, The Ohio State University, the University of Pennsylvania, the University of Portsmouth, SLAC National Accelerator Laboratory, Stanford University, the University of Sussex, Texas A&M University, and the OzDES Membership Consortium.

Based in part on observations at Cerro Tololo Inter-American Observatory, National Optical Astronomy Observatory, which is operated by the Association of Universities for Research in Astronomy (AURA) under a cooperative agreement with the National Science Foundation.

The DES data management system is supported by the National Science Foundation under Grant Numbers AST-1138766 and AST-1536171. The DES participants from Spanish institutions are partially supported by MINECO under grants AYA2015-71825, ESP2015-66861, FPA2015-68048, SEV-2016-0588, SEV-2016-0597, and MDM-2015-0509, some of which include ERDF funds from the European Union. IFAE is partially funded by the CERCA program of the Generalitat de Catalunya. Research leading to these results has received funding from the European Research Council under the European Union's Seventh Framework Program (FP7/2007-2013) including ERC grant agreements 240672, 291329, and 306478. We acknowledge support from the Brazilian Instituto Nacional de Ciência e Tecnologia (INCT) e-Universe (CNPq grant 465376/2014-2).

CONTRIBUTORS AND FUNDING SOURCES

Contributors

This work was supported by a dissertation committee consisting of Professor Louis Strigari, Professor Jonelle Walsh, Professor Jennifer Marshall, and Professor Sherry Yennello of the Department of Physics and Astronomy and Professor Sherry Yennello of the Department of Chemistry.

The data analyzed for Chapter II was provided by Professor Marshall and Doctor Josh Simon. The observations were performed by Doctor Denija Crnojevic. The analysis and review of Chapter II and Chapter III underwent significant review by Doctor Andrew Pace and by the Dark Energy Survey Collaboration and the Milky Way Working Group.

Funding Sources

Graduate study was partially supported by a fellowship from Texas A&M University.

NOMENCLATURE

UFD	Ultra-faint Dwarf
GC	Globular Cluster
IMF	Initial Mass Function
CMD	Color-Magnitude Diagram
DES	Dark Energy Survey
HST	Hubble Space Telescope
MSTO	Main Sequence Turnoff
MS	Main Sequence
HB	Horizontal Branch
RGB	Red Giant Branch
SDSS	Sloan Digital Sky Survey
FOV	Field of View
MCMC	Markov Chain Monte Carlo
CDM	Cold Dark Matter
MW	Milky Way
PSF	Point-Spread Function
ROI	Region of Interest
RA	Right Ascension
PDF	Probability Distribution Function

TABLE OF CONTENTS

Page

ABSTRACT ii

DEDICATION iii

ACKNOWLEDGMENTS iv

CONTRIBUTORS AND FUNDING SOURCES vi

NOMENCLATURE vii

TABLE OF CONTENTS viii

LIST OF FIGURES x

LIST OF TABLES xvi

1. INTRODUCTION 1

    1.1 Ultra-faint Dwarf Galaxies 1
    1.2 Initial Mass Functions 2
    1.3 Characterization with Ground-based Data 3

2. GRUS I AND INDUS II 5

    2.1 Introduction 5
    2.2 Observations and Data Reduction 6
        2.2.1 Data 6
        2.2.2 Megacam Photometry 7
        2.2.3 DES Photometry 8
        2.2.4 Transformation from Megacam to DES 9
    2.3 Methods 13
    2.4 Results & Discussion 15
        2.4.1 Grus I 15
        2.4.2 Indus II 22

3. IMF ANALYSIS 24

    3.1 Introduction 24
    3.2 Data 25
        3.2.1 Simulated Data 26

3.2.2 Target Objects 30
3.3 Methods 33
3.3.1 Analysis 34
3.4 Results 36
3.4.1 Cetus II 38
3.4.2 Cetus III 39
3.4.3 Columba I 40
3.4.4 DES J0225+0304 41
3.4.5 Eridanus II 42
3.4.6 Eridanus III 43
3.4.7 Grus I 44
3.4.8 Grus II 45
3.4.9 Horologium I 46
3.4.10 Horologium II 47
3.4.11 Indus II 48
3.4.12 Kim 2 48
3.4.13 Phoenix II 49
3.4.14 Pictoris I 50
3.4.15 Reticulum II 51
3.4.16 Reticulum III 52
3.4.17 Tucana II 53
3.4.18 Tucana III 54
3.4.19 Tucana IV 55
3.4.20 Tucana V 56
3.5 Discussion 57

4. SUMMARY AND CONCLUSIONS 60

4.1 The Nature of UFD Candidates 60
4.2 Characterization of UFDs 61
4.3 Characterization of the IMF 62

REFERENCES 64

APPENDIX A. HESS CMDS 83

LIST OF FIGURES

FIGURE Page

2.1 Full $24' \times 24'$ FOV of Grus I (left panel) and Indus II (right panel). Shown here are the final SWarped and coadded r-band images with masks applied to saturated objects and satellite trails (white marks). The inner blue circles delineate the region of interest (ROI; see §2.3) defined in the statistical analysis used to determine final properties of each object. The outer circles mark the outer limit of the area designated as the background region in the statistical analysis. For both objects, the radii of the circles are $r_{\text{inner}} = 7\farcm2$ and $7\farcm2 \geq r_{\text{background}} \geq 12'$..... 6

2.2 Distribution of high confidence stars used in photometric transformation from Megacam instrumental magnitudes to the DES magnitude system. All four panels show $m_{DES} - m_{Megacam}$ vs. $g - r(Megacam)$, where $Megacam$ here are transformed into the DES system. The top two panels show Grus I (586 matched stars) and the bottom two panels show Indus II (1122 matched stars). For both objects, the green points represent g-band data and the red points represent r-band data. 9

2.3 g_0 vs. $(g_0 - r_0)$ CMDs of the full $24' \times 24'$ Megacam FOV centered on Grus I (left) and Indus II (right)—created with the final stellar Magellan/Megacam+DES catalog (where objects $g_0 18$ and $r_0 17.5$ are from DES). The error bars represent median photometric uncertainties for one-mag wide bins and are arbitrarily placed in color-space. 12

2.4 Posterior probability distributions for the structural and isochrone parameters of Grus I obtained from an elliptical Plummer model and grid of PARSEC isochrones. The parameters explored were (from left to right): stellar richness (λ), Δ R.A. & Δ Dec.(these are the shift from the centroid found in (3)), semi-major half-light radius (a_h), ellipticity (ϵ), position angle (ϕ), distance modulus ($(m - M)_0$), age (τ), and metallicity ([Fe/H]). Dashed lines in the 1D histograms indicate 16th, 50th, and 84th quantiles of the median peak likelihood. We have excluded these quantiles from $(m - M)_0$ and [Fe/H] due to their bimodality. 16

2.5 Shown as a red star are the position of Grus I with our newly derived properties (circled in red) and its original location in the size-luminosity plane. The original location of Indus II is shown as a light blue circle. The MW globular clusters are in grey points and the rest of the MW UFDs are depicted with blue crosses. 17

2.6 The top row of panels is for Grus I CMD and the bottom row is for Indus II CMD. In both cases, the 1st panel shows an ROI of $2 \times r_h$ centered on the object, where Grus I uses properties found in this study (see Table 2.5) and Indus II uses the discovery properties from (4). The 2nd panel is a comparison CMD made from stars $> 2 \times r_h$ away from the ROI. The 3rd panel is the Hess diagram of the stars within $2 \times r_h$ as seen in the 1st panel.The 4th panel is a Hess diagram showing the density of the background stars seen in the 2nd panel. They have been scaled to match the same area as the ROIs. The 5th panel is the Hess difference of the 4th and 3rd panels. 18

2.7 Right panel: Spatial distribution of stars in Grus I that have high membership probability. Middle Panel: Color-magnitude diagram of the same stars with high membership probability. The black line is the isochrone best described by our newly derived parameters in Table 2.5. Gray points in both panels are stars with less than 5% membership probability. Right panel: The stellar density profile of Grus I where the data is shown in red in elliptical bins of equal number and weighted by associated membership probabilities. The black dashed line shows the theoretical two-dimensional Plummer profile created with a Plummer-scale radius equal to $a_h = 5.6'$. 19

2.8 The $3-\sigma$ iso-density contours of Grus I with our redetermined centroid shown as a red star. The blue circles represent the location of the two overdensities mentioned in Jerjen et al. (5) and the gold diamond is the original centroid found in Koposov et al. (3). The yellow dashed ellipse indicates the Plummer halflight radius found in this work. 21

3.1 Example of simulated data created to test our ability to recover physical parameters and IMF slope. Additionally used to test observational limitations of IMF target candidates and determine proper magnitude, color, and spatial cuts for accurate characterization. 26

3.2 The leftmost panel has $M_V = -1$, the middle panel has $M_V = -2$, and the rightmost panel has $M_V = -3$. All other simulated physical properties are the same among all three panels. These were preliminary runs shown here to provide an example of the testing that was done with the simulated data. 28

3.3 Simulated datasets with all physical properties the same except for α. The panel on the left has $\alpha = 1.35$ and the figure on the right has $\alpha = 3.35$ It can be seen that morphological convergence (all other things being equal) is easier to achieve and more precise with a shallower slope. 29

3.4 Simulated data set with $alpha = 3.35$. This is an example of recovering the isochrone parameter values with a steeper slope. 30

3.5 Shown here are CMDs of all the confirmed and candidate UFDs from the DES footprint (6). The isochrone overlaid is a Dotter 2008 (7) of age 13.0 Gyr and $[Fe/h] = 2.34$, representative of typical UFD populations. The spread in the isochrone is an applied error function based on the Y6_GOLD data. 32

3.5 Continued 33

3.6 Comparing Dotter 2008 (7), Dotter 2016 (8), and Dotter 2016 downloaded from the website (8). The black dots are spectra from Simon et al. (9). 35

3.7 Posterior probability distributions for the structural and isochrone parameters of Cetus II obtained from an elliptical Plummer model and grid of PARSEC isochrones. The parameters explored were (from left to right): stellar richness (λ), Δ R.A. & Δ Dec. (these are the shifts from the centroid found in the literature), semi-major half-light radius (a_h), ellipticity (ϵ), position angle (ϕ). Dashed lines in the 1D histograms indicate 16th, 50th, and 84th quantiles of the median peak likelihood. The red lines represent current literature values. 38

3.8 Posterior probability distributions for the structural and isochrone parameters of Cetus III. This figure is similar to Figure 3.7 39

3.9 Posterior probability distributions for the structural and isochrone parameters of Columba I. This figure is similar to Figure 3.7 40

3.10 Posterior probability distributions for the structural and isochrone parameters of DES J0225+0304. This figure is similar to Figure 3.7 41

3.11 Posterior probability distributions for the structural and isochrone parameters of Eridanus II. This figure is similar to Figure 3.7 42

3.12 Posterior probability distributions for the structural and isochrone parameters of Eridanus III. This figure is similar to Figure 3.7 43

3.13 Posterior probability distributions for the structural and isochrone parameters of Grus I. This figure is similar to Figure 3.7 44

3.14 Posterior probability distributions for the structural and isochrone parameters of Grus II. This figure is similar to Figure 3.7 45

3.15 Posterior probability distributions for the structural and isochrone parameters of Horologium I. This figure is similar to Figure 3.7 46

3.16 Posterior probability distributions for the structural and isochrone parameters of Horologium II. This figure is similar to Figure 3.7 47

3.17 Posterior probability distributions for the structural and isochrone parameters of Indus II. This figure is similar to Figure 3.7 48

3.18 Posterior probability distributions for the structural and isochrone parameters of Kim 2. This figure is similar to Figure 3.7 49

3.19 Posterior probability distributions for the structural and isochrone parameters of Phoenix II. This figure is similar to Figure 3.7 50

3.20 Posterior probability distributions for the structural and isochrone parameters of Pictoris I. This figure is similar to Figure 3.7 51

3.21 Posterior probability distributions for the structural and isochrone parameters of Reticulum II. This figure is similar to Figure 3.7 with the addition of the free parameter α, the slope of the IMF. 52

3.22 Posterior probability distributions for the structural and isochrone parameters of Reticulum III. This figure is similar to Figure 3.7 53

3.23 Posterior probability distributions for the structural and isochrone parameters of Tucana II. This figure is similar to Figure 3.7 54

3.24 Posterior probability distributions for the structural and isochrone parameters of Reticulum II. This figure is similar to Figure 3.7 with the addition of the free parameter α, the slope of the IMF. 55

3.25 Posterior probability distributions for the structural and isochrone parameters of Tucana IV. This figure is similar to Figure 3.7 56

3.26 Posterior probability distributions for the structural and isochrone parameters of Tucana V. This figure is similar to Figure 3.7 57

3.27 The difference between all of the objects listed in Table 3.3 and their original literature values. For readability, only a_h (the black dots), M_V (the blue star), and D (the distance in kpc, the red plus) are listed here. 58

3.28 Comparison of all the dwarf galaxies with IMF measurements (power-law form). The dashed line is the Salpeter IMF. 59

3.29 IMF slope vs. average metallicity of all the dwarf galaxies with IMF measurements (power-law form). 59

A.1 The left panel is a binned CMD of Cetus II within a ROI of $2r_h$. The middle panel is a binned CMD of the background nearby. The right panel is a background subtracted Hess color magnitude diagram. The dashed line represents an old, metal poor Dotter 2008 isochrone and the red lines are DES Y6_GOLD representative spread due to photometric uncertainty. 83

A.2 A background subtracted Hess color magnitude diagram of Cetus III. This figure is similar to Figure A.1 84

A.3 A background subtracted Hess color magnitude diagram of Columba I. This figure is similar to Figure A.1 84

A.4 A background subtracted Hess color magnitude diagram of DES 0225 0304. A background subtracted Hess color magnitude diagram of Columba I. This figure is similar to Figure A.1 85

A.5 A background subtracted Hess color magnitude diagram of Eridanus II. This figure is similar to Figure A.1 85

A.6 A background subtracted Hess color magnitude diagram of Eridanus III. This figure is similar to Figure A.1 86

A.7 A background subtracted Hess color magnitude diagram of Grus I. This figure is similar to Figure A.1 86

A.8 A background subtracted Hess color magnitude diagram of Grus II. This figure is similar to Figure A.1 87

A.9 A background subtracted Hess color magnitude diagram of Horologium I. This figure is similar to Figure A.1 87

A.10 A background subtracted Hess color magnitude diagram of Horologium II. This figure is similar to Figure A.1 88

A.11 A background subtracted Hess color magnitude diagram of Indus II. This figure is similar to Figure A.1 88

A.12 A background subtracted Hess color magnitude diagram of Indus II. This figure is similar to Figure A.1 89

A.13 A background subtracted Hess color magnitude diagram of Phoenix II. This figure is similar to Figure A.1 89

A.14 A background subtracted Hess color magnitude diagram of Pictoris I. This figure is similar to Figure A.1 90

A.15 A background subtracted Hess color magnitude diagram of Reticulum II. This figure is similar to Figure A.1 90

A.16 A background subtracted Hess color magnitude diagram of Reticulum III. This figure is similar to Figure A.1 91

A.17 A background subtracted Hess color magnitude diagram of Tucana II. This figure is similar to Figure A.1 91

A.18 A background subtracted Hess color magnitude diagram of Tucana III. This figure is similar to Figure A.1 92

A.19 A background subtracted Hess color magnitude diagram of Tucana IV. This figure is similar to Figure A.1 92

A.20 A background subtracted Hess color magnitude diagram of Tucana V. This figure is similar to Figure A.1 93

LIST OF TABLES

TABLE Page

2.1 Observing log of Magellan/Megacam observations in the g- and r-bands for Grus I and Indus II. 7

2.2 The photometric transformations between Megacam instrumental magnitudes and the DES photometric system. The fifth column displays the difference between the transformed Megacam magnitudes and the DES magnitudes. The sixth (sharp range) and seventh (median chi-value) columns detail the morphological cuts made on the instrumental photometry. The last two columns detail the number of stars and magnitude range of the final Megacam+DES stellar catalogs after these cuts were applied. The median absolute standard deviation of the difference between DES magnitudes and transformed Megacam magnitudes. The faint magnitude limits correspond to $S/N \sim 5$ 10

2.3 The final calibrated stellar catalog for Grus I—Sorted by star ID. This table is published in its entirety in machine-readable format. A portion is shown here for guidance regarding its form and content. All magnitudes are in the DES magnitude system. 11

2.4 The final calibrated stellar catalog for Indus II—Sorted by star ID. This table is published in its entirety in machine-readable format. A portion is shown here for guidance regarding its form and content. 12

2.5 Photometric and spectroscopic parameters of Grus I and Indus II found in the literature prior to this work. The columns for Grus I, in order, are from this work, (3; 10; 5; 11; 12; 13). Column 8 describes Indus II as found in the discovery paper, (4). 23

3.1 An example of a simulated stellar catalog—sorted by star ID. This table is published in its entirety in machine-readable format. A portion is shown here for guidance regarding its form and content. All magnitudes are in the DES magnitude system. 27

3.2 20 targets 31

3.3 Listed here are the results of refitting objects with Y6_GOLD data. 37

1. INTRODUCTION

1.1 Ultra-faint Dwarf Galaxies

With the advent of high-precision, large-area surveys such as SDSS (14), the Dark Energy Survey (DES) (15), Pan-STARRS (16), the Hyper Suprime-Cam Subaru Strategic Program (HSC SSP) (17), MagLites (18), and DELVE (19), the number of known faint satellite systems that orbit the Milky Way (MW) has dramatically increased (4; 3; 20). The ambiguity of what constitutes a galaxy increases as more systems are discovered that lie between the traditional loci of globular clusters and galaxies. Additionally, these low-luminosity systems challenge spectroscopic studies due to their low number of bright member stars (21).

Many of these satellites discovered in the past decade are categorized as ultra-faint dwarf (UFD) galaxies (22). With $M_V \gtrsim -8\,\mathrm{mag}$ ($\mathrm{M}_* \lesssim 10^5\,\mathrm{M}_\odot$) (23; 24), UFDs overlap with bright globular clusters (GCs) in the size-luminosity plane. Though they overlap in this parameter space, UFDs and GCs likely have different formation mechanisms (25). From their internal stellar kinematics, GCs are consistent with having little or no dark matter, and may be remnants of nucleated dwarf galaxies or may follow a completely separate evolutionary path (26).

In contrast, the stellar kinematics of UFDs exhibit high M/L_V ratios i.e.,, ($M/L_V \sim 10^3$) (27) and represent the faintest end of the galaxy luminosity function. Dynamical mass measurements are one of the primary distinguishing characteristics between UFDs and GCs. In comparison to low-luminosity GCs, UFDs have larger sizes ($r_h \gtrsim 30$ pc), larger velocity dispersions ($\sigma \gtrsim 3\,\mathrm{km\,s^{-1}}$), and significant metallicity spreads ($\sigma_{[Fe/H]} \gtrsim 0.3$ dex), as shown in (27) and (28).

As the most dark matter dominated objects visible in the Universe, UFDs provide crucial, empirical information about the nature of dark matter and hierarchical structure at the smallest-scales (29; 24). In λ-cold dark matter (λCDM) cosmology, structure forms hierarchically, with the UFDs corresponding to the galaxies in the smallest of dark matter halos (30; 31; 32). Discerning the exact nature of MW satellites is therefore our paramount observational method to better

constrain and compare cosmological models to low-luminosity systems. Firmly establishing the newly-discovered satellites as UFDs, and measuring their mass-to-light ratios, requires spectroscopic studies of a significant sample of their stars (33).

However, due to the faintness of these systems, spectroscopy is only possible for a small sample of their stars, making a robust determination of their mass-to-light ratios difficult to obtain. In addition to spectroscopic studies, information on the structural parameters and stellar populations of UFDs may be obtained through deep photometric studies. For faint overdensities of stars like UFDs, this requires targeted imaging and precise photometry, in order to distinguish members of the systems from background stars and galaxies (23; 34; 35; 36; 24; 5; 37).

1.2 Initial Mass Functions

An Initial Mass Function (IMF) describes the number of stars as a function of stellar mass for a simple stellar population. A star's mass is critical to understanding its location along a representative isochrone. In order to accurately infer properties of and assign membership to observed stellar systems, we must also understand the distribution of stellar masses along their evolutionary path.

In 1955, Salpeter et al. (38), determined a universal power-law IMF that well described the distribution of massive stars in the Milky Way (MW). This IMF form can be parameterized in terms of the slope, α, as

$$\xi(m) = dN/dm \propto m^{-\alpha}, \tag{1.1}$$

where $\alpha = 2.35$ for the classic Salpeter IMF.

Studies of the MW have shown that the IMF flattens out below $0.4\,\mathrm{M}_{\odot}$ giving evidence to the need for another form to describe the behavior of an IMF. Kroupa describes the MW IMF with a broken power law (39) . They found a slope of $\alpha = 2.3$ for $M > 0.5\,\mathrm{M}_{\odot}$ (close to the Salpeter slope) and $\alpha = 1.3$ for $M < 0.5\,\mathrm{M}_{\odot}$. Chabrier further modified the IMF parameterization to include a log-normal distribution below $1\,\mathrm{M}_{\odot}$ (40; 41).

Studies of the MW field and GCs point toward a universal IMF that is well described by the three previously mentioned IMF forms. However, complementary extra-galactic studies have

shown potentially steeper IMF slopes for giant elliptical galaxies (42; 43; 44).

These results hint at a non-universal IMF over different mass regimes. This points toward the need for local, resolved studies of lower mass systems to explore any potential trends in mass correlations. Studying resolved systems also avoids modeling assumptions that are required for unresolved studies and various degeneracies that can arise.

Local studies have been done with data taken with the Hubble Space Telescope (HST) of MW satellites and the Magellanic Clouds. Space-based imaging allows for deep photometry of local, resolved objects. Unlike extra-galactic studies (which focus on massive stars), HST imaging can probe a few magnitudes below the MSTO of local UFDs. This magnitude range can span a mass range, for $[Fe/H] < -1$, of between 0.2 and $0.7\,\mathrm{M}_{\odot}$, exploring the faint end of the IMF.

It's beneficial to study UFDs because they have relaxation times longer than a Hubble time and so they don't require dynamical evolution corrections. This is important because dynamical evolution (mass segregation and evaporation) can change the slope (45)—implying that the current mass function should be very similar, if not the same as the IMF. UFDs provide an excellent counterpoint to the MW field, GCS, and extragalactic IMF studies because of how different the galaxies are from the MW and larger extragalactic galaxies.

1.3 Characterization with Ground-based Data

Recently, large-area, ground-based surveys have achieved deeper and more precise photometry than was previously available. The purpose of the Dark Energy Survey (DES) is to explore and constrain the nature of dark energy. In order to do this, a major focus of the collaboration has been to create extremely precise photometry. By the last year of the program, DES has $\sim 76,200$ exposures across all five visible bands ($grizY$) and achieves a signal-to-noise (S/N) of 10 at a depth of $g \sim 24.7$ and $r \sim 24.4$.

With a combination of wide-field, deep data and statistical inference, we can infer the physical properties of UFDs. In this work we seek to clarify the nature of two objects detected in the DES footprint, Grus I and Indus II, with deep Magellan/Megacam imaging. Here we also contribute these local studies by analyzing all the UFDs and UFD candidates in the DES footprint (~ 20

objects) (6). We are able to provide IMF constraints on two of these UFDs, updated parameters on 13, and find agreement with 2 objects not being UFDs.

In Chapter 2, the analysis for Grus I and Indus II is detailed. This chapter is where the most details are presented about the statistical analysis done as it was the first study. In Chapter 3, I will present the results of a similar analysis on all the UFDs in the DES footprint using the latest DES coadded catalog. I will also present the results of the updated analysis to include constraints on the slope of the IMF of two UFDs. In Chapter 4, a summary of the results from both studies and their impact on the astronomical community is discussed.

2. GRUS I AND INDUS II

2.1 Introduction

Grus I was discovered by Koposov et al. (3), however its status as a GC or UFD has not yet been totally disentangled due to its faintness ($M_V = -3.4$) and the lack of deep, wide field photometry. Follow-up studies based on the deep but small Gemini/GMOS-S field of view (FOV) photometry (5) were not able to determine the properties of Grus I because of its extension ($r_h = 1\farcm77$) (3).

Martinez et al. obtained a precise distance to Grus I of $D_\odot = 127 \pm 6$ kpc ($\mu_0 = 20.51 \pm 0.10$ mag) from the detection of two RR Lyrae members (13). They find that this distance would imply a change of 5% in its previously calculated physical size, consistent with the estimate of Koposov et al. (3). Given the large uncertainties in the previous determinations of physical size, deep and extended imaging in Grus I is needed to firmly confirm this.

Complementary spectroscopic studies made of this system (10; 12) were not able to decipher the nature of this object either, since the velocity dispersion could not be resolved because of the scarce sample of members detected.

Our second target, Indus II, was identified in Bechtol et al. (4) as a low-confidence UFD candidate and will be referred to as Indus II throughout the paper for convenience. The initial data for Indus II were located in a survey region with atypical non-uniformity as they were taken part-way through the survey observations. The primary evidence for candidacy stems from a clump of apparent blue horizontal branch (BHB) stars at $g \sim 22$. While Indus II has been targeted in some dark matter indirect detection analyses (46), there are no other studies confirming the nature of the object. Given the uncertainty associated with this system, we chose to confirm whether this target was a gravitationally bound system due to Magellan/Megacam's FOV potentially covering $3 \times r_h$ (4).

We follow similar methods to other studies that have confirmed the status of many MW satellites as dwarf galaxies (47; 48; 49; 50; 51; 36; 52; 53; 54). Our data complements other studies

by utilizing a larger FOV (necessary for the potentially larger extents), while still resolving magnitudes ~ 3 magnitudes deeper than the discovery papers.

2.2 Observations and Data Reduction

2.2.1 Data

We observed Indus II and Grus I over four nights in April 2017 with the Megacam instrument (55) at the $f/5$ focus of the 6.5 m Magellan Clay telescope. Megacam is an imager composed of 36 CCDs of 2048×4608 pixels, creating a square array with a FOV of $\sim 24' \times 24'$ (see Figure 2.1). The data were binned 2×2 resulting in a pixel scale of $0\overset{''}{.}16$. Observations were dithered such that each image is offset by $+5''$ in right ascension (RA) and $+13''$ in declination (Dec.) from the previous one. This reduces the impact of the small gaps between the CCDs.

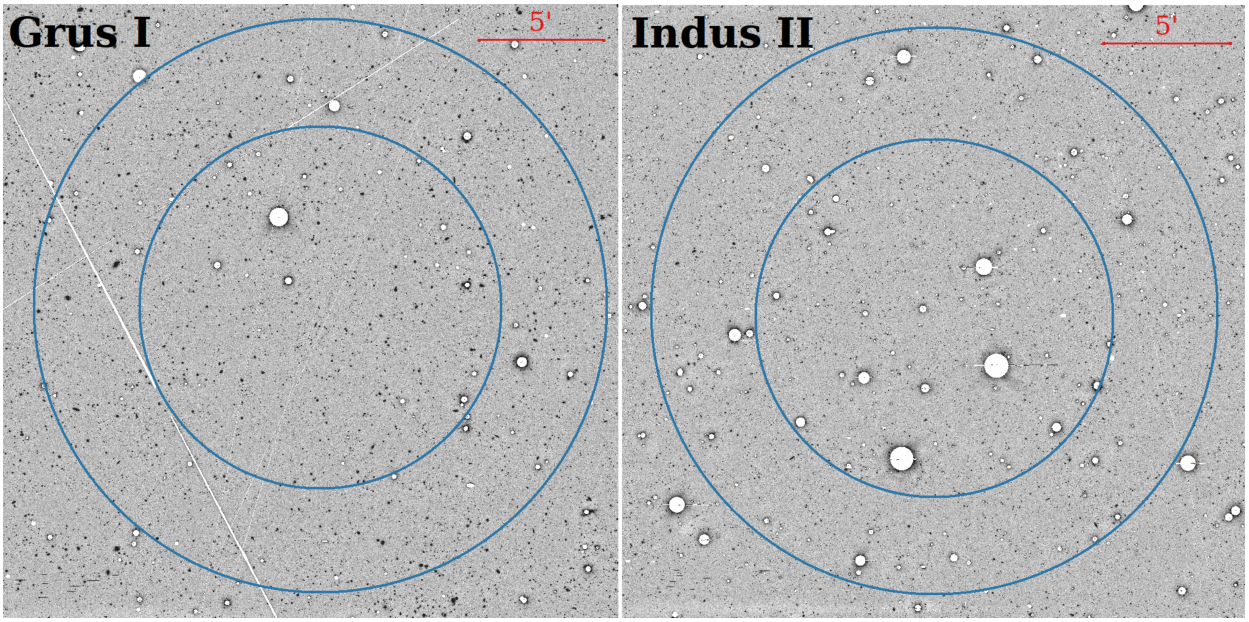

Figure 2.1: Full $24' \times 24'$ FOV of Grus I (left panel) and Indus II (right panel). Shown here are the final SWarped and coadded r-band images with masks applied to saturated objects and satellite trails (white marks). The inner blue circles delineate the region of interest (ROI; see §2.3) defined in the statistical analysis used to determine final properties of each object. The outer circles mark the outer limit of the area designated as the background region in the statistical analysis. For both objects, the radii of the circles are $r_{\text{inner}} = 7\overset{'}{.}2$ and $7\overset{'}{.}2 \geq r_{\text{background}} \geq 12'$.

The data were reduced using the Megacam pipeline developed at the Harvard-Smithsonian Center for Astrophysics[1] (56). This pipeline includes tasks such as bias subtraction, flat fielding, and cosmic ray correction. In addition, the pipeline derives astrometric solutions using the 2MASS survey (57). The images were then resampled, with a `lanczos3` interpolation function, and combined with a weighted average using `SWarp` (58). This process produced a final, stacked g- and r-band image for each object. An observing log can be found in Table 2.1.

Table 2.1: Observing log of Magellan/Megacam observations in the g- and r-bands for Grus I and Indus II.

Object	UT Date	Filter	$N \times t_{exp}$ (s)	Seeing ($''$)
Grus I	2017 Apr 23	g	7×300	0.7
	2017 Apr 24	r	8×300	0.9
Indus II	2017 Apr 21	g	8×300	0.6
	2017 Apr 22	r	8×300	0.5

2.2.2 Megacam Photometry

Due to the large FOV and number of objects in each image, we used point-spread function (PSF) fitting software to extract the stellar photometry. We used the well-known photometry package, `DAOPHOT`/`ALLSTAR` and `ALLFRAME`, and followed the general guidelines as described in various other papers to determine instrumental magnitudes (59**?**).

An accurate PSF model was created from the brightest and most isolated unsaturated stars in the image. An initial coordinate list and aperture photometry pass of each image was done to find appropriate stars to be used in creating the PSF models. We chose 500 of the brightest stars, evenly distributed over the image, and visually inspected the surrounding areas and radial profiles for saturation, neighbors, bad pixels, and other effects that might affect the measurement of an object.

[1]This paper uses data products produced by the OIR Telescope Data Center, supported by the Smithsonian Astrophysical Observatory.

In order to represent stars over the entire FOV, we ensured that the remaining stars were distributed over the entire image and allowed the PSF to vary quadratically. It should be noted that due to the elongation of objects in the Grus I g-band image, the fitting radius was set to be slightly larger than the FWHM to better encompass the core of the star. The elongation is along the East-West axis and likely due to tracking issues.

In order to create a final coordinate list, `ALLSTAR` was used twice to perform preliminary PSF photometry on the images. The first run produced a star-subtracted image on which `ALLSTAR` was run the second time and the stars used in the psf-fit and neighbors were visually inspected. This allows for the detection of fainter objects, located in the PSF wings of brighter objects. The resultant object list is then input to `ALLFRAME` to perform a final round of PSF photometry on each filter simultaneously. In order to convert pixel coordinates from one filter to another, `DAOMATCH/DAOMASTER` is used to find a linear transformation between the g- and r-bands for each image. This last step creates a final catalog in each filter that is matched by object ID. It also mitigates the systematic uncertainty created by blended stars being inaccurately measured as one star in some frames.

2.2.3 DES Photometry

We used DES photometry to transform Megacam instrumental magnitudes to DES standard magnitudes and to find magnitudes for the stars saturated in Megacam. DES is a wide-field survey imaging 5000 deg^2 of the southern hemisphere (15). DES uses the Dark Energy Camera (DECam (60)) positioned at the prime focus of the 4-meter Blanco telescope at the Cerro Tololo Inter-American Observatory (CTIO) in Chile. DES data are reduced by the DES Data Management (DESDM) pipeline; in which they are detrended, astrometrically calibrated to 2MASS, and coadded into image tiles (61). Detrending includes standard bias subtraction, CCD cross talk, flat fielding, and non-linearity, pupil, fringe, and illumination corrections. Object detection, photometric, and morphological measurements were performed with `SExtractor` followed by multi-epoch and single-object fitting (SOF) (62).

The DES catalogs used in this work were created from the DES Y3 GOLD (v2.0) catalog

with the selection flags FLAGS_GOLD$= 0$ and EXTENDED_CLASS_MASH_SOF≤ 2 in order to ensure we have a complete stellar sample with minimal contaminants. The FLAGS_GOLD selection applies a bitmask for objects that have known photometric issues and artifacts. The EXTENDED_CLASS_MASH_SOF is similar to the extended classification variables defined in Equations 1, 2, and 3 in Shipp et al. (63), but for the SOF photometry. The variables in these equations classify objects as high-confidence stars, low-confidence stars, and low-confidence galaxies.

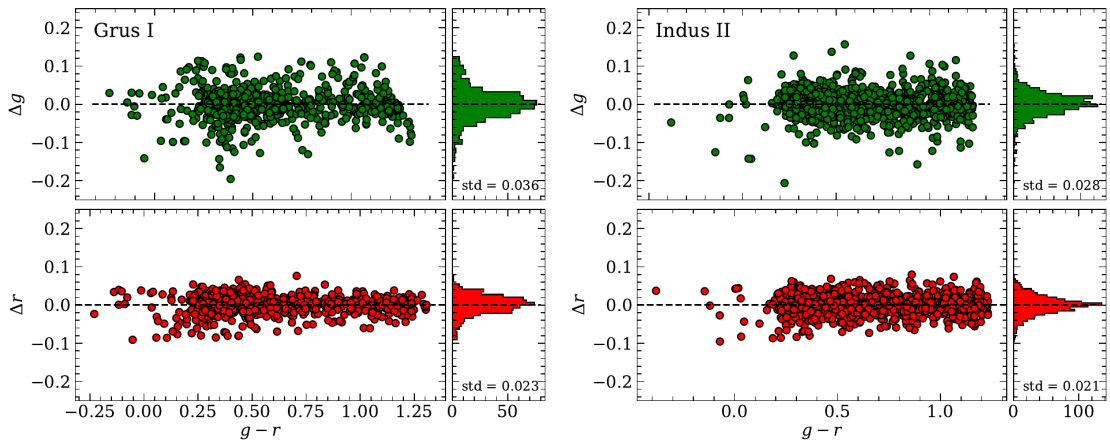

Figure 2.2: Distribution of high confidence stars used in photometric transformation from Megacam instrumental magnitudes to the DES magnitude system. All four panels show $m_{DES} - m_{Megacam}$ vs. $g - r(Megacam)$, where $Megacam$ here are transformed into the DES system. The top two panels show Grus I (586 matched stars) and the bottom two panels show Indus II (1122 matched stars). For both objects, the green points represent g-band data and the red points represent r-band data.

2.2.4 Transformation from Megacam to DES

The matched objects found in the previous section were used to find a transformation between DES magnitudes and Megacam instrumental magnitudes. A color cut of $(g_0 - r_0)_{DES} < 1.2$ was applied to remove a clump of M0 and redder stars. We used only stars having DES photometric errors less than 0.03 mag. These criteria ensure that a high-quality stellar sample is utilized in finding the magnitude system transformation.

To perform this transformation, we solve for the coefficients of the following equation using a generalized least squares regression:

$$M_{DES} = m_{instr} + \beta + \alpha(g_0 - r_0)_{DES}, \tag{2.1}$$

where β is the zeropoint offset and α is the color coefficient. To find the true distribution of $M_{DES} - m_{instr}$, we run the catalog through a sigma-clipping algorithm based on the median absolute deviation. Stars that lie outside 3σ are clipped until the distribution converges. Equation 2.1 is then applied to all of the instrumental magnitudes found from `ALLFRAME`. A second-order fit was explored and deemed unnecessary. The coefficients of this fit are in the third and fourth columns in Table 2.1 and the difference between transformed Megacam magnitudes and DES magnitudes of stars used to find the transformation can be seen in Figure 2.2.

Table 2.2: The photometric transformations between Megacam instrumental magnitudes and the DES photometric system. The fifth column displays the difference between the transformed Megacam magnitudes and the DES magnitudes. The sixth (sharp range) and seventh (median chi-value) columns detail the morphological cuts made on the instrumental photometry. The last two columns detail the number of stars and magnitude range of the final Megacam+DES stellar catalogs after these cuts were applied. The median absolute standard deviation of the difference between DES magnitudes and transformed Megacam magnitudes. The faint magnitude limits correspond to $S/N \sim 5$

Object	Filter	β	α	std(Δ_{mag})	Sharp	Chi	# of stars	Mag range
Grus I	g	7.554	-0.136	0.036	$(-0.7, 1.2)$	1.65	6743	$(15.6, 26.7)$
	r	7.651	-0.027	0.023	$(-0.5, 0.7)$	1.25	6743	$(15.2, 26.3)$
Indus II	g	7.596	-0.167	0.028	$(-0.5, 0.3)$	2.05	5520	$(15.2, 26.6)$
	r	7.657	-0.029	0.021	$(-0.7, 0.2)$	4.91	5520	$(14.8, 26.8)$

We created the final stellar catalog by applying morphological cuts using the statistics *sharp* and χ which were determined during the PSF fitting. *Sharp* can be approximated as *sharp*$^2 \sim \sigma^2_{obs} - \sigma^2_{PSF}$, where σ_{obs} is the observed photometric error and σ_{PSF} is the expected photometric

error (59).

The second statistic, χ, is the ratio of observed pixel-to-pixel scatter over expected scatter, determined from the intrinsic scatter in the PSF models. Star galaxy separation begins to break down at fainter magnitudes, i.e., $g_0 \sim 25.5$ and $r_0 \sim 24.75$. The details of these cuts and the magnitude range of the final stellar catalogs can be found in the last four columns in Table 2.2. In addition, the final catalog's brighter magnitudes are supplemented by the DES stellar objects where Megacam saturates at $g_0 \sim 18$ and $r_0 \sim 17.5$. A portion of these catalogs can be seen in Tables 2.3 and 2.4.

Table 2.3: The final calibrated stellar catalog for Grus I—Sorted by star ID. This table is published in its entirety in machine-readable format. A portion is shown here for guidance regarding its form and content. All magnitudes are in the DES magnitude system.

Star ID	R.A. (deg)	Dec. (deg)	$g_{0,DES}$ (mag)	σ_g (mag)	$r_{0,DES}$ (mag)	σ_r (mag)
12543	344.134	−50.285	25.398	0.106	24.807	0.068
12845	344.139	−50.284	22.623	0.007	22.402	0.007
13343	344.138	−50.281	24.075	0.029	24.044	0.036
14597	344.103	−50.278	24.745	0.047	24.361	0.049
14730	344.168	−50.278	24.956	0.070	24.902	0.076
15406	344.187	−50.275	17.679	0.003	17.276	0.002

Figure 2.3 shows the color-magnitude diagrams (CMDs) created for both Grus I and Indus II using the final calibrated stellar catalog as it was described in this section. The uncertainties show that the photometric signal-to-noise ~ 10 to a depth ~ 3 magnitudes below that of the discovery papers.

Table 2.4: The final calibrated stellar catalog for Indus II—Sorted by star ID. This table is published in its entirety in machine-readable format. A portion is shown here for guidance regarding its form and content.

Star ID	R.A. (deg)	Dec. (deg)	$g_{0,DES}$ (mag)	σ_g (mag)	$r_{0,DES}$ (mag)	σ_r (mag)
17138	309.735	−46.284	25.845	0.125	25.532	0.090
17539	309.705	−46.283	25.911	0.117	25.658	0.100
17819	309.691	−46.282	21.532	0.007	20.891	0.006
18608	309.677	−46.278	21.129	0.005	20.183	0.010
18821	309.764	−46.278	25.005	0.064	24.897	0.052
19208	309.689	−46.276	21.143	0.006	20.198	0.010

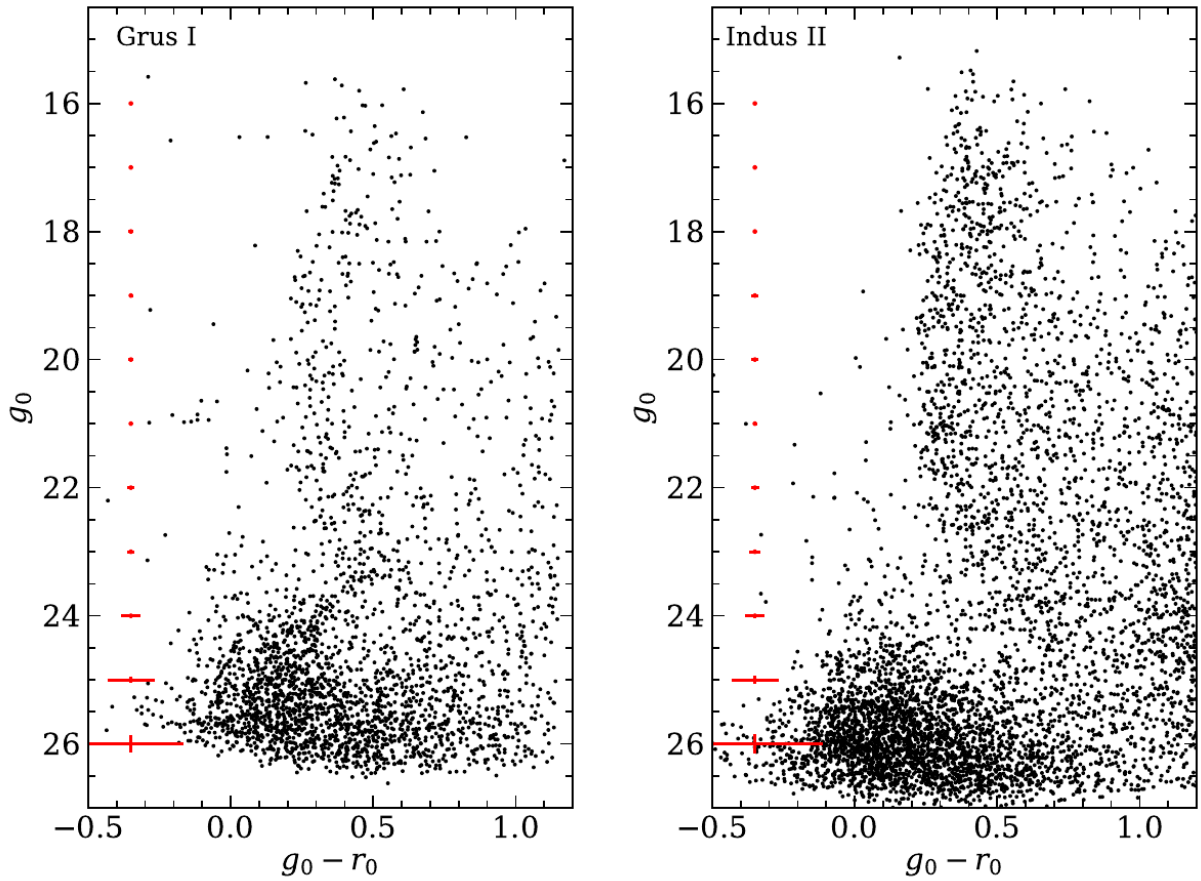

Figure 2.3: g_0 vs. $(g_0 - r_0)$ CMDs of the full $24' \times 24'$ Megacam FOV centered on Grus I (left) and Indus II (right)—created with the final stellar Magellan/Megacam+DES catalog (where objects $g_0 18$ and $r_0 17.5$ are from DES). The error bars represent median photometric uncertainties for one-mag wide bins and are arbitrarily placed in color-space.

2.3 Methods

We utilize the Ultra-faint Galaxy Likelihood toolkit to determine structural parameters and the best-fitting isochrones for Grus I and Indus II. Here we review the aspects of `UGaLi` that are important for our analysis, and refer to (20) and the appendix of (6) for a more detailed description.

Our data sample consists of the magnitude and the error on the magnitude in two filters, $\mathcal{D}_{c,i} = \{g_i, \sigma_{g_i}, r_i, \sigma_{r_i}\}$, and the spatial positions of the stars $\mathcal{D}_{s,i} = \{\alpha_i, \delta_i\}$. We define the probability distribution for the structural parameters as u_s, and the probability distribution for the parameters of the isochrone as u_c. The total probability distribution function (PDF) for the data $\mathcal{D}_i = \{\mathcal{D}_{s,i}, \mathcal{D}_{c,i}\}$ given the model parameters θ is then

$$u(\mathcal{D}_i\theta) = u_s(\mathcal{D}_{s,i}\theta_s) \times u_c(\mathcal{D}_{c,i}\theta_c), \tag{2.2}$$

This probability distribution is defined such that the integral of it over the entire spatial and magnitude domain is unity.

For the structural properties, u_s, we assume an elliptical Plummer model, with a projected density distribution (64; 23),

$$\Sigma(R) \propto \left[1 + \left(\frac{R_i}{R_p}\right)^2\right]^{-2}. \tag{2.3}$$

Here R_i is the elliptical radius coordinate from the center of the galaxy, and R_p is the Plummer-scale radius (equivalent to the 2D azimuthally averaged half-light radius, $r_h = a_h\sqrt{1-\epsilon}$). There are five model parameters that describe the Plummer profile: the centroid coordinates (α_0, δ_0,), the semi-major half-light radius (a_h), the ellipticity (ϵ), and position angle (ϕ). The density distribution is further related to spatial position by

$$R_i = \left\{ \left[\frac{1}{1-\epsilon}\left(X_i\cos\phi - Y_i\sin\phi\right)\right]^2 - \left(X_i\sin\phi + Y_i\cos\phi\right)^2 \right\}^{\frac{1}{2}} \tag{2.4}$$

and spatial position is related to the object centroid by

$$X_i - X_0 = (\alpha_i - \alpha_0)\cos(\delta_0) \tag{2.5}$$

and

$$Y_i - Y_0 = \delta_i - \delta_0. \tag{2.6}$$

For the isochrone properties, u_c, we calculate the PDF by binning the color-magnitude information over a grid of isochrones that are weighted by a Chabrier IMF (40) and have a fixed solar alpha abundance. These isochrones are described in terms of All metallicities are reported as [Fe/H] $= \log_{10}\left(\frac{Z}{Z}\right)$, with $Z_{=}0.0152$.

The grid of PARSEC isochrones are representative of old metal-poor stellar populations, i.e., $0.0001 < Z < 0.001$, 1 Gyr $< \tau <$ 13.5 Gyr, and $16.0 < m - M < 25.0$ to fit the CMD properties of each object (65). We check that our results do not depend on the isochrone model by comparing to (8) and find that they are insensitive to this specific assumption.

With the above model, we can define the Poisson log-likelihood

$$\log \mathcal{L} = -\lambda N_s - \sum_{i}^{stars} \log(1 - p_i), \tag{2.7}$$

where λ, the stellar richness, is a normalization parameter representative of the total number of member stars with $M_* > 0.1M$ in the satellite, N_s is the fraction of observable satellite member stars, and p_i is the probability that a star is a member of the satellite.

Because we choose to normalize the signal PDF to unity, we can interpret λ as the total number of stars in the satellite (observed + unobserved). The membership probability is given by

$$p_i = \frac{\lambda u_i}{\lambda u_i + b_i}, \tag{2.8}$$

where b_i is the background density function (for more details see Appendix C in Drlica-Wagner et al. (66)). We take the background density function to be independent of spatial position in our

region of interest (ROI).

The empirical background density function, b_i, is determined from an annulus ($7\farcm2 < r < 12'$) surrounding our target ROI ($r < 7\farcm2$). We require the ROI to be $\gtrsim 2 \times r_h$. This is the maximum ROI that still allows for the background annulus to contain $\sim 3 \times r_h$ (23), where r_h is from Koposov et al. and Bechtol et al. (3; 4). Figure 2.1 depicts these regions as blue circles. Any non-stellar objects that still contaminate the data at greater magnitudes are expected to do so equally over the entire FOV and therefore averaged within b_i.

With λ allowed to vary and b_i held fixed, we simultaneously explore the whole parameter space with flat priors for all parameters except r_h (an inverse prior). With `UGaLi`, we run an MCMC chain with 100 walkers, 12000 steps, and 1000 burn-in (67). Absolute V-band magnitude is determined following the prescription of Martin et al. (23)

2.4 Results & Discussion

2.4.1 Grus I

Column 1 of Table 2.5 lists the parameters obtained from the median peak likelihood of the posterior distributions (see Figure 2.4). With our improved parameters for Grus I, we find it to be consistent with an extended ultra-faint dwarf galaxy that resides at the faint edge ($\mu \sim 30$ mag) of the galaxy locus in the size-luminosity plane. Figure 2.5 shows the relationship between GCs and UFDs in this parameter space and also shows the updated location of Grus I. Table 2.5 lists the parameters that were derived in previous works (both Grus I and Indus II are represented).

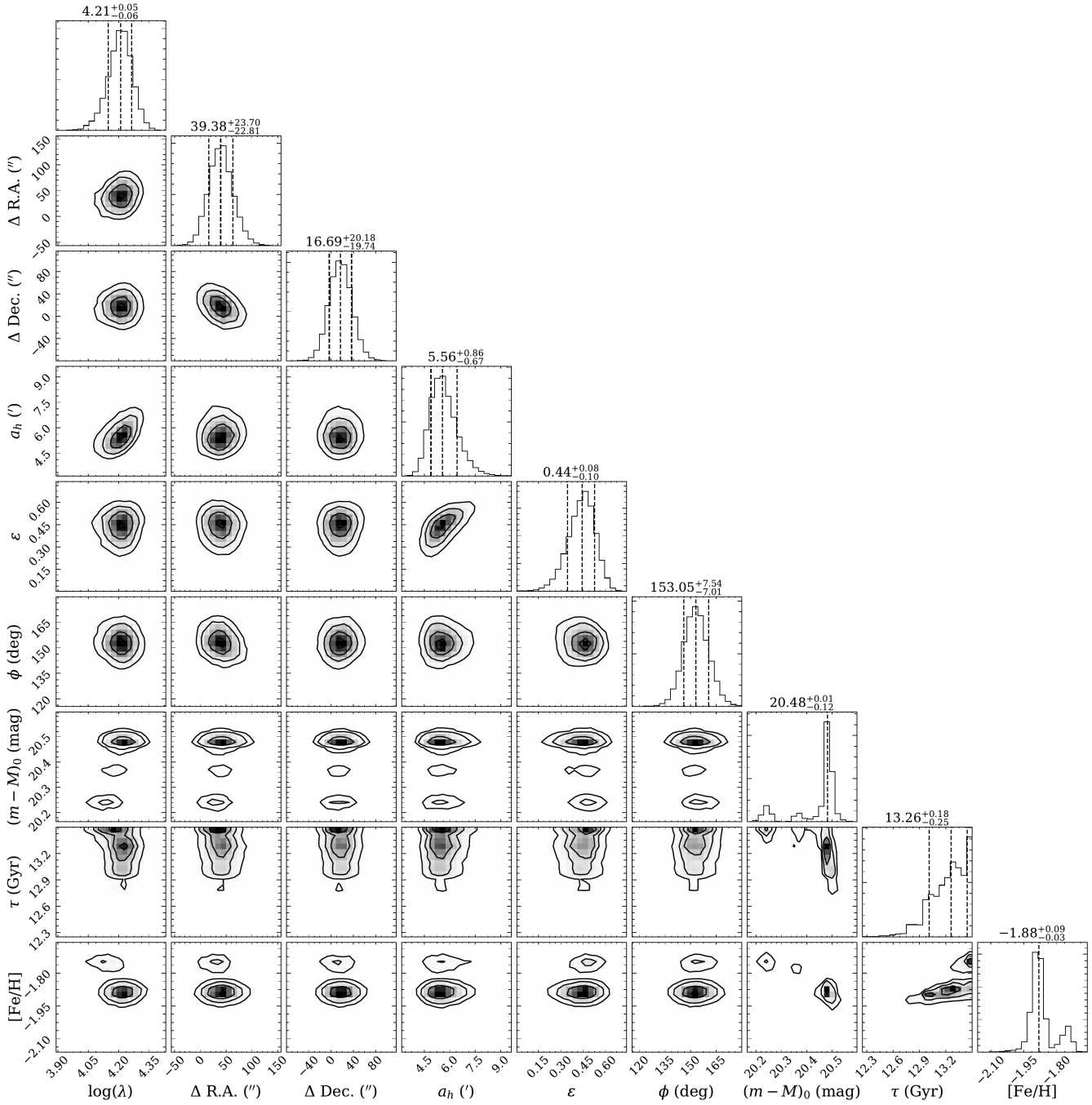

Figure 2.4: Posterior probability distributions for the structural and isochrone parameters of Grus I obtained from an elliptical Plummer model and grid of PARSEC isochrones. The parameters explored were (from left to right): stellar richness (λ), Δ R.A. & Δ Dec.(these are the shift from the centroid found in (3)), semi-major half-light radius (a_h), ellipticity (ϵ), position angle (ϕ), distance modulus ($(m-M)_0$), age (τ), and metallicity ([Fe/H]). Dashed lines in the 1D histograms indicate 16th, 50th, and 84th quantiles of the median peak likelihood. We have excluded these quantiles from $(m-M)_0$ and [Fe/H] due to their bimodality.

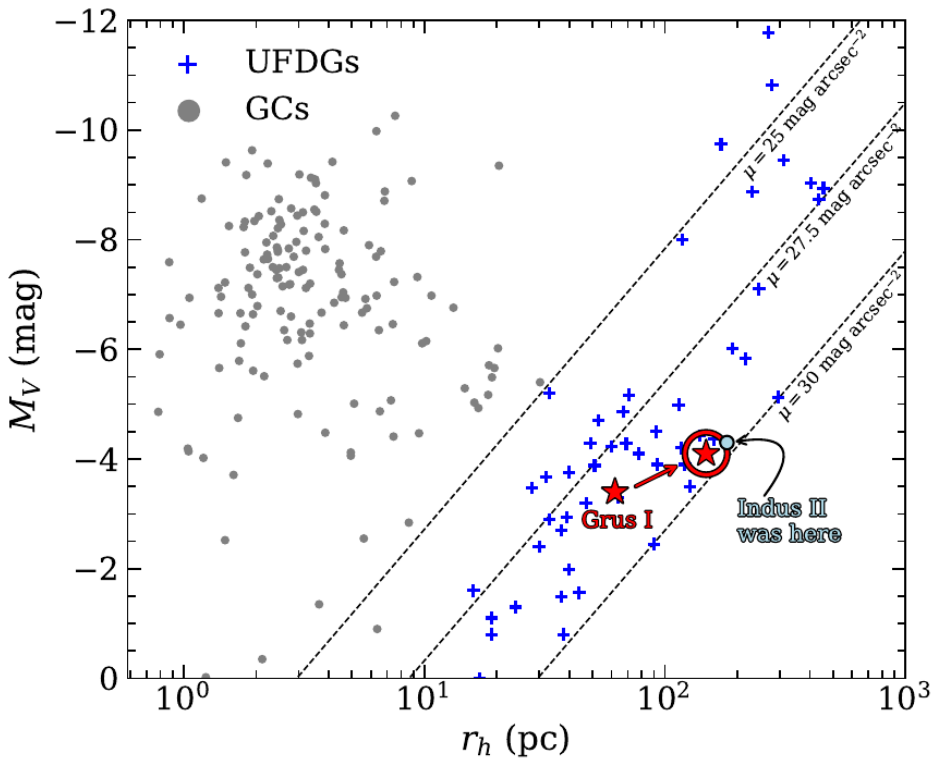

Figure 2.5: Shown as a red star are the position of Grus I with our newly derived properties (circled in red) and its original location in the size-luminosity plane. The original location of Indus II is shown as a light blue circle. The MW globular clusters are in grey points and the rest of the MW UFDs are depicted with blue crosses.

Previous spectroscopic studies by Walker et al. and Ji et al. (10; 12) find the brightest potential member stars are very metal poor (e.g., [Fe/H] ~ -2.3), which is in agreement with the photometric metallicity found in Jerjen et al. (5). In contrast, this and other photometric studies (3) have found it to be less metal poor, i.e., [Fe/H] $\lesssim -2$. In agreement with these studies, several fainter potential member stars were found to be less metal poor (10).

With a $a_h \sim 202$ pc and $M_V \sim -4.1$, we find Grus I is both larger and brighter than estimates from previous works (3; 5; 11). While photometric metallicities are not as reliable as spectroscopic, according to our results, Grus I is among the more metal-rich ([Fe/H] ~ -1.9) UFDs found to date (68). As previous analyses have found mixed results, a larger spectroscopic sample is required to confirm the metallicity of this object.

This discrepancy between spectroscopic and photometric metallicities has been seen in previous studies (see Section 4.3 in Caldwell et al. (69)). In that case, it was considered more likely that the spectroscopic results were likely systematically metal-poor. There was very good agreement with the isochrone calculated with the photometric metallicity and probable member stars.

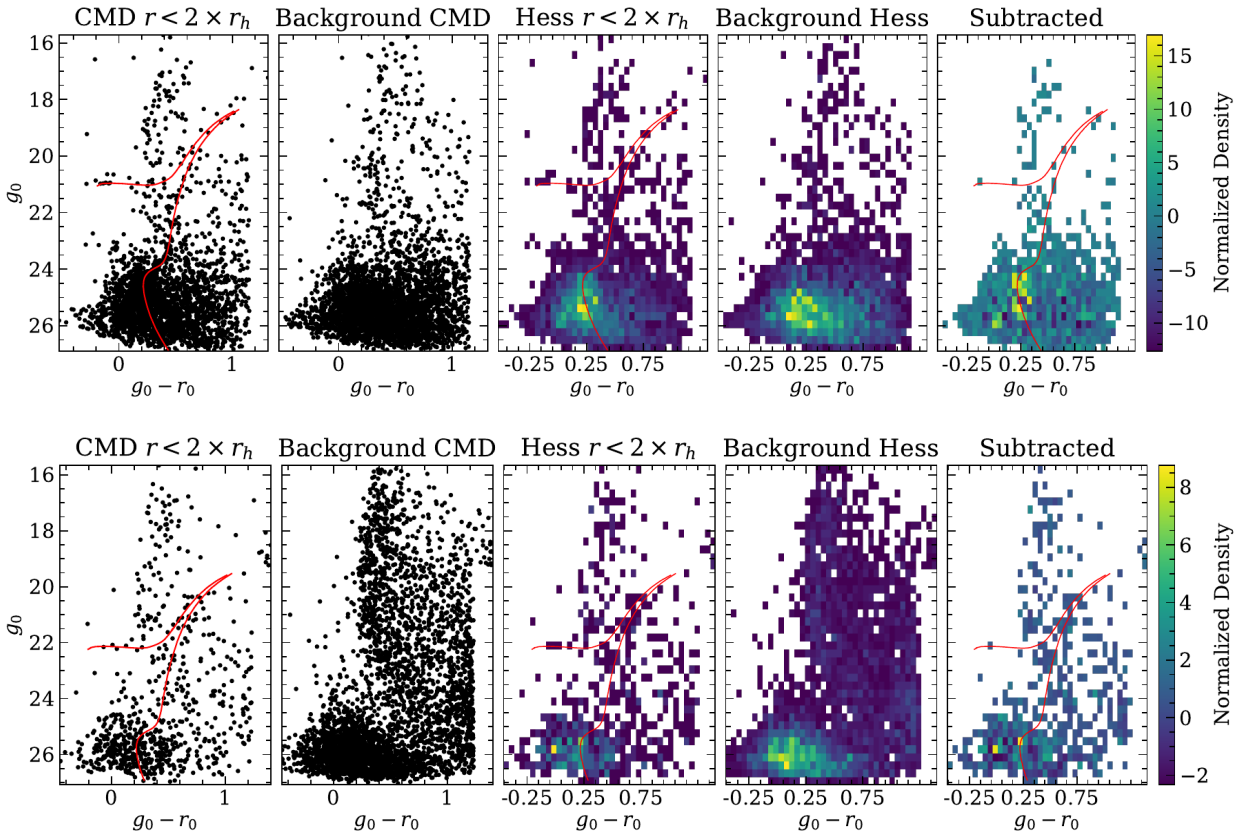

Figure 2.6: The top row of panels is for Grus I CMD and the bottom row is for Indus II CMD. In both cases, the 1st panel shows an ROI of $2 \times r_h$ centered on the object, where Grus I uses properties found in this study (see Table 2.5) and Indus II uses the discovery properties from (4). The 2nd panel is a comparison CMD made from stars $> 2 \times r_h$ away from the ROI. The 3rd panel is the Hess diagram of the stars within $2 \times r_h$ as seen in the 1st panel.The 4th panel is a Hess diagram showing the density of the background stars seen in the 2nd panel. They have been scaled to match the same area as the ROIs. The 5th panel is the Hess difference of the 4th and 3rd panels.

Figure 2.6 shows the CMD of the stars within $2 \times r_h$ and the CMD of the background (see the 1st and 2nd panel, respectively). The last three panels of Figure 2.6 are Hess diagrams of the back-

ground stellar density, the stellar density within $2 \times r_h$, and the difference of the two (see panels 3, 4, and 5, respectively). Overlaid in the 1st, 4th, and 5th panels is a PARSEC isochrone representative of an old, metal-poor population with $\tau = 13.3$ Gyr and [Fe/H] $= -1.9$. This isochrone agrees with the best-fit properties of Grus I inferred from the maximum likelihood distribution.

For Grus I the background-subtracted Hess diagram shown in the 5th panel of Figure 2.6, clearly illuminates MSTO and MS that are well-represented by the inferred properties. Less obvious, but still well-populated, the isochrone clearly delineates a HB and RGB population. It should be noted that some potential members can still be seen in the second top-row panel (background CMD) of Figure 2.6 due to Grus I's large extent.

In the left two panels of Figure 2.7, we show the distribution of the `UGaLi` membership probabilities in sky coordinates and color-magnitude space. These membership probabilities were determined as described in §2.3. The three panels in this figure show that our inferred parameters describing the stellar population and morphology of Grus I are consistent with a theoretical Plummer profile.

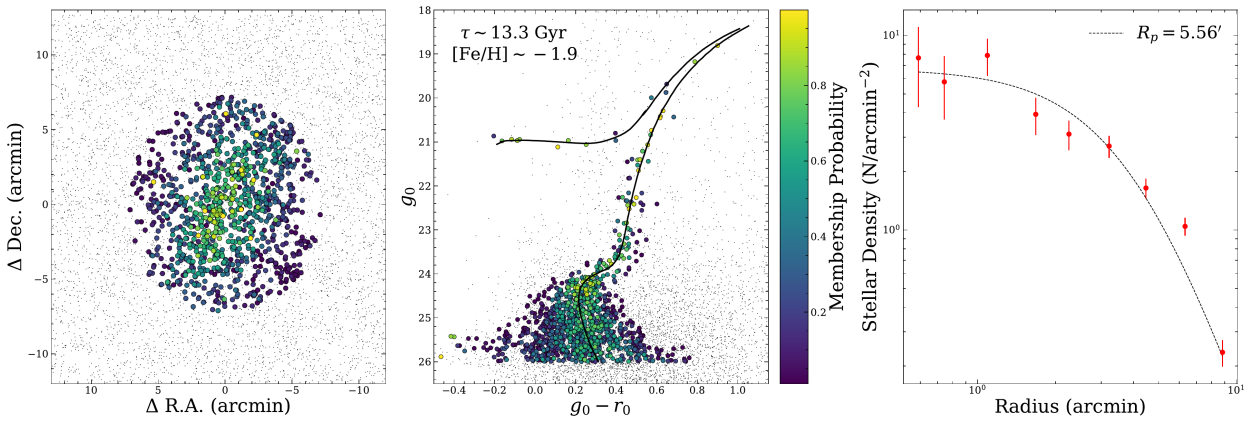

Figure 2.7: Right panel: Spatial distribution of stars in Grus I that have high membership probability. Middle Panel: Color-magnitude diagram of the same stars with high membership probability. The black line is the isochrone best described by our newly derived parameters in Table 2.5. Gray points in both panels are stars with less than 5% membership probability. Right panel: The stellar density profile of Grus I where the data is shown in red in elliptical bins of equal number and weighted by associated membership probabilities. The black dashed line shows the theoretical two-dimensional Plummer profile created with a Plummer-scale radius equal to $a_h = 5.6'$.

These probabilities were further used to create a binned and weighted density profile as seen in the far right panel of Figure 2.7. There are an equal number of stars in each bin. It can be seen that the binned data fits well over the Plummer model profile shown as the dashed line.

The posterior distributions and maximum-likelihood peak values are shown in Figure 2.4. While some of the properties shown in Figure 2.4 agree with previous works (see Table 2.5) within the uncertainties (e.g., centroid coordinates, ellipticity, distance modulus), others have shifted slightly in this work (i.e., r_h), changing some of the derived properties.

Jerjen et al. (5) find two small overdensities at $[(\alpha - \alpha_0), (\delta - \delta_0)] \approx [+0.2, -0.5]$ (arcmin) and $[(\alpha - \alpha_0), (\delta - \delta_0)] \approx [-0.6, +0.8]$ (arcmin)–with extents of 22×25 pc and 13×28 pc, respectively. It is interesting to note that we do not find obvious evidence of the two slight overdensities or diffuse centroid found in (5). Our centroid shift does not seem to be significant or dependent on any lack of dense central overdensity as can be seen in Figure 2.8. The dashed yellow line in this figure indicates the halflight radius created with our inferred parameters.

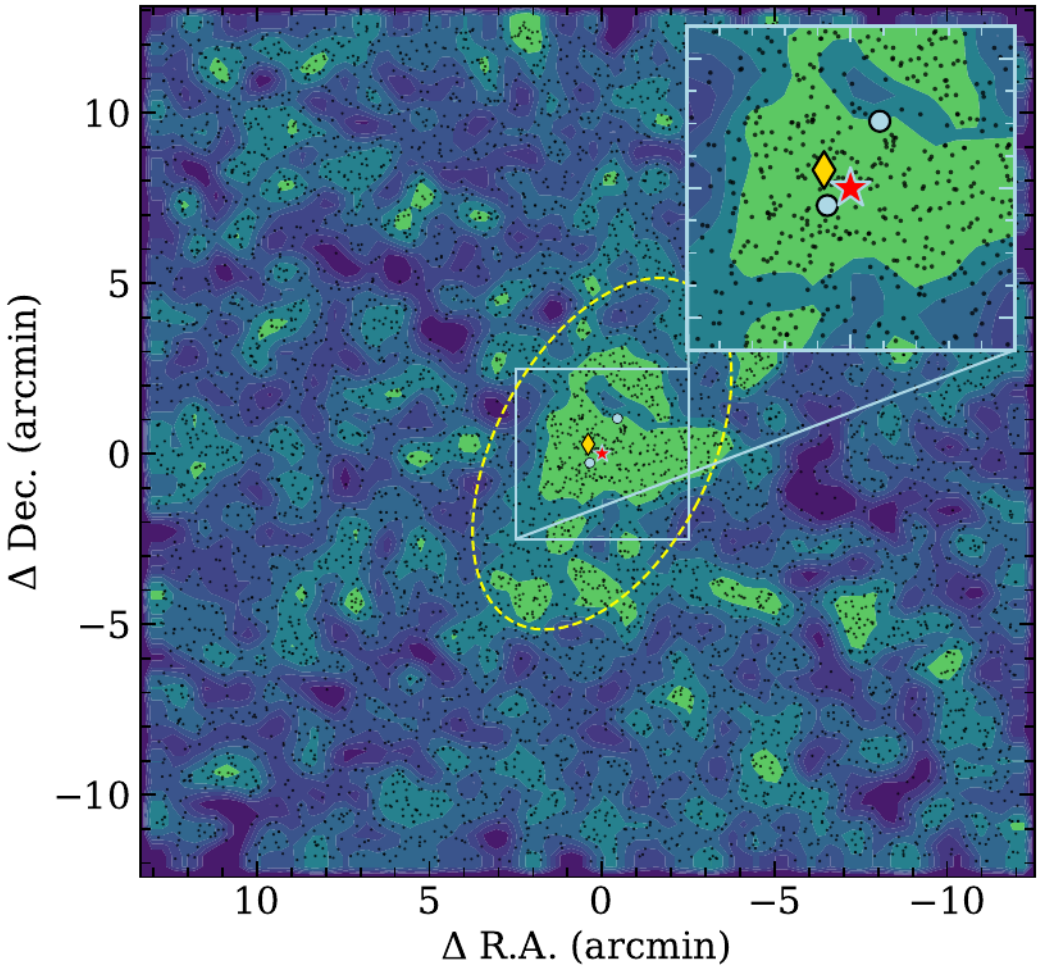

Figure 2.8: The $3-\sigma$ iso-density contours of Grus I with our redetermined centroid shown as a red star. The blue circles represent the location of the two overdensities mentioned in Jerjen et al. (5) and the gold diamond is the original centroid found in Koposov et al. (3). The yellow dashed ellipse indicates the Plummer halflight radius found in this work.

The r_h ($4\farcm16$) found in this work is larger than previous works by more than a factor of 2. Our larger FOV (see Figure 2.1) allows us to more accurately constrain the local background contamination and is likely the reason for the change in extent. Additionally, we find Grus I to be about one magnitude brighter ($M_V \sim -4.1$ mag) than previously thought (3), while the distance to the object is in agreement with the recently updated distance determination based on RR Lyrae stars (13).

It should be noted that Jhelum, a nearby stellar stream ($\mathrm{D}_\odot \sim 13$ kpc, $m - M \sim 15.6$)(63),

potentially contaminates the FOV. In order to test this, we cut potential stream member stars from our catalog and performed the same analysis on the new catalog. These potential members were chosen based on Jhelum's spatial footprint and location in color-magnitude space. The width of the area in color-magnitude space was chosen to account for our photometric uncertainties. The distance of the Jhelum stream ($D_{\odot} \sim 13$ kpc) compared to how far Grus I is precludes any physical association between the two. The results from this analysis were similar within uncertainties. Therefore, we determined that the presence of the stream does not significantly affect our analysis.

2.4.2 Indus II

MCMC chains run on this object fail to converge and no membership probabilities are calculated. The resulting isochrone parameters from the uncoverged chains are indicative of a young stellar population, which is inconsistent with UFDs or globular clusters.

In all but the background panels of Figure 2.6, the UFD representative old, metal-poor isochrone delineates the HB but fails to match with any other CMD feature. The derived isochrone fails to match the BHB stars that its candidacy hinged on originally. This indicates Indus II is likely a false-positive, i.e., neither a dwarf galaxy nor a globular cluster.

Since we have found that Indus II is neither a real galaxy nor a cluster, it goes against convention to use Indus II as its designation. We prefer to use the designation Indus II from now on.

Table 2.5: Photometric and spectroscopic parameters of Grus I and Indus II found in the literature prior to this work. The columns for Grus I, in order, are from this work, (3; 10; 5; 11; 12; 13). Column 8 describes Indus II as found in the discovery paper, (4).

	Grus I							Indus II
	This Work							
	(1)	(2)	(3)	(4)	(5)	(6)	(7)	(8)
α_{2000} (deg)	$344.166^{+0.007}_{-0.006}$	344.1765	···	344.1700	344.179	···	···	309.76
δ_{2000} (deg)	$-50.168^{+0.006}_{-0.005}$	-50.1633	···	-50.1641	-50.1800	···	···	-46.16
t-value (σ)	21.3	10.1	···	···	···	···	···	~ 5.7
M_V (mag)	-4.1 ± 0.3	-3.4 ± 0.3	···	···	···	···	···	-4.3 ± 0.19
D (kpc)	125^{+6}_{-12}	120	···	115 ± 6	···	···	···	214 ± 16
r_h (arcmin)	$4.16^{+0.54}_{-0.74}$	$1.77^{+0.85}_{-0.39} b$	···	···	0.81 ± 0.66b	···	···	$2.9^{1.1}_{1.0} b$
r_h (pc)	151^{+21}_{-31}	$62^{+29.8}_{-13.6}$	···	···	28.3 ± 23.0	···	···	181 ± 67
ϵ	$0.44^{+0.08}_{-0.10}$	$0.41^{+0.20}_{-0.28}$	···	···	0.45 ± 0.30	···	···	< 0.4
ϕ (deg)	$153^{+8.0}_{-7.0}$	4 ± 60	···	···	23 ± 18	···	···	···
$m - M$ (mag)	$20.48^{+0.11}_{-0.22} a$	20.4	···	20.30 ± 0.11	···	···	$20.51 \pm 0.10 c$	···
τ (Gyr)	$13.26^{+0.18}_{-0.25}$	···	···	$14.0^{+1.0}_{-1.0}$	···	···	···	···
$[Fe/H]$ (dex)	$-1.88^{+0.09}_{-0.03}$	···	$-1.42^{+0.55}_{-0.42}$	$-2.5^{+0.3}_{-0.3}$	-2.5 ± 0.3	$-2.57, -2.50$	···	···
$\sigma_{[Fe/H]}$ (dex)	···	···	< 0.9	···	···	···	···	···
$\langle v_{LOS} \rangle$ (km s^{-1})	···	···	$-140.5^{+2.4}_{-1.6}$	···	···	···	···	···
$\sigma_{v_{LOS}}$ (km s^{-1})	···	···	< 9.8	···	···	···	···	···
$M_/L_{V,}$	···	···	< 2645	···	···	···	···	···

aA systematic uncertainty of 0.1 mag was added to account for the difference between best-fits for (65) and (8) isochrones. bSemi-major halflight radii converted from azimuthally-averaged radii with $\sqrt{1-\epsilon}$ factor. cThis distance measurement is based on two RR Lyrae stars found in Grus I.

3. IMF ANALYSIS

3.1 Introduction

Ultra-faint Dwarf galaxies provide a unique laboratory of a variety of physical processes due to their extreme nature. As the most dark matter dominated (24), yet low mass galaxies in the Universe categorizing these objects is key to answering still open questions.

These objects are found in ground-based optical surveys as statistical stellar overdensities (6). Currently, there are more than 50 confirmed and candidate UFDs. As the next generation of surveys comes online and pushes the limits of ages and metallicities, more of these objects continue to be found. As we continue to probe deeper and find fainter objects, we also gain the ability to more accurately characterize the UFDs we do know. Additionally, we can push the boundaries and start placing constraints on the low-mass end of the IMF of galaxies.

In the MW and in massive stars, the IMF seems to be fairly universal—well described by the classical Salpeter IMF (38). In order to explore the empirical nature of the IMF, it becomes necessary to study it in other environments. Low-mass environments, in particular, provide an opportunity to better explore any dramatic effects from the stellar birth cloud or the gas density (45). IMF studies on dwarf galaxies and UFDs has been done before, but always with space-based data (45; 70).

The IMF of several of the larger dwarf galaxies has been measured using optical photometry from HST/WFPC2 and HST/ACS. Draco was found to have $2.1 < \alpha < 2.3$ (71), Ursa Minor $\alpha = 1.8$ (72), and $\alpha = 1.9$ for the SMC (73). Geha et al. found power-law slopes for the dwarfs, Hercules and Leo IV, shallower than the Salpeter IMF at $\alpha = 1.2$ and $\alpha = 1.3$, respectively (45). To complement Geha et al., Gennaro et al. found IMF slopes for four more dwarfs: Boo I, CVn II, Com Ber, and UMaI with $\alpha = 1.87, 1.17, 1.68, 1.58$, respectively (70).

All of these environments consist of sub-solar masses and low-metallicities and there's some correlation between IMF slope and average metallicity (70). There's also some variability within

the UFD sample itself though. This further emphasizes the need for increased numbers of UFD IMFs.

Here, we will provide an updated analysis of all the confirmed and candidate UFDs in the DES footprint (6). We will also show that constraining the IMF with ground-based survey data is possible and provide an analysis of the slope of the IMF of two UFDs from that list.

3.2 Data

Similar to the analysis completed in Chapter 2, we use DES photometry. However, in this study we use DES photometry only and update our data set to the Y6_GOLD catalog. Y6_GOLD is created using the full 6 years of DES data (compared to 3 years for DES DR1) and is thus deeper and more spatially complete in the $grizY$ bands, and is the data used for the second public data release (DES DR2) (74). DR2 consists of 681 nights of observations from August 2013 to January 2019. The final catalog has a photometric precision $< 1\%$ and a coadded depth of $g = 24.7$ and $r = 24.4$ at a signal-to-noise (S/N) $= 10$ (74).

The Y6_GOLD data were reduced homogeneously using the DESDM pipeline (61). This pipeline includes an overscan correction, flat-fielding, bias subtraction, masking, and astrometric calibration using *Gaia*. The source catalog was created using `PSFEx` (75) and `SourceExtractor` (76) to perform PSF modeling and source detection respectively.

This work focuses on the very small and often diffuse systems made of resolved, faint stellar sources. To that end, we use the coadded images produced by the multi-epoch pipeline. Created in a manner similar to the Y3 GOLD coadded images, there were some changes to increase uniformity and overall data quality. This has resulted in small “holes" in the footprint where there was apparent coverage before (74). However, the overall quality of the data is unprecedented.

For this work, we require a mostly complete stellar sample (which can lead to galaxy contamination across the FOV). This sample was created by applying the EXTENDED_CLASS_MASH selection flag with a value between 0 and 2. This is similar to the extended classifier described in the previous chapter (see Equations 1, 2, and 3 in Shipp et al. (63)). Where again, there is a value of 0 for high confidence stars, 1 for candidate stars, 2 for mostly galaxies, and 3 for high confidence

galaxies. This star/galaxy classifier uses the classifications derived first from multi-object fitting (MOF), then single-object fitting (SOF), then weighted average (WAVG) values from single epoch detections, and lastly values from `SourceExtractor` detections (74).

3.2.1 Simulated Data

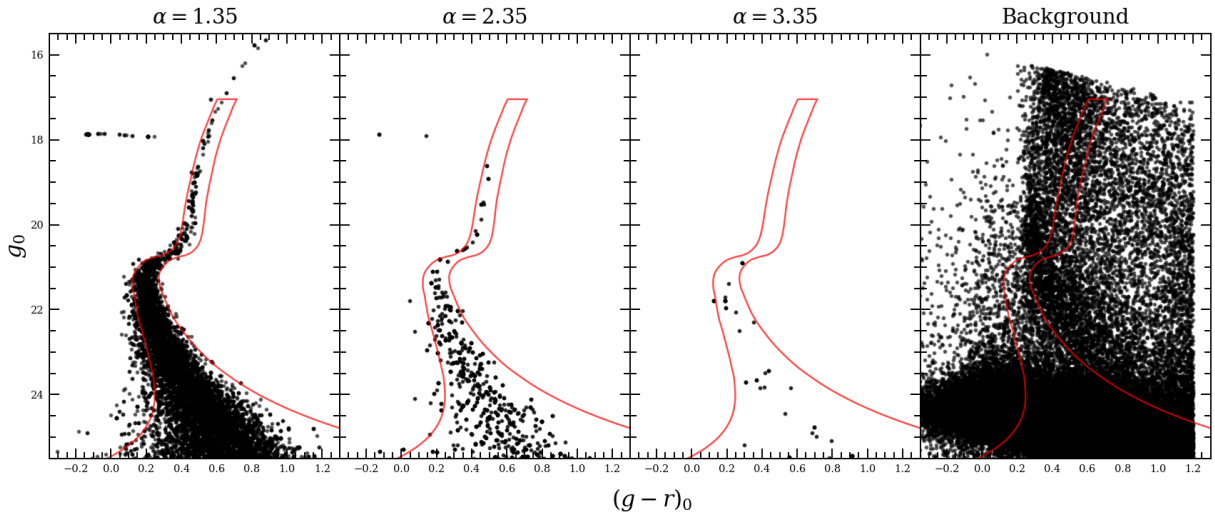

Figure 3.1: Example of simulated data created to test our ability to recover physical parameters and IMF slope. Additionally used to test observational limitations of IMF target candidates and determine proper magnitude, color, and spatial cuts for accurate characterization.

We used `UGaLi` to create g- and r-band magnitudes of old, simple stellar populations specifying the age, metallicity, distance modulus, and IMF slope. We then attached these to positions generated from an elliptical Plummer distribution to simulate typical UFDs (64). Each simulated star was given an “observational" error based on its apparent magnitude that was representative of measured observational uncertainties of the Y6_GOLD dataset used in the final analysis. Finally, a background region was created by identifying a 2.5×2.5 degree area of the DES footprint that did not contain any contaminating stellar populations (see the rightmost panel of Figure 3.1). Each simulated UFD was embedded in this “background."

An example of these simulations can be seen in Figure 3.1. The dramatic impact of changing

Table 3.1: An example of a simulated stellar catalog—sorted by star ID. This table is published in its entirety in machine-readable format. A portion is shown here for guidance regarding its form and content. All magnitudes are in the DES magnitude system.

Star ID	R.A. (deg)	Dec. (deg)	$g_{0,DES}$ (mag)	σ_g (mag)	$r_{0,DES}$ (mag)	σ_r (mag)
898684388	53.956	−54.640	23.088	0.045	22.794	0.038
398684425	53.303	−54.640	22.027	0.015	21.525	0.010
398684592	53.692	−54.638	23.492	0.049	23.173	0.042
398684593	53.140	−54.633	22.732	0.028	22.323	0.020
398684749	53.536	−54.628	23.430	0.058	23.077	0.040
398684802	53.779	−54.633	23.725	0.121	23.681	0.105

the slope of the IMF can be seen clearly in this figure. With a shallower slope (e.g $\alpha = 1.35$; see the first panel), the system is clearly more populated along the MS and up the RGB. We used these simulations to test the accuracy and precision of our analysis method. Additionally, we used these simulations to determine the limitations in this method and appropriate magnitude and color cuts to obtain the most accurate characterizations.

We found that with DES Y6_GOLD data a faint magnitude limit of $g = 24$ was required to recover input parameters, including the IMF slope (α). This is 0.7 mags brighter than the faint limit of the Y6_GOLD data set. After testing bright magnitude limits, it was determined that leaving the full range of brighter magnitudes ($g \lesssim 16$) resulted in better background constraints and subtraction. As can be seen in Figure 3.1, α is also clearly a limiting factor. A theoretical UFD with a steeper slope (see panel 3, $\alpha = 3.35$) would have considerably fewer stars, making it harder to observe and statistically separate from the background.

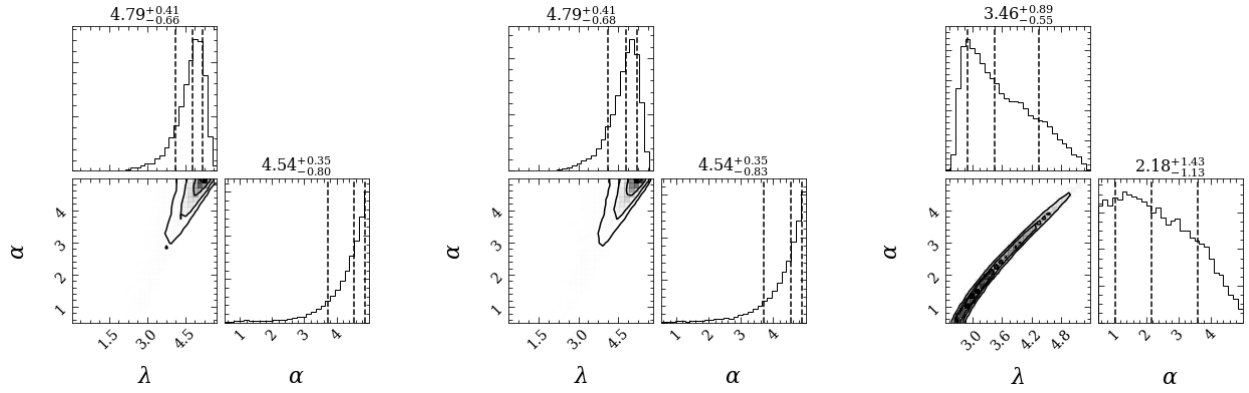

Figure 3.2: The leftmost panel has $M_V = -1$, the middle panel has $M_V = -2$, and the rightmost panel has $M_V = -3$. All other simulated physical properties are the same among all three panels. These were preliminary runs shown here to provide an example of the testing that was done with the simulated data.

Figure 3.2 shows preliminary results testing the efficacy of our method on various masses. The first two panels in this figure indicate that α is not recoverable for objects fainter than $M_V \sim -2$. The third panel shows that the analysis method is starting to pick up on a more signal than noise. The recovery of other morphological and isochrone parameters is not affected as strongly by this limitation on recovering α. This sort of testing was done on mass limitations, apparent magnitude limitations (bright and faint), distance, size, and α.

Specifically, simulating a Ret II-like object, we show that a full analysis (including IMF slope determination) is possible for an object of this size and makeup (see Figure 3.3). Reticulum II has $a_h = 5.52$ arcmin, $M_V = -3.9$, and is only 30 kpc away. Tucana III is likewise only 25 kpc away, although it is fainter and smaller than Reticulum II. Given this information, we selected Ret II and Tuc III to provide UFD slope constraints, as well as using the deep, wide, and precise Y6_GOLD data to provide and confirm updated characterization. For the rest of the targets, we hold α fixed at the classical Salpeter slope of 2.35 (38).

We found that the isochrone parameters were difficult to recover depending on the size and luminosity of the object. With a well-populated MSTO and either a RGB or HB, the isochrone parameters can be reasonably recovered (although there's a clear degeneracy between age and

distance modulus). Also, α plays a significant role in the efficacy of this analysis through affecting the number of observable stars. When the slope is steeper (as in the right panel of Figure 3.3 and in Figure 3.4; $\alpha = 3.35$), the parameters become harder to recover—particularly the isochrone parameters. To reduce the available parameter space and get stronger constraints on α, we also ran our analysis with metallicity and or age held fixed when the literature values were from a reliable source (e.g., spectroscopy or RR Lyrae studies).

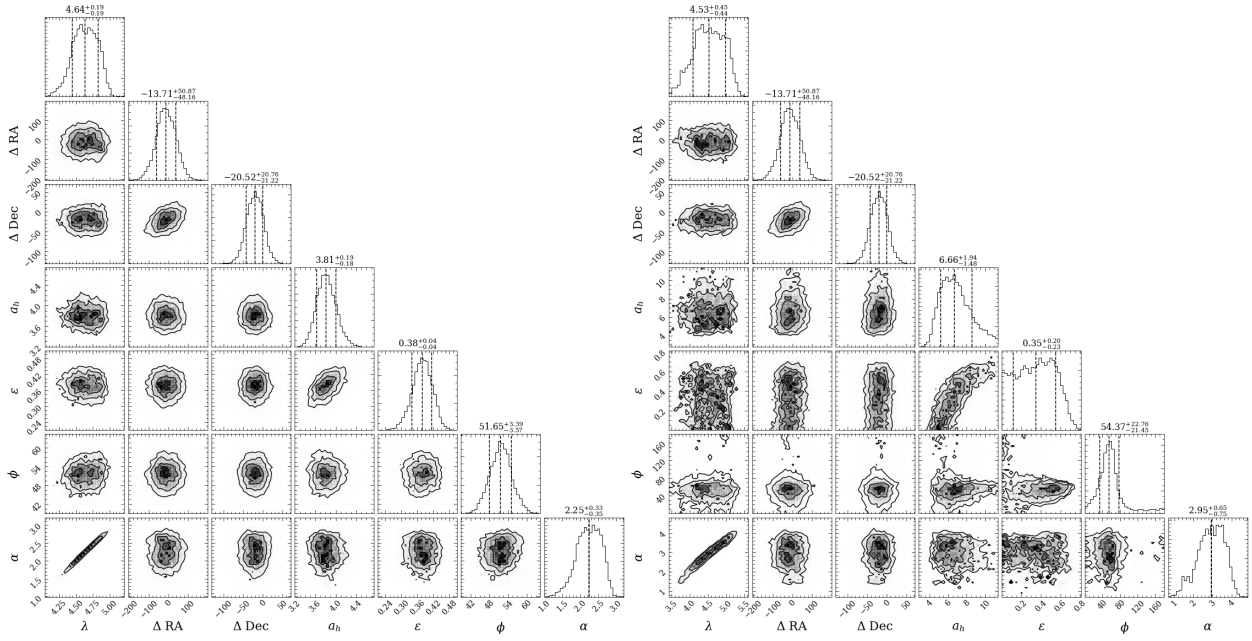

Figure 3.3: Simulated datasets with all physical properties the same except for α. The panel on the left has $\alpha = 1.35$ and the figure on the right has $\alpha = 3.35$ It can be seen that morphological convergence (all other things being equal) is easier to achieve and more precise with a shallower slope.

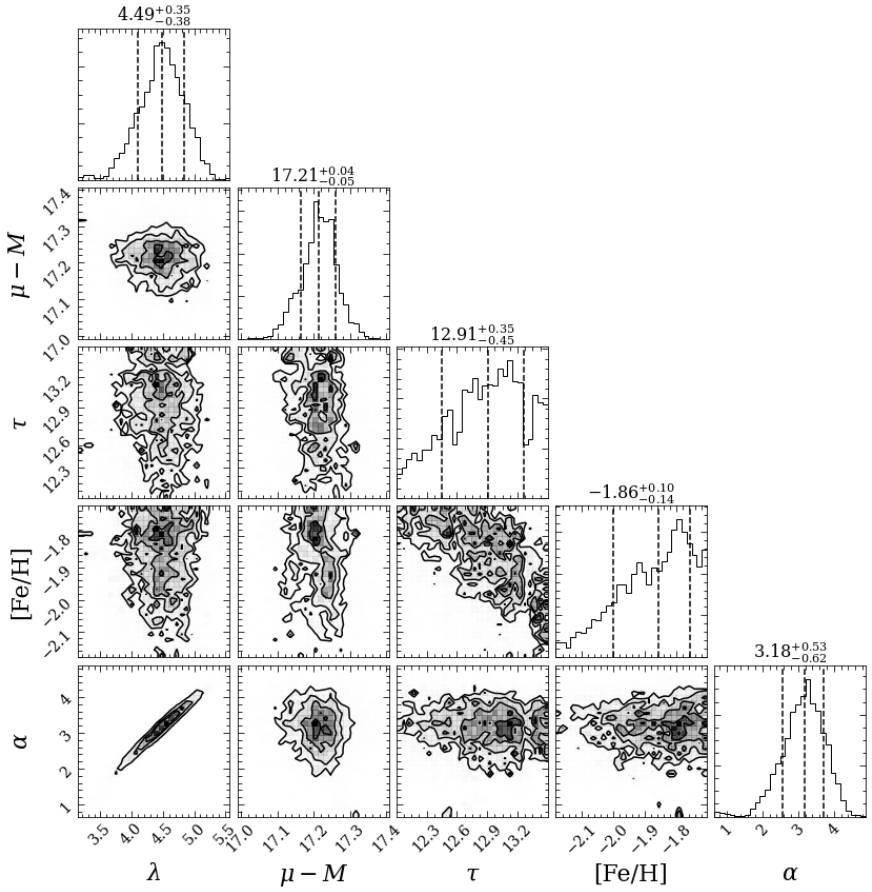

Figure 3.4: Simulated data set with $alpha = 3.35$. This is an example of recovering the isochrone parameter values with a steeper slope.

3.2.2 Target Objects

As mentioned in Section 3.1, the data sample described in Section 3.2 will be used to infer updated physical properties of 20 target objects. Listed in Table 3.2 are all of the current literature values (6). Figure 3.5 shows the CMD of all the target objects. They are overlaid with an old, metal-poor isochrone ($\tau = 13.0$ Gyr, $[Fe/H] = -2.34$) with spread representative of this data sets photometric uncertainty. It can immediately be seen that some objects are more populated than others and therefore likely easier to analyze (e.g., Ret II and Tuc III; fourth row, third panel and fifth row, second panel, respectively). You can also see a clear HB around $g \sim 23$ in Eri II (second row, first panel).

Table 3.2: 20 targets

Name	RA (deg)	Dec (deg)	$m-M$ (mag)	a_h ($'$)	ϵ	Distance (kpc)	$r_{1/2}$ (pc)	M_V (mag)	Ref.
Cetus II	19.47	-17.42	17.4	1.9	< 0.4	30	17	0.0	(4)
Cetus III	31.331	-4.270	22.0	1.23	0.76	251	44	-2.5	(77)
Columba I	82.86	-28.01	21.3	2.2	0.3	183	98	-4.2	(78)
DES J0225+0304	36.4267	3.0695	16.9	2.68	0.61	24	12	-1.1	(79)
Eridanus II	56.0925	-43.5329	22.9	1.77	0.35	380	158	-7.21	(11)
Eridanus III	35.69	-52.28	19.8	0.315	0.44	91	8.6	-2.07	(80)
Grus I	344.1797	-50.18	20.4	0.81	0.45	120	21	-3.47	(11)
Grus II	331.02	-46.44	18.6	6.0	< 0.2	53	92	-3.9	(4)
Horologium I	43.8813	-54.116	19.5	1.59	0.27	79	31	-3.55	(11)
Horologium II	49.1077	-50.0486	19.5	2.09	0.52	78	33	-2.6	(81)
Indus II	309.72	-46.16	21.7	2.9	< 0.4	214	180	-4.3	(4)
Kim 2	317.2020	-51.1671	20.0	0.48	0.32	100	12	-3.32	(11)
Phoenix II	354.996	-54.4115	19.6	1.49	0.67	83	21	-3.30	(11)
Pictor I	70.949	-50.2854	20.3	0.88	0.63	114	18	-3.45	(11)
Reticulum II	53.9203	-54.0513	17.4	5.52	0.58	30	31	-3.88	(11)
Reticulum III	56.36	-60.45	19.8	2.4	< 0.4	92	64	-3.3	(4)
Tucana II	342.9796	-58.5689	18.8	12.59	0.39	58	165	-3.8	(3)
Tucana III	359.15	-59.60	17.0	6.0	0.0	25	44	-2.4	(4)
Tucana IV	0.73	-60.85	18.4	11.8	0.4	48	128	-3.5	(4)
Tucana V	354.35	-63.27	18.7	1.8	0.7	55	16	-1.6	(4)

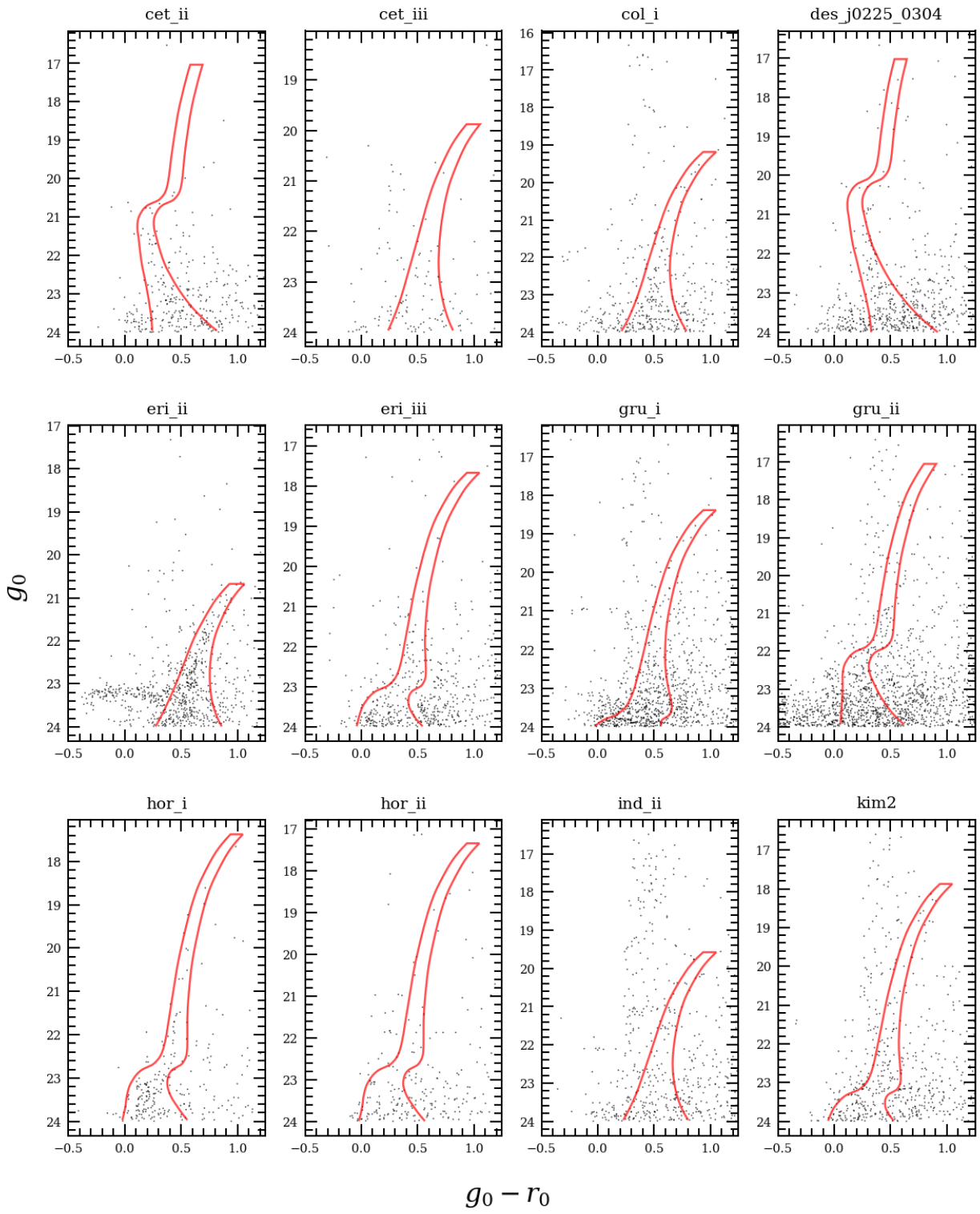

Figure 3.5: Shown here are CMDs of all the confirmed and candidate UFDs from the DES footprint (6). The isochrone overlaid is a Dotter 2008 (7) of age 13.0 Gyr and $[Fe/h] = 2.34$, representative of typical UFD populations. The spread in the isochrone is an applied error function based on the Y6_GOLD data.

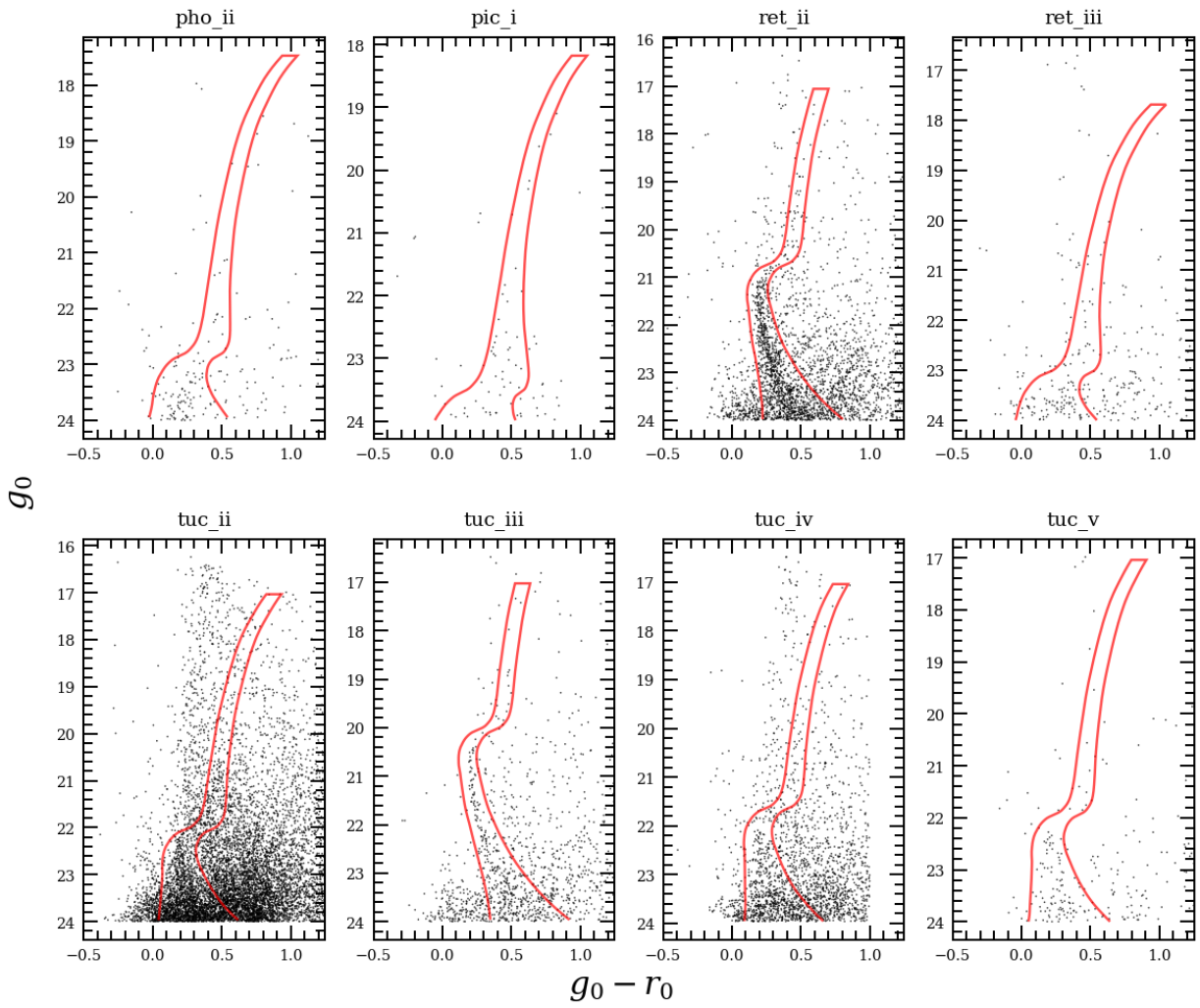

Figure 3.5: Continued

3.3 Methods

Similar to Chapter 2, we used the Ultra-faint Galaxy Likelihood (`UGaLi`) toolkit to provide updated characterization for all the candidate and confirmed UFDs in the DES footprint. In order to better characterize the UFDs in DES, we modified `UGaLi` to additionally fit for the IMF.

For both the simulated and real data, our input data consists of two filters ($g-$ and $r-$ band) and their associated errors. In the case of the simulated data, these were errors empirically found to well model representative of errors in the Y6_GOLD catalog. Our input data also consists of

the spatial positions of the stars (RA and Dec.). The simulated stellar positions were created by randomly drawing from an elliptical Plummer distribution and assigning them magnitudes from the simulated stellar population.

Our improvements on the previous method affected only the second part of Equation 2.2,

$$u_c(\mathcal{D}_{c,i}|\boldsymbol{\theta}_c). \tag{3.1}$$

It follows that u_c now consists of the following model parameters: distance modulus $(m - M)$, age (τ), and metallicity (Z), and the slope of the IMF (α).

3.3.1 Analysis

In the course of testing our improvements on `UGaLi`, we also explored the effects of different isochrones (e.g., Parsec (65), Dotter 2008 (7), and Dotter 2016 (8), etc.). It has been found before that some of these isochrones are bluer than is found spectroscopically (6). We determined that Dotter 2008 isochrones were the truest to spectroscopic metallicity. Figure 3.6 shows the slight difference between the Dotter 2016 (8) and the Dotter 2008 (7) along the red giant branch (RGB). While previously we found that this did not significantly affect the results of our analysis (along the MS these isochrones are very similar), with the addition of the sensitive slope information we decided to use Dotter 2008 isochrones for the remainder of the analysis.

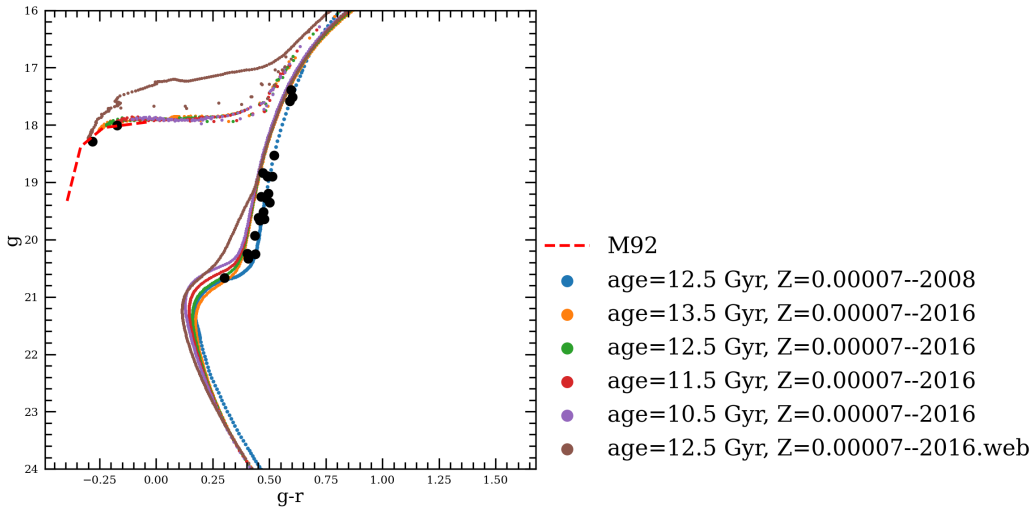

Figure 3.6: Comparing Dotter 2008 (7), Dotter 2016 (8), and Dotter 2016 downloaded from the website (8). The black dots are spectra from Simon et al. (9).

Another benefit of the Dotter 2008 isochrones is that they reach lower metallicities. The isochrone grid is then $0.00007 < Z < 0.001$, 1Gyr $< \tau <$ 13.5Gyr, $16.0 < m - M < 25.0$, and $0.5 < \alpha < 4.5$. Equation 2.2 is then calculated by binning the color $(g - r)$ and magnitude information over this grid. When α is held fixed (as is the case with most of the targets), the isochrones are weighted by a Chabrier IMF (40) in the form of a power-law plus a log-normal distribution at low masses. When α is allowed to vary, the IMF takes on the form of a simple power law,

$$\int \frac{dN}{dm} = Am^{-\alpha}, \tag{3.2}$$

where DN/dm is the change in number of stars formed with a given stellar mass, A is a normalization parameter, and m is mass. The normalization parameter, A, is calculated with each step to normalize the integral of the IMF to be 1 for the mass range $0.1\,\mathrm{M}_\odot < M_\star < 100\,\mathrm{M}_\odot$.

For the morphological properties (the first part of Equation 2.2), we still assume an elliptical Plummer model (64; 23) as described by Equations 2.3, 2.4, 2.6, and 2.5. There are five free parameters that describe the first part of : the centroid coordinates (α_0, δ_0,), the semi-major half-light radius (a_h), the ellipticity (ϵ), and position angle (ϕ).

We define our Poisson log-likelihood as

$$\log \mathcal{L} = -\lambda N_s - \sum_{i}^{stars} \log(1 - p_i), \tag{3.3}$$

no change in the where λ is still the normalization parameter (for stars $M_\star > 0.1 M_\odot$), N_s is the fraction of observable satellite member stars, and p_i is membership probability.

We normalize Equation 2.2 of the signal to unity, allowing us to infer the total number of stars in each target object—both observed and unobserved. We calculate the membership probability of stars in the ROI with Equation 2.8 and consider the background density function, b_i, as independent of spatial position.

We find the background function from an annulus surrounding our target ROI. Because of the survey nature of DES data we can utilize a FOV large enough to account for proper background statistics (23; 13). In most cases, we take our target ROI to be ($r < 0.5\,\mathrm{deg}$) and determine b_i from an annulus ($0.5\,\mathrm{deg} < r < 2.0\,\mathrm{deg}$) surrounding the target ROI. In the case of Eri III and Kim 2, we use a target ROI of $r < 0.2\,\mathrm{deg}$ and a background annulus of $0.2\,\mathrm{deg} < r < 1.0$ because their semi-major halflight radii are significantly smaller than the rest of the targets $r_h < 0.'5$) For Tuc II and Tuc IV, we use a target ROI of $r < 5.0\,\mathrm{deg}$ and a background annulus of $1.25\,\mathrm{deg} < r < 5.0\,\mathrm{deg}$. Their semi-major halflight radii are $r_h \gtrsim 9'$.

In all cases, we allow λ to vary and hold b_i fixed. In the case of Ret II we hold Z and $m - M$ fixed and for Ret II and Tuc III, we allow α to vary. Through the `UGaLi` toolkit we run an MCMC chain that results in 5200,000 samples exploring the whole parameter space with flat priors (with the exception of r_h, which has an inverse prior).

3.4 Results

We were able to obtain results on 65% of our target objects. Table 3.3 provides a summary of updated parameter values obtained from the median peak likelihood of the posterior distributions (see Figures 3.7 - 3.24). Results for each object are detailed in the following subsections—as well as an assessment on if it is likely possible to constrain an IMF for each object with the current data.

Table 3.3: Listed here are the results of refitting objects with Y6_GOLD data.

Name	RA (deg)	Dec (deg)	a_h ($'$)	ϵ	Distance (kpc)	$r_{1/2}$ (pc)	M_V (mag)	α
Cetus II	-17.48 ± 0.03	19.42 ± 0.02	$6.94^{1.6}_{1.3}$	0.7	30	25	-1.3	$\cdots$
Columba I	$82.87^{+0.03}_{-0.05}$	-28.04 ± 0.02	$2.61^{+0.92}_{-0.59}$	0.24	183	121	-5.2	$\cdots$
Eridanus II	56.1 ± 0.1	-43.53 ± 0.01	$2.13^{+0.23}_{-0.21}$	0.34	363	178	-7.8	$\cdots$
Eridanus III	$35.691^{+0.004}_{-0.005}$	-52.28 ± 0.001	$0.61^{+0.17}_{0.13}$	0.61	91	9	-2.6	$\cdots$
Grus I	$344.17^{-0.32}_{+0.03}$	$-50.17^{+0.26}_{-0.02}$	$2.76^{+1.34}_{-0.85}$	0.36	126	74	-4.6	$\cdots$
Horologium I	43.88 ± 0.01	$-54.12^{+0.004}_{-0.5003}$	1.8 ± 0.2	0.11	79	39	-3.8	$\cdots$
Kim 2	$317.208^{+0.003}_{-0.004}$	$-51.162^{+0.001}_{-0.002}$	$0.39^{+0.15}_{-0.10}$	< 0.3	100	9	-2.3	$\cdots$
Phoenix II	$354.999^{+0.009}_{-0.007}$	$-54.407^{+0.007}_{-0.005}$	$1.79^{+0.41}_{-0.32}$	0.42	83	30	-2.93	$\cdots$
Pictoris I	70.95 ± 0.04	-50.28 ± 0.02	$1.82^{+1.41}_{-0.81}$	0.41	115	29	-3.38	$\cdots$
Reticulum II	53.93 ± 0.01	-54.048 ± 0.003	$6.17^{+0.32}_{-0.31}$	0.59	32	37	-3.9	$1.68^{+0.48}_{-0.47}$
Tucana II	$342.99^{+0.95}_{-0.05}$	$-58.60^{+0.02}_{-0.03}$	$15.67^{+2.13}_{-1.79}$	< 0.15	57	238	-6.1	$\cdots$
Tucana III	359.12 ± 0.03	-59.58 ± 0.01	$5.89^{+1.42}_{-1.00}$	0.3	24	38	-1.1	$1.56^{+0.73}_{-0.83}$
Tucana V	354.34 ± 0.02	-63.266 ± 0.008	$2.43^{+0.79}_{-0.56}$	0.42	55	24	-3.5	$\cdots$

3.4.1 Cetus II

Cetus II was discovered in the DES footprint in the DES Y2 data (4) as a lower-confidence candidate. The original structural parameters found for this object indicated that if a UFD, it would be the most compact and least luminous dwarf found (4). The results shown in Figure 3.7 indicate a significant increase in a_h and therefore with a much brighter absolute magnitude ($M_V = -1.3$). Given the large uncertainties on the shift in the centroid parameters, this increase should be treated with caution until further followup can be done. If these uncertainties can be resolved, then Cetus II is a potential candidate for IMF studies.

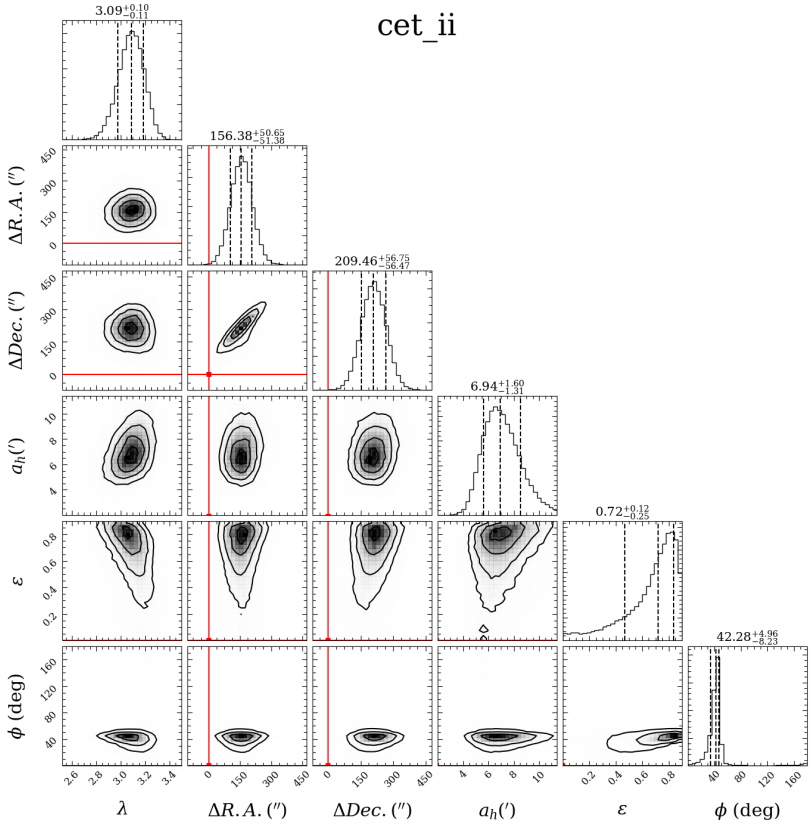

Figure 3.7: Posterior probability distributions for the structural and isochrone parameters of Cetus II obtained from an elliptical Plummer model and grid of PARSEC isochrones. The parameters explored were (from left to right): stellar richness (λ), Δ R.A. & Δ Dec. (these are the shifts from the centroid found in the literature), semi-major half-light radius (a_h), ellipticity (ϵ), position angle (ϕ). Dashed lines in the 1D histograms indicate 16th, 50th, and 84th quantiles of the median peak likelihood. The red lines represent current literature values.

3.4.2 Cetus III

Cetus III was found in the Hyper Suprime-Cam Subaru Strategic Program (HSC-SSP (82; 83)) (77). As was expected, this object was difficult to measure with DES data. It can be seen in the first panel of the second row of Figure 3.5 that the lower magnitude limit of DES data does not reach far enough below the MSTO. Figure 3.8 shows the lack of convergence.

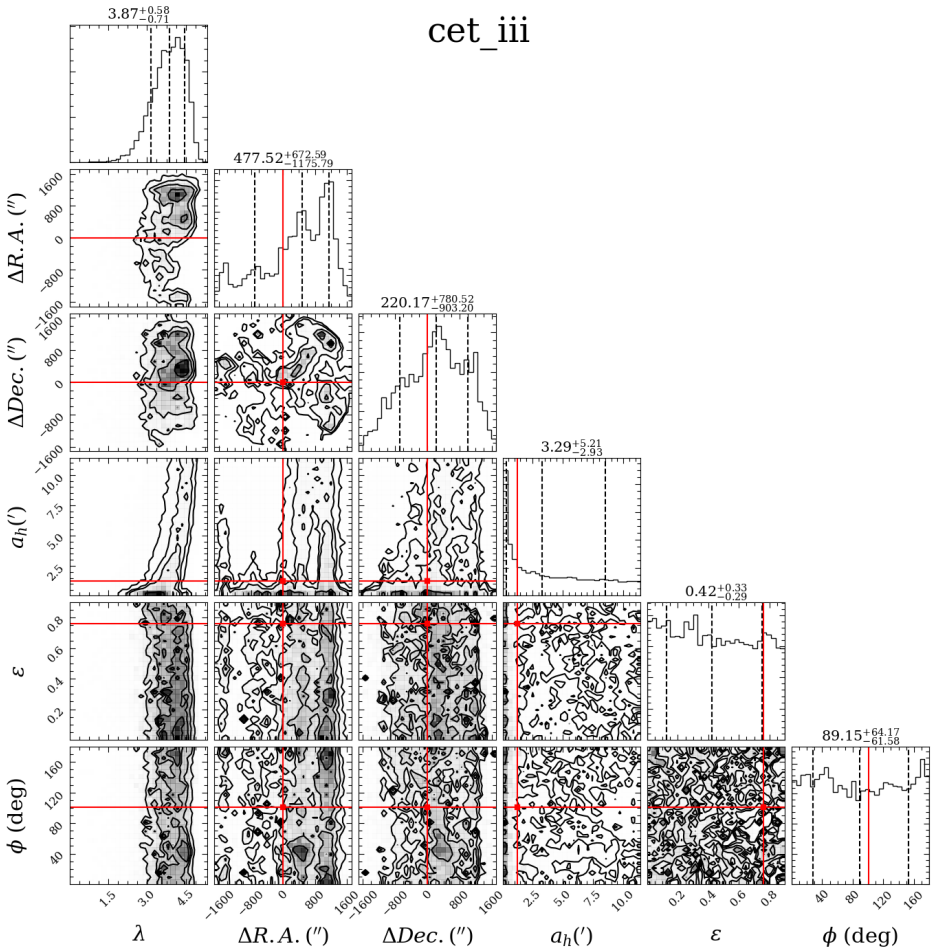

Figure 3.8: Posterior probability distributions for the structural and isochrone parameters of Cetus III. This figure is similar to Figure 3.7

3.4.3 Columba I

Columba I was observed with HSC in 2016 (78). Columba I appeared to be a typical old, metal-poor UFD and these results point to the same conclusion. All structural parameters are in agreement (within uncertainties) of previously found results, with the exception being the position angle. However, given the lack of clear convergence on an ellipticity value, this discrepancy is not surprising.

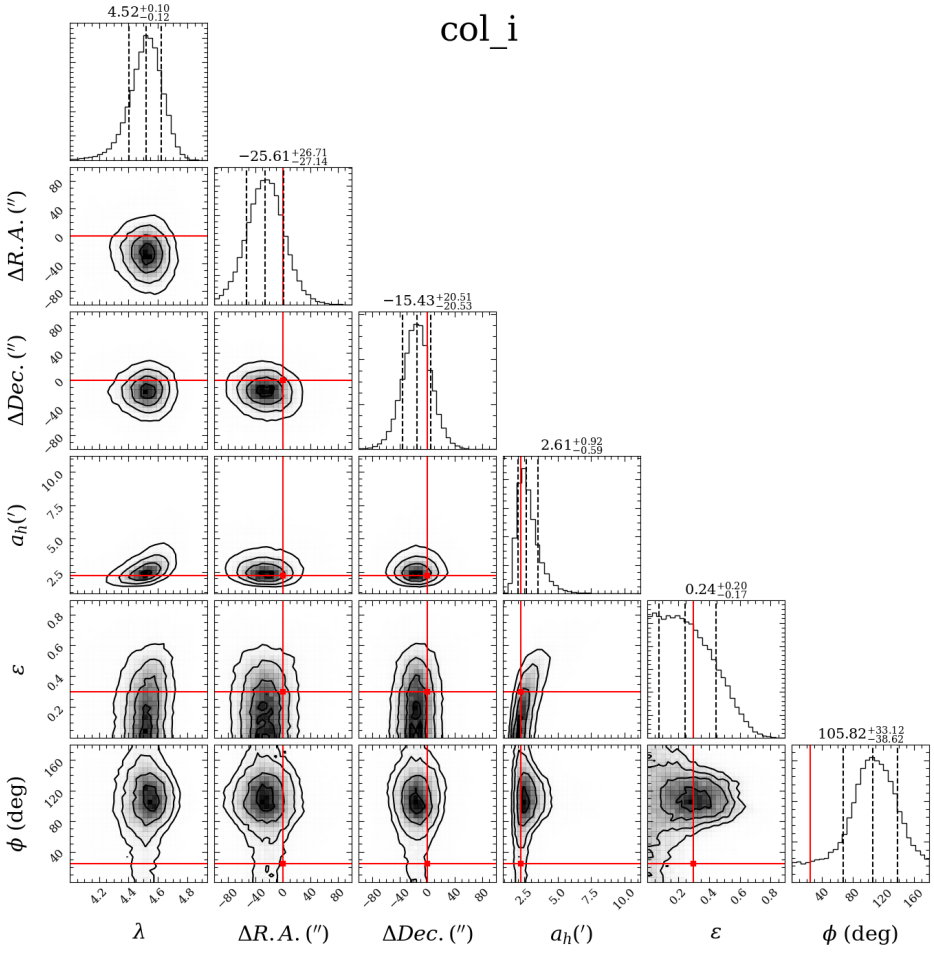

Figure 3.9: Posterior probability distributions for the structural and isochrone parameters of Columba I. This figure is similar to Figure 3.7

3.4.4 DES J0225+0304

DES J0225+0304 was found using the first two years of DES coadded data (79). Originally found to have a very small physical extent, it was located in the region of ambiguity between GCs and UFDs on the size-luminosity plane. While there might be some indication of an overdensity lower on the MS (see Figure A.4 at $g_0 \sim 22.5$), there is not enough information to confirm the existence of a UFD. To compliment this evidence, it can be seen in Figure 3.10 that there was no convergence in any of the structural parameters.

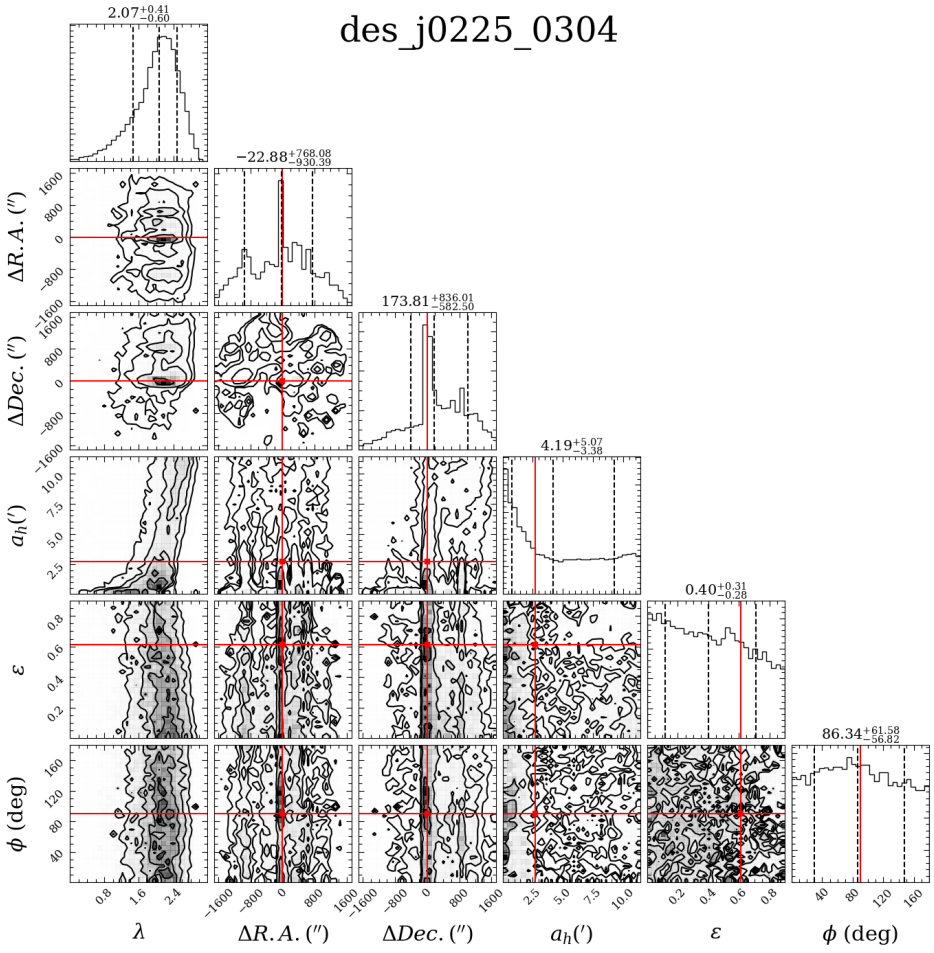

Figure 3.10: Posterior probability distributions for the structural and isochrone parameters of DES J0225+0304. This figure is similar to Figure 3.7

3.4.5 Eridanus II

Eridanus II was found in Year 1 of DES and analyzed by Koposov et al. (3) and the DES collaboration separately (20). Eridanus II is one of the most distant ($D = 363$ kpc) and one of the brightest ($M_V = -7.8$) UFDs found to date. The results depicted in Figure 3.11 show good agreement between our analysis and previously found results. At $g \sim 23$ there is a clear, well populated horizontal branch (see Figure A.5. While the limiting magnitude prohibits this object from being an IMF target, it nonetheless is a very interesting target for follow-up population studies.

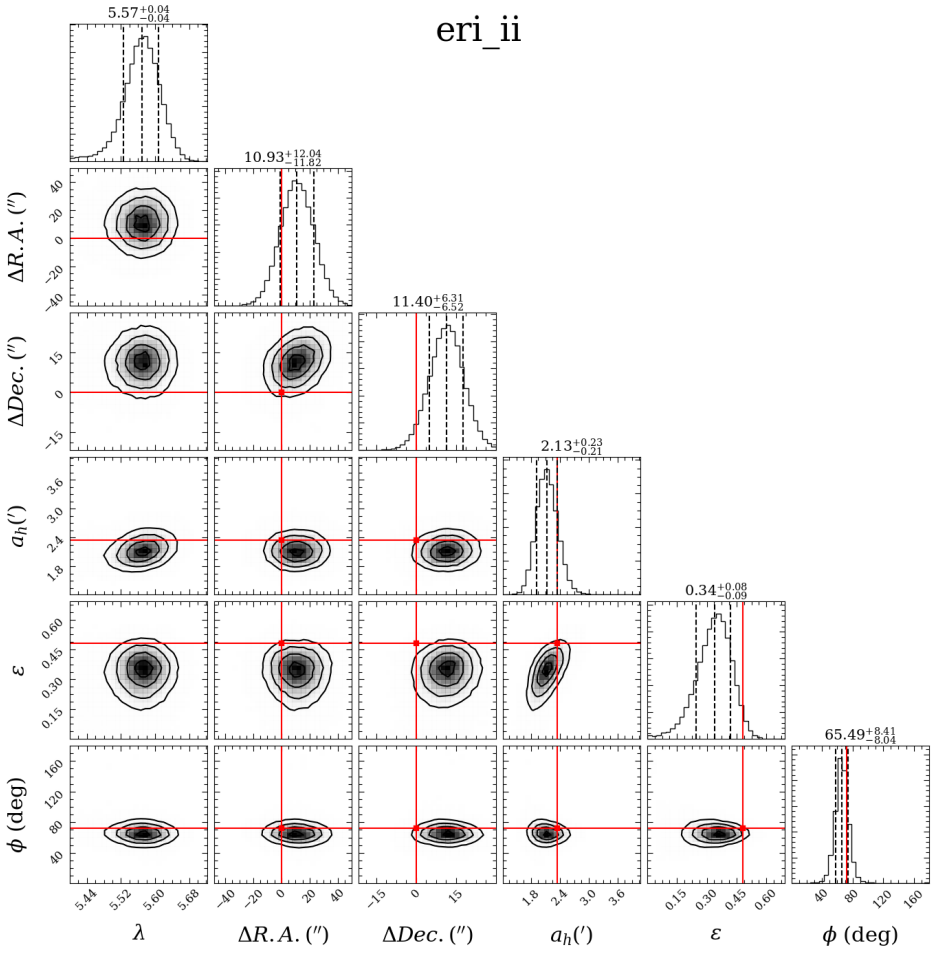

Figure 3.11: Posterior probability distributions for the structural and isochrone parameters of Eridanus II. This figure is similar to Figure 3.7

3.4.6 Eridanus III

Eridanus III was reported in Koposov et al. (3) and in the Y1 release of the DES collaboration (20). Those studies show a clear stellar population, however, its candidacy as a UFD is still open to interpretation. As seen in Figure A.6, there seem to be a faint RGB and top of the MSTO. This is in agreement with previous studies and given its repeatedly found small extent, it is likely a GC. The one thing to note is that with Y6_GOLD data we find Eridanus III to be smaller in extent than was previously thought (3) and slightly shifted in Dec.

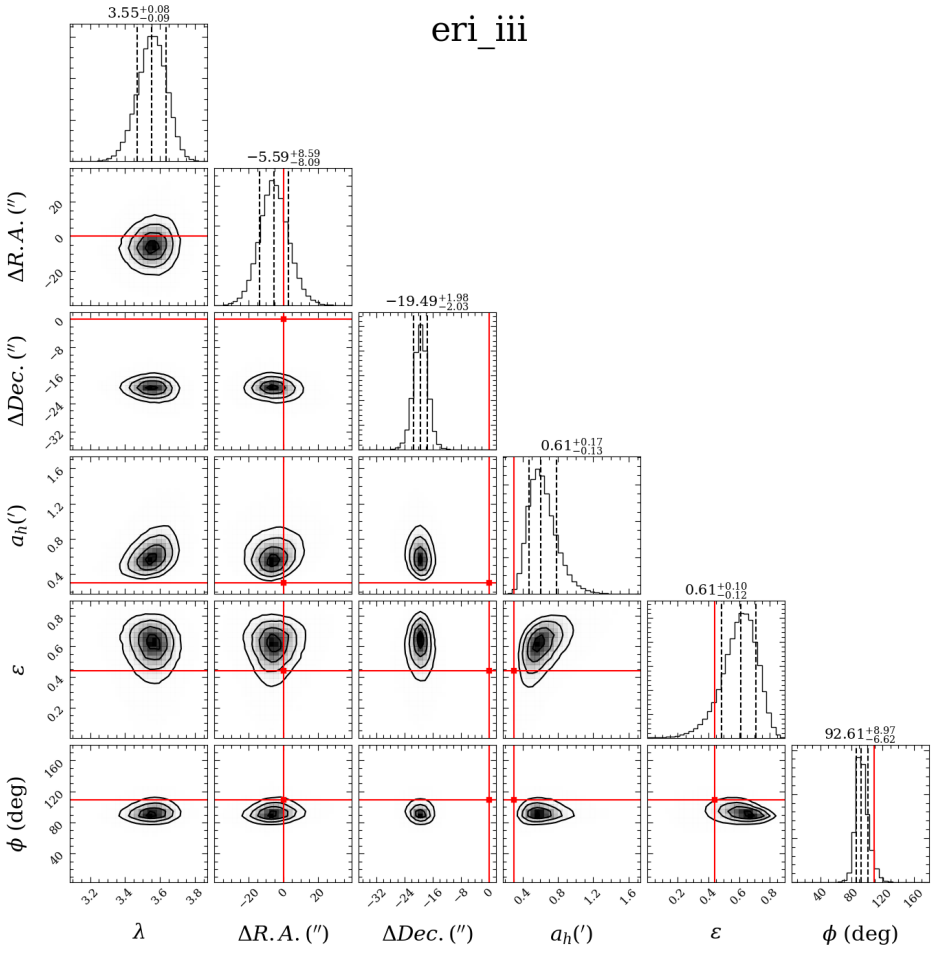

Figure 3.12: Posterior probability distributions for the structural and isochrone parameters of Eridanus III. This figure is similar to Figure 3.7

3.4.7 Grus I

This object has been the subject of many studies, including both spectroscopic and photometric follow-up (3; 10; 5; 12; 13). In the previous chapter, we conducted a follow-up study using Megacam data and a limited FOV, we found Grus I to be both larger and brighter than was previously thought. With this more precise data and wider FOV, this study finds Grus I to be smaller than before (Chapter 2) but still larger and brighter than previous studies.

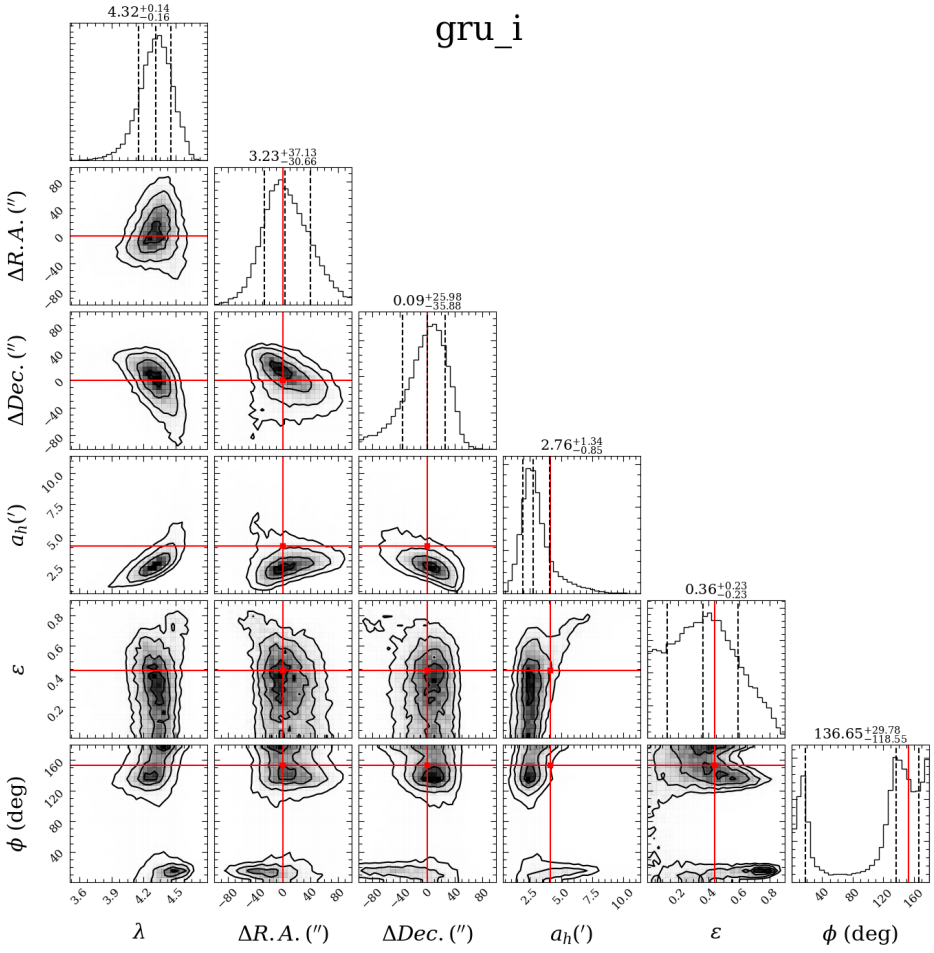

Figure 3.13: Posterior probability distributions for the structural and isochrone parameters of Grus I. This figure is similar to Figure 3.7

3.4.8 Grus II

Grus II was found in the Year 2 DES data as the most significant new UFD candidate (4). However, in the reprocessing a lot of the data in this part of the footprint was removed to increase uniformity and precision. There is some hint at a stellar population in both Figure 3.14 and Figure A.8. At $g \sim 21$, there is a potential sub-red giant branch. Follow up photometry or dedicated reprocessing of the DES data will be needed to further confirm the status of this candidate.

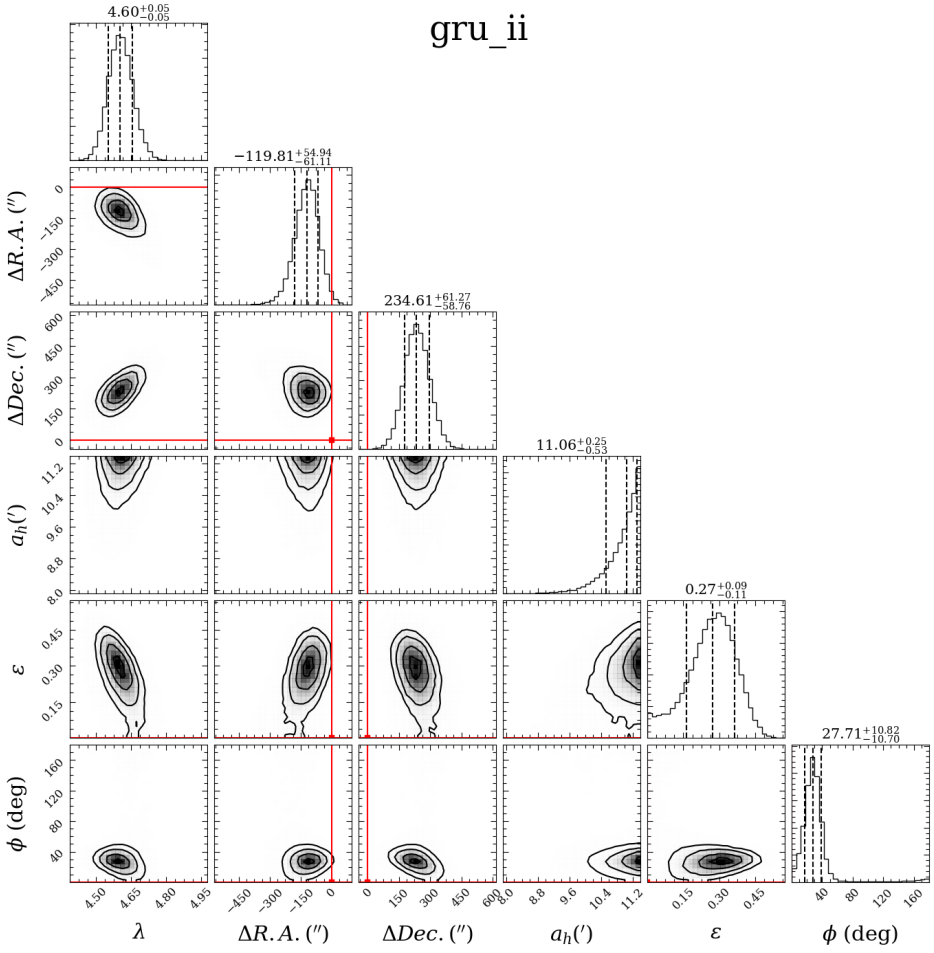

Figure 3.14: Posterior probability distributions for the structural and isochrone parameters of Grus II. This figure is similar to Figure 3.7

3.4.9 Horologium I

Horologium I was found with high significance in the DES Y1 coadded data by both Koposov et al (3) and the DES collaboration (20). Despite the ambiguity introduced due to its small size, it was classified as a UFD (3). We find it to be marginally larger and brighter at 40 pc in extent and with a $M_V = -3.9$ and agree that it is likely a UFD. Further, Horologium I has a very clear MSTO and RGC (see Figure A.9).

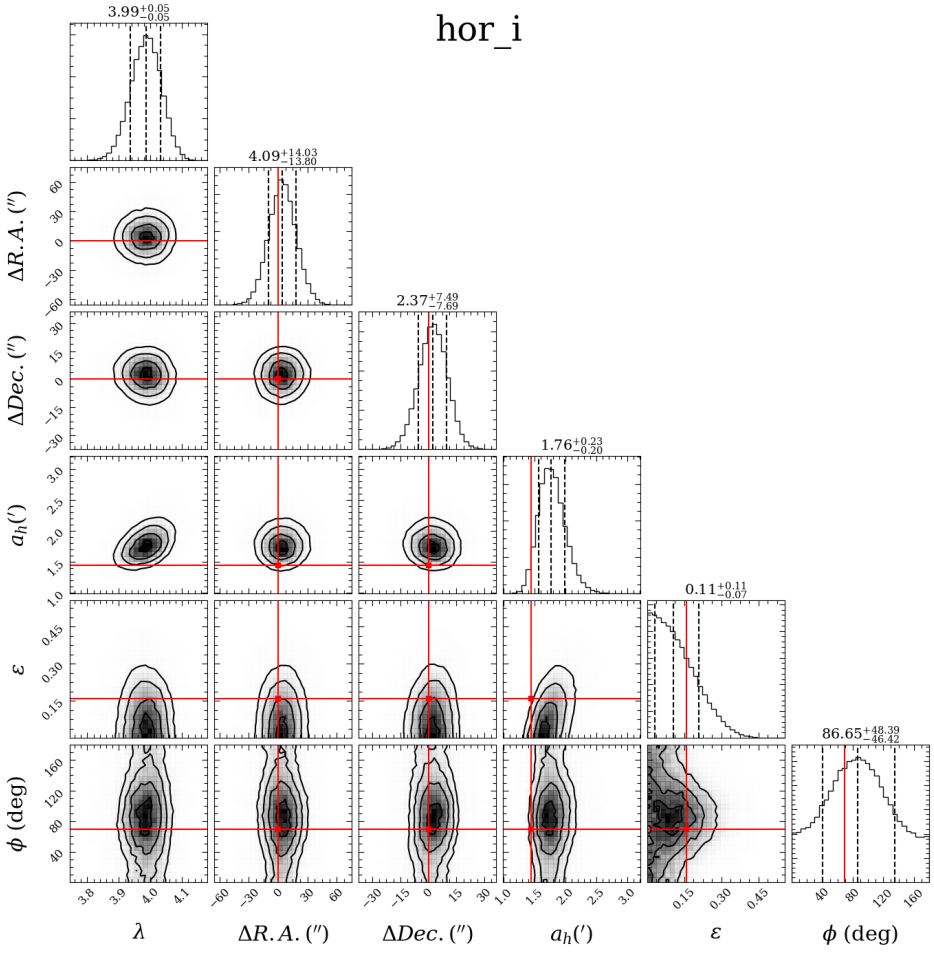

Figure 3.15: Posterior probability distributions for the structural and isochrone parameters of Horologium I. This figure is similar to Figure 3.7

3.4.10 Horologium II

Horologium II was discovered as a UFD candidate in the Y1A1 DES catalog (the first catalog to be produced) (81). It was found to be a faint, elongated object with a potential match to an old, metal-poor isochrone (13.5 Gyr, $[Fe/H] \sim -2.1$). It can be seen in Figure 3.16 that we are unable to recover an associated half-light radius for this object. Figure A.10 shows a potentially populated RGB and MSTO, but there is too much scatter to confidently say that this is a coherent stellar population. We recommend a targeted follow-up study to confirm the nature of this object.

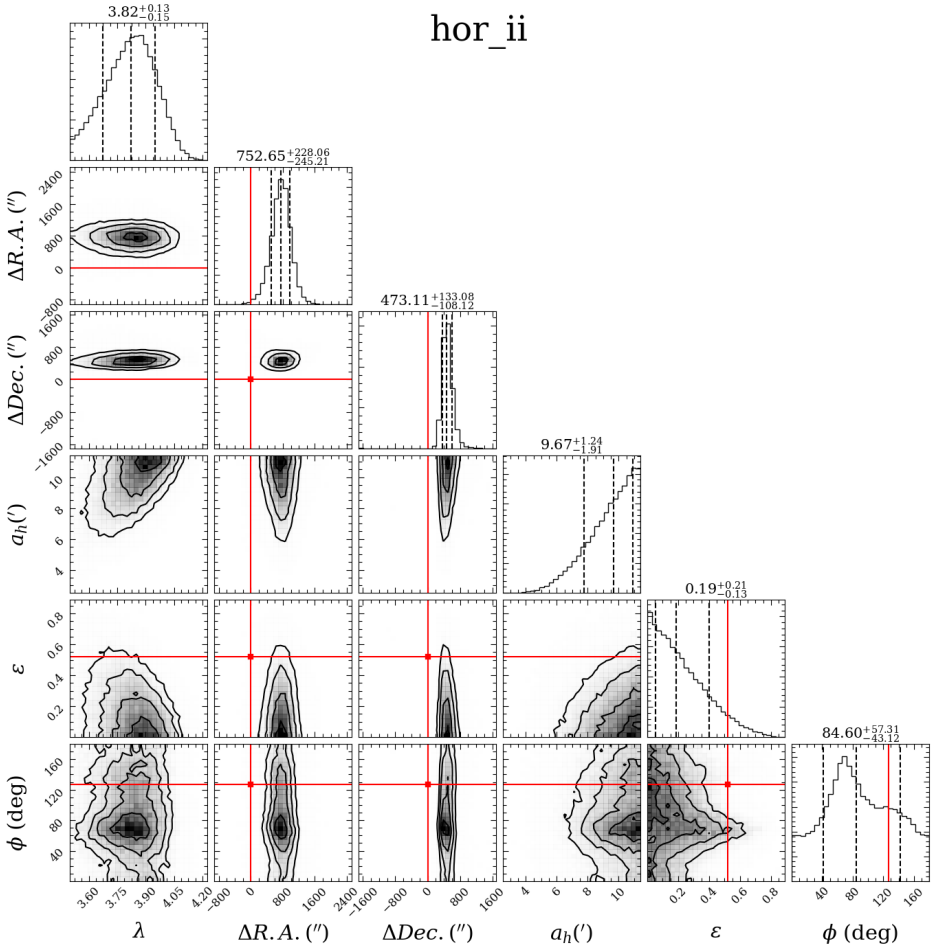

Figure 3.16: Posterior probability distributions for the structural and isochrone parameters of Horologium II. This figure is similar to Figure 3.7

3.4.11 Indus II

In agreement with our previous analysis (see chapter 2), this analysis shows that Indus II is likely neither a UFD or GC. Figure 3.17 shows a complete lack of convergence on any structural parameters. Figure A.11 still shows the features that flagged the object before.

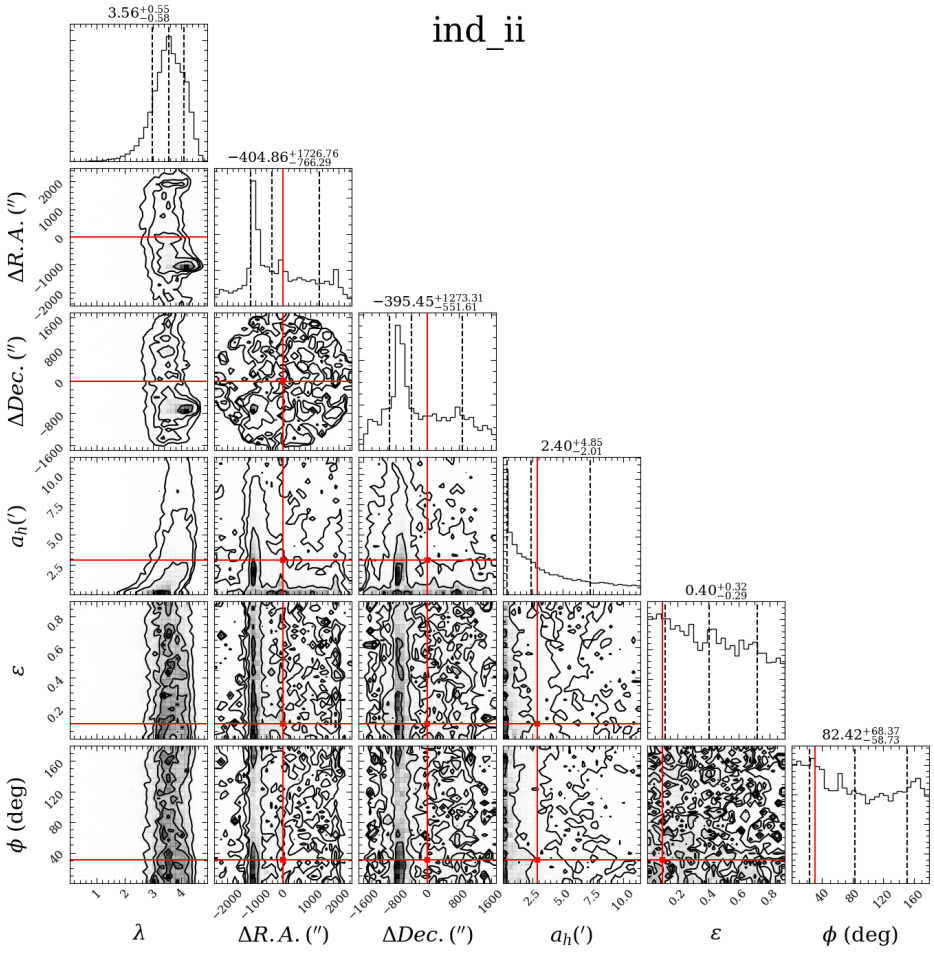

Figure 3.17: Posterior probability distributions for the structural and isochrone parameters of Indus II. This figure is similar to Figure 3.7

3.4.12 Kim 2

Kim 2 was discovered in an independent survey with DECam and followed up with targeted DECam data (81). It has been determined to likely be a larger star cluster as opposed to a UFD.

Our analysis supports the findings that this FOV contains a coherent stellar population (see Figure A.12), but is unlikely to be a UFD.

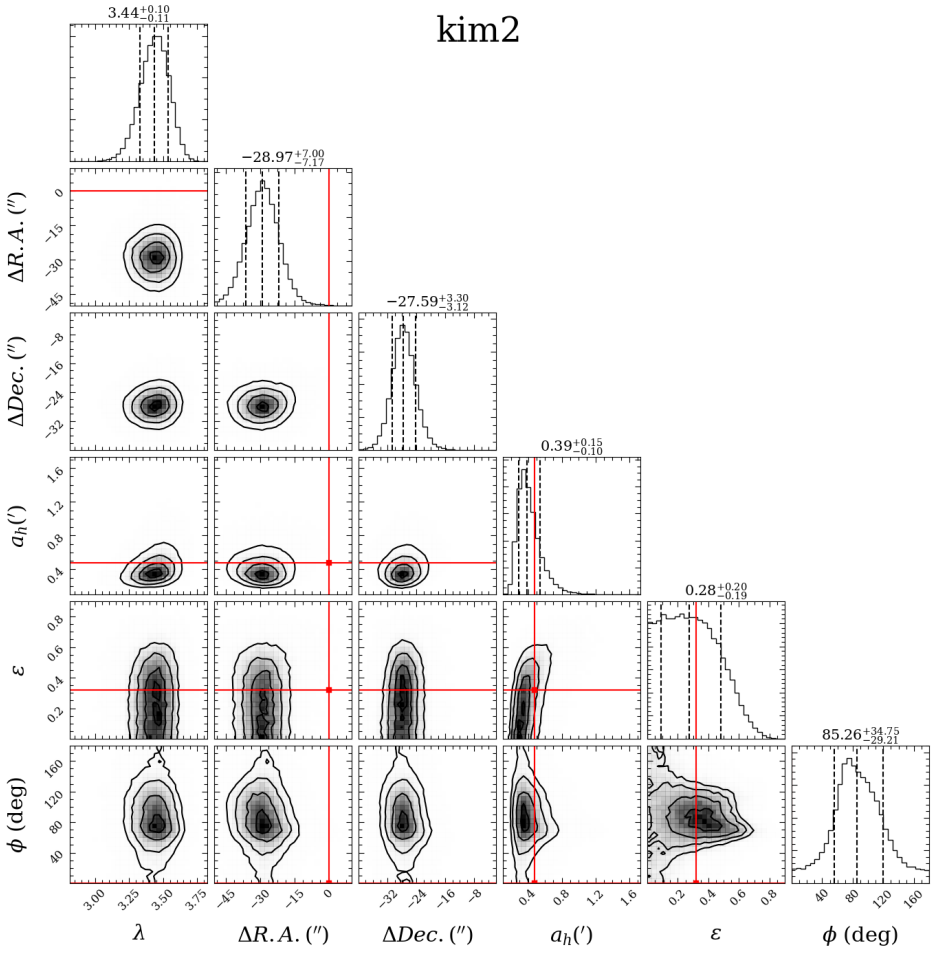

Figure 3.18: Posterior probability distributions for the structural and isochrone parameters of Kim 2. This figure is similar to Figure 3.7

3.4.13 Phoenix II

Phoenix II is a likely UFD based on discovery parameters (20; 3) and spectroscopy (84). This candidacy is also supported by the presence of an RR Lyrae star located on the horizontal branch (13). We present updated characteristics that are in very good agreement with previous studies (20; 3; 37).

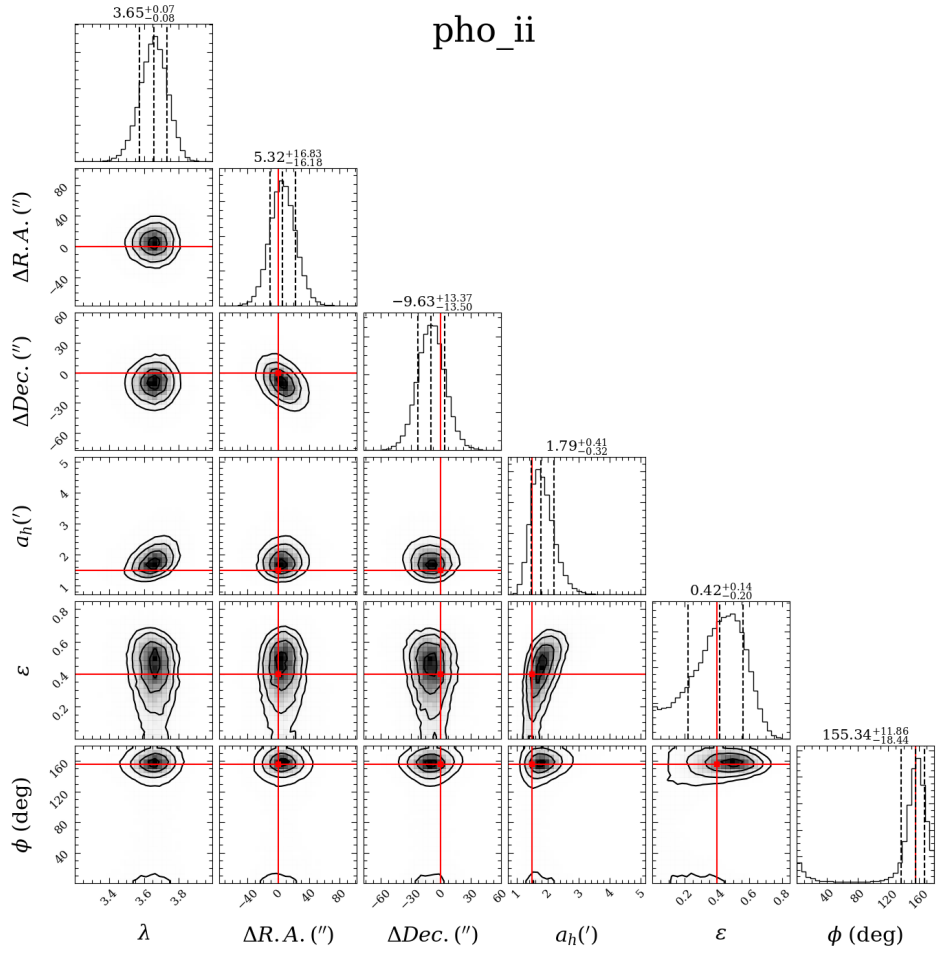

Figure 3.19: Posterior probability distributions for the structural and isochrone parameters of Phoenix II. This figure is similar to Figure 3.7

3.4.14 Pictoris I

Pictoris I was reported in Koposov et al. using DES Y1 data as a high confidence UFD (3). Unfortunately, this FOV suffers from large gaps in the data due to the reprocessing and more stringent quality control. Despite this Figure 3.20 shows some convergence on similar morphological properties as found previously. Additionally, it can be seen in Figure A.14 that there is a RGB and potential HB along with a MSTO.

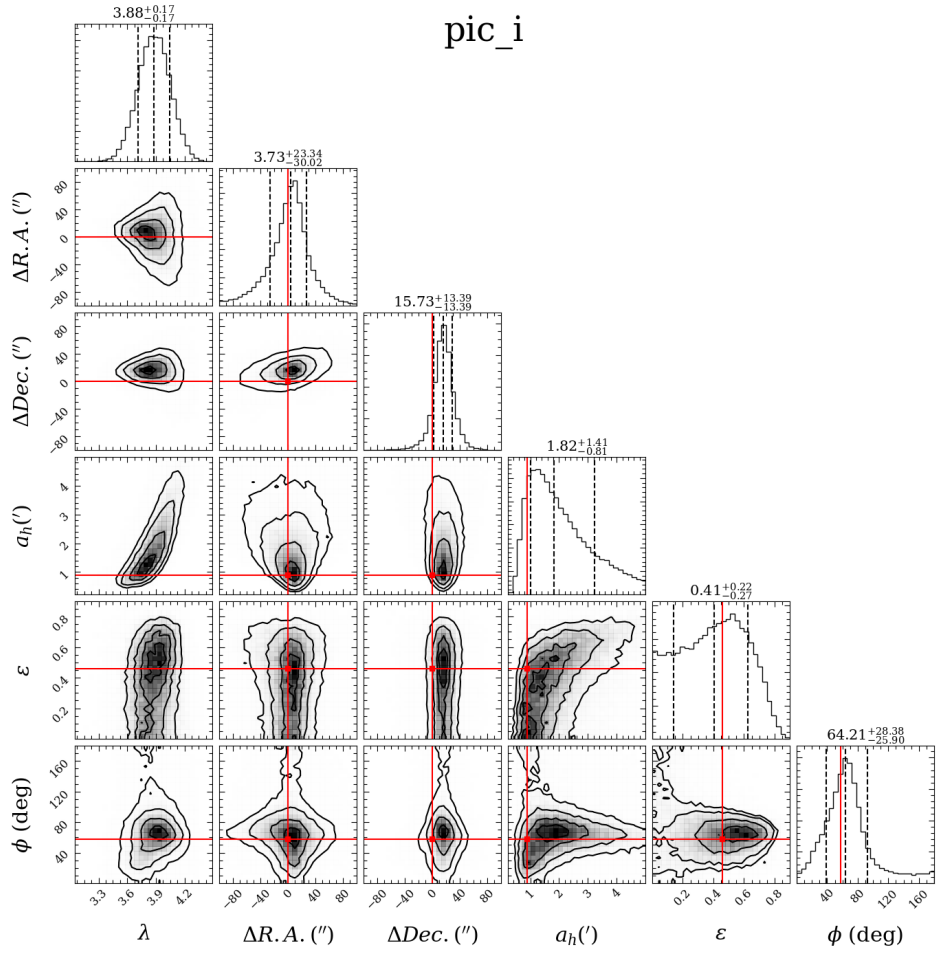

Figure 3.20: Posterior probability distributions for the structural and isochrone parameters of Pictoris I. This figure is similar to Figure 3.7

3.4.15 Reticulum II

Reticulum II was discovered in the Y1 DES footprint and classified as a candidate rather than a UFD due to its small size (3). However, its ellipticity and subsequent likelihood analyses pointed toward the object being a UFD (20). Follow-up spectroscopy has since confirmed its status as an UFD (10). Here we provide updated structural parameters as well as the slope of the IMF. In keeping with other IMF studies done on UFDs, Reticulum II hints at a "bottom-light" IMF.

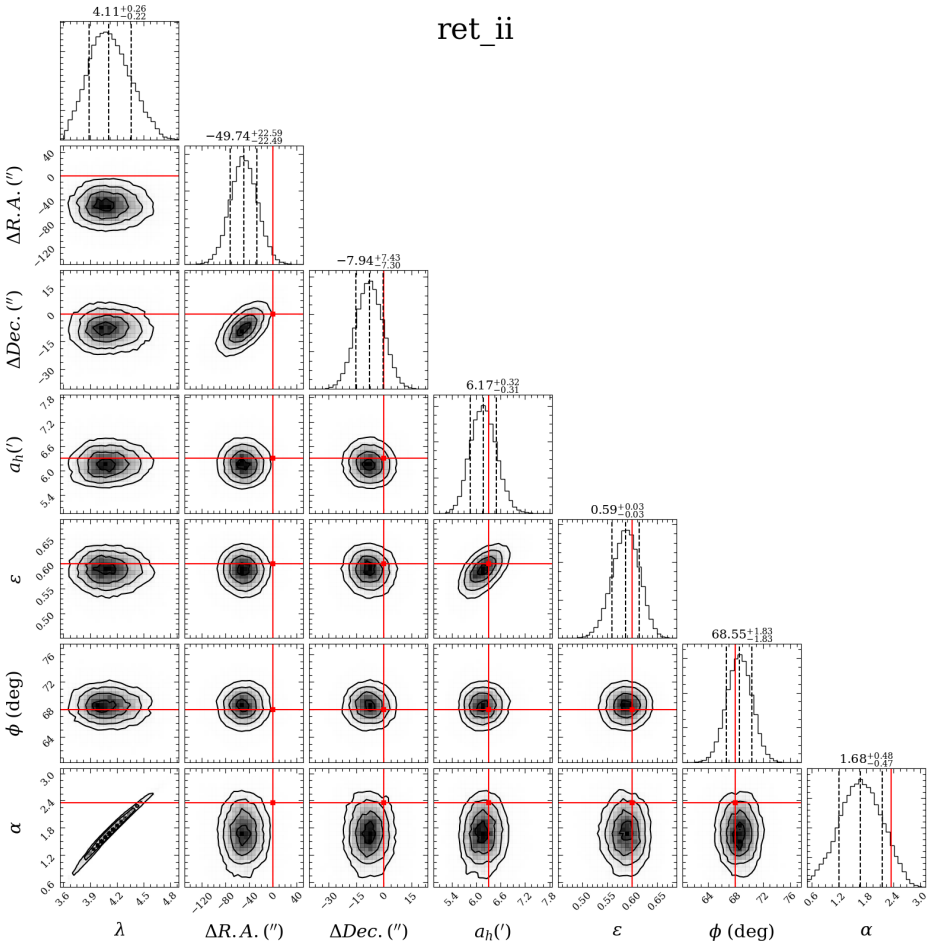

Figure 3.21: Posterior probability distributions for the structural and isochrone parameters of Reticulum II. This figure is similar to Figure 3.7 with the addition of the free parameter α, the slope of the IMF.

3.4.16 Reticulum III

Reticulum III was found in the DES Y2 and tentatively classed as a UFD based on it's potential BHB and RGB stars (85). Figure 3.22 shows a lack of convergence on r_h and a large uncertainty on the centroid parameters. There does seem to be some potential overdensity at the MSTO (see Figure A.16). This object would be worth either follow-up observation or further investigation using this data set.

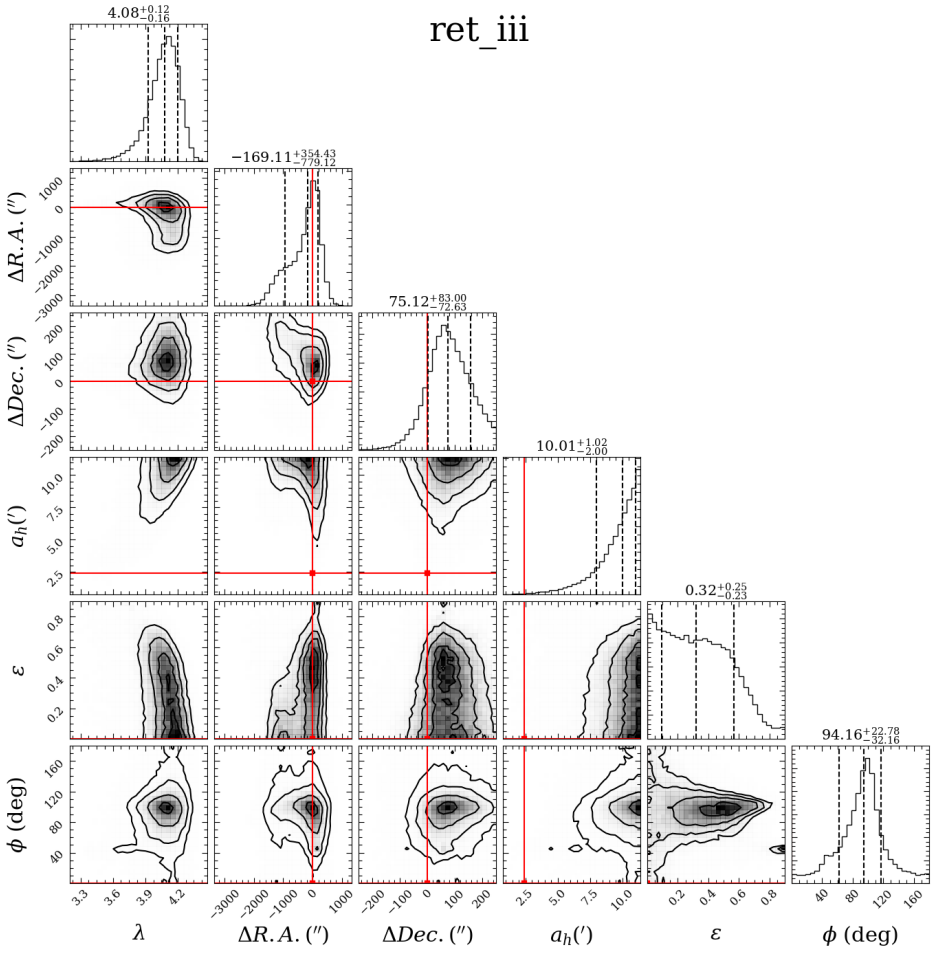

Figure 3.22: Posterior probability distributions for the structural and isochrone parameters of Reticulum III. This figure is similar to Figure 3.7

3.4.17 Tucana II

Tucana II was discovered in Y1 DES data as a high significance UFD candidate (4; 3). This object is well populated along the MSTO and RGB (see Figure A.17. With our updated properties we find this object to be larger than was previously thought. Recently, it was reported that some stars associated with Tucana II were further than expected (86). However, Figure 3.23 points toward a larger r_h than previously found.

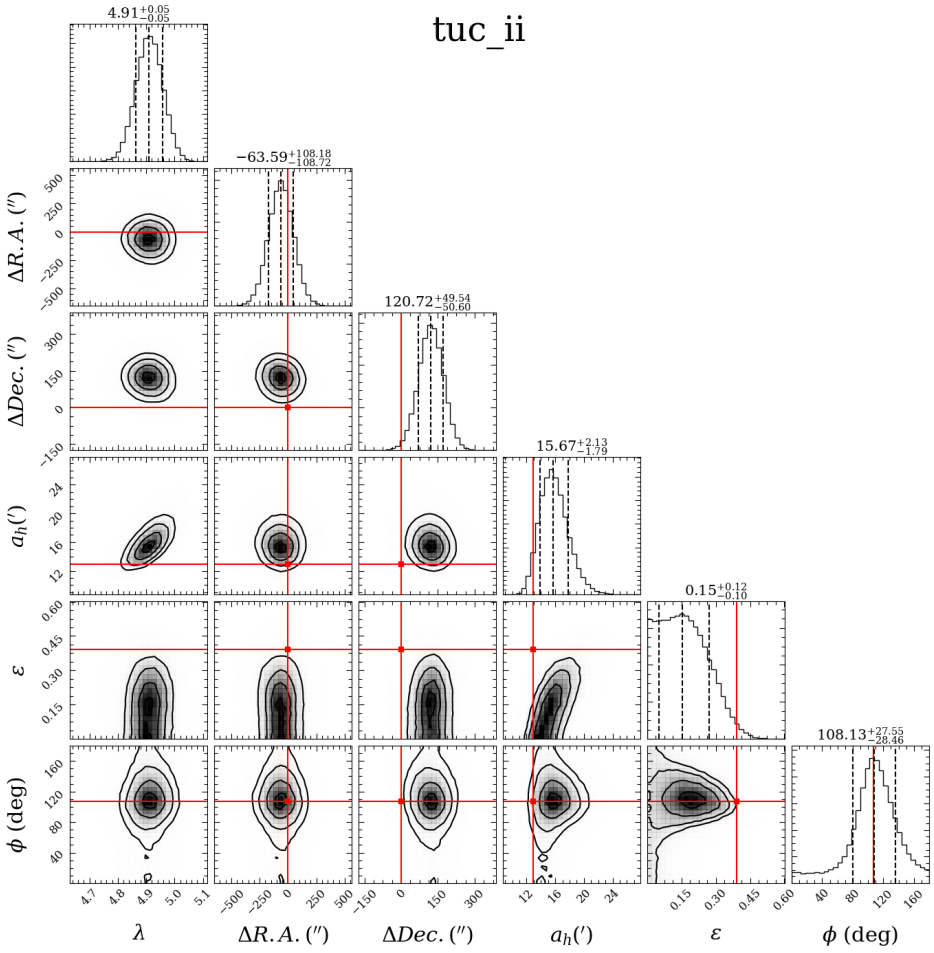

Figure 3.23: Posterior probability distributions for the structural and isochrone parameters of Tucana II. This figure is similar to Figure 3.7

3.4.18 Tucana III

Tucana III was found in the Y2 DES data release (4). Comparable in size to Reticulum II, its nearby proximity is also what made it a useful target to determine IMF slope constraints. Tucana III is well populated and resolved several magnitudes below its MSTO. We find updated structural parameters in keeping with previous studies and a shallower slope than the standard Salpeter of 2.35. This points toward a "bottom-light" IMF.

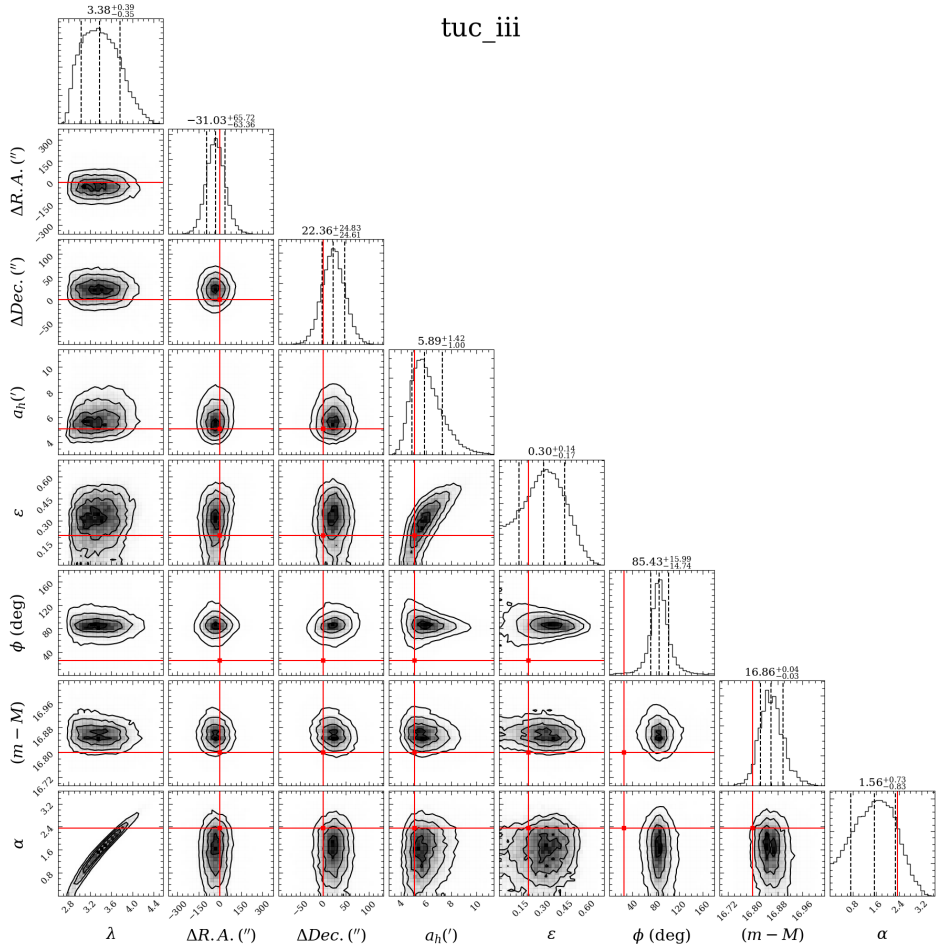

Figure 3.24: Posterior probability distributions for the structural and isochrone parameters of Reticulum II. This figure is similar to Figure 3.7 with the addition of the free parameter α, the slope of the IMF.

3.4.19 Tucana IV

Tucana IV was discovered in Y2 DES data (85). It is another large candidate with a reported extent of $\sim$ 127 pc. As shown in Figure 3.25, the half-light radius is difficult to constrain. This is due to a large gap in coverage near the center of the object. Despite this Figure A.19 shows a strong MSTO indicating that this is still a strong candidate. It is recommended to either perform follow-up observations or to rerun this analysis using data that does not include some of these quality cuts. Tucana IV shows strong candidacy for the IMF study if that gap can be filled.

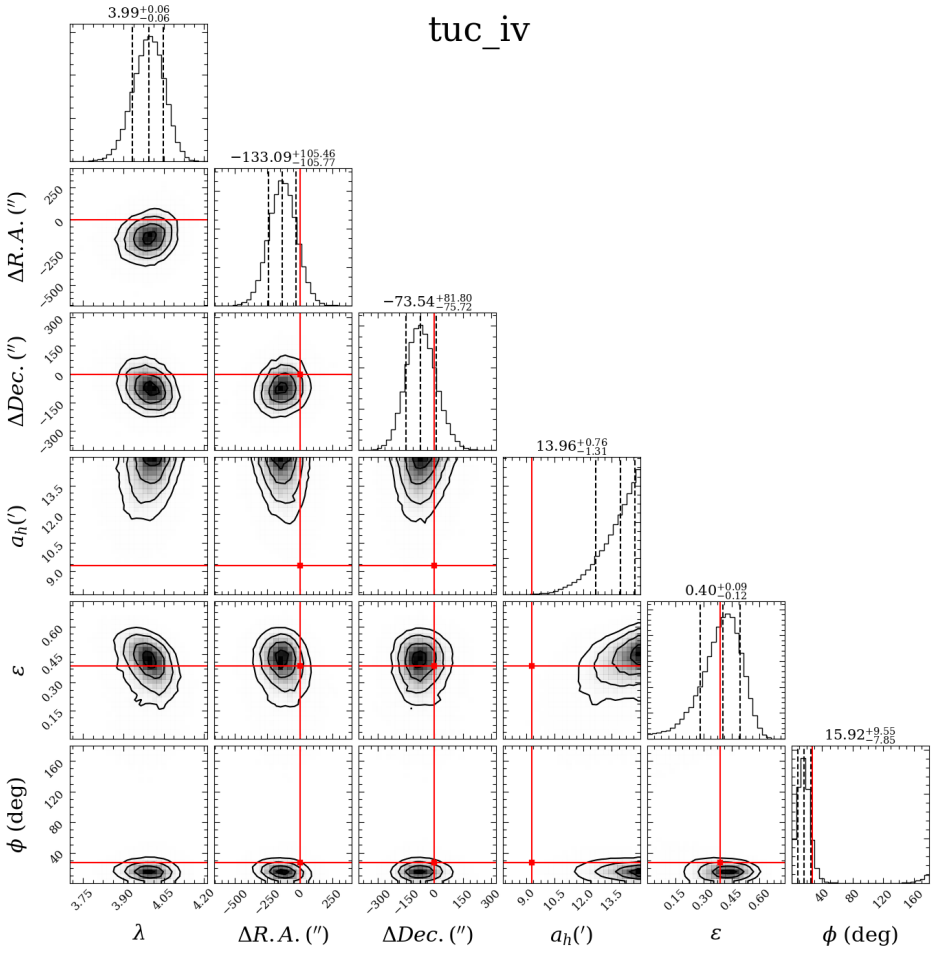

Figure 3.25: Posterior probability distributions for the structural and isochrone parameters of Tucana IV. This figure is similar to Figure 3.7

3.4.20 Tucana V

Tucana V was discovered in Y2 DES data as a faint, stellar system that was too extended and elliptical to be a GC (85). We find Tucana V to be brighter and less elliptical than was previously found. This would cast some ambiguity onto its nature as a UFD. It is clearly well populated below the MSTO (see Figure A.20, however we recommend that this object be the subject of targeted follow-up observation before confirming its status as a UFD

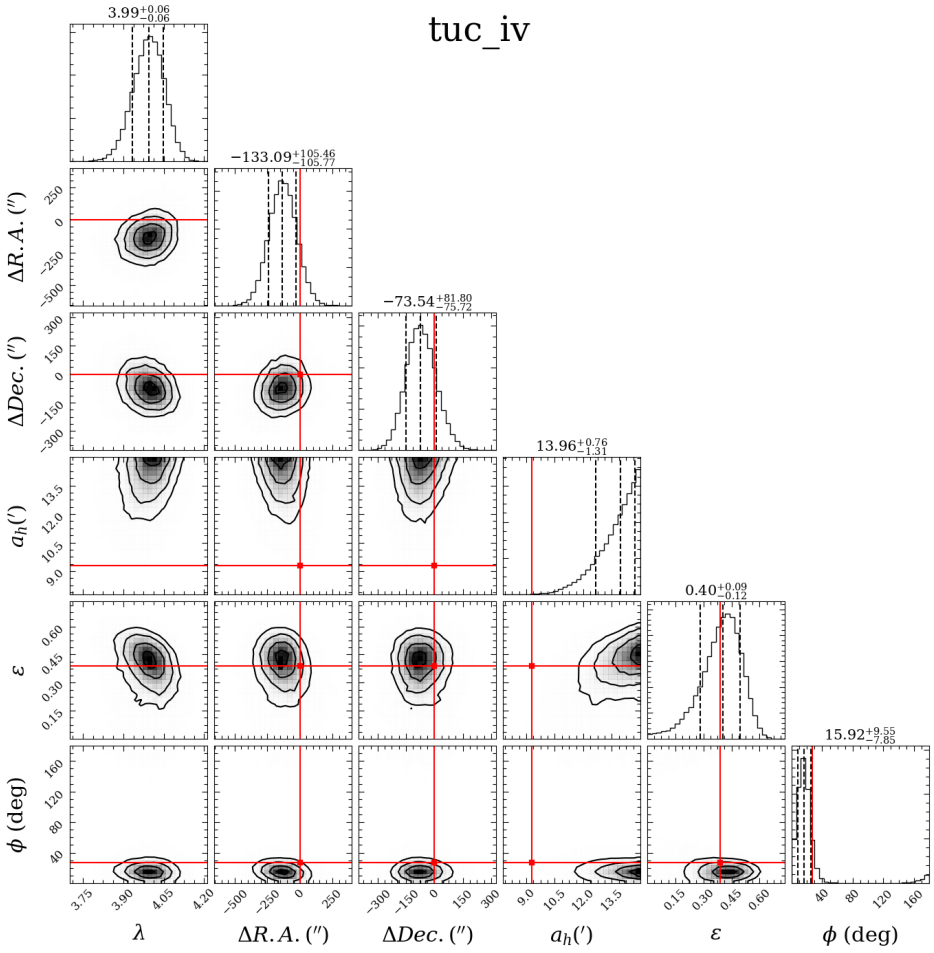

Figure 3.26: Posterior probability distributions for the structural and isochrone parameters of Tucana V. This figure is similar to Figure 3.7

3.5 Discussion

The difference between the literature values and our study of M_V, a_h, and distance (D) is shown in Figure 3.27. It can be seen that most of the objects have very little shift. It is interesting to note that we find Tuc II to be slightly larger than before. There has been some speculation that some of its member stars are further than expected (based on the previous halflight radius (86).

Another interesting result that can be seen in Figure 3.27 is Cetus II. Cetus II should have dedicated follow-up to determine the actual size of the object. The FOV centered on Indus II was again found not to have a stellar population indicative of a UFD or GC.

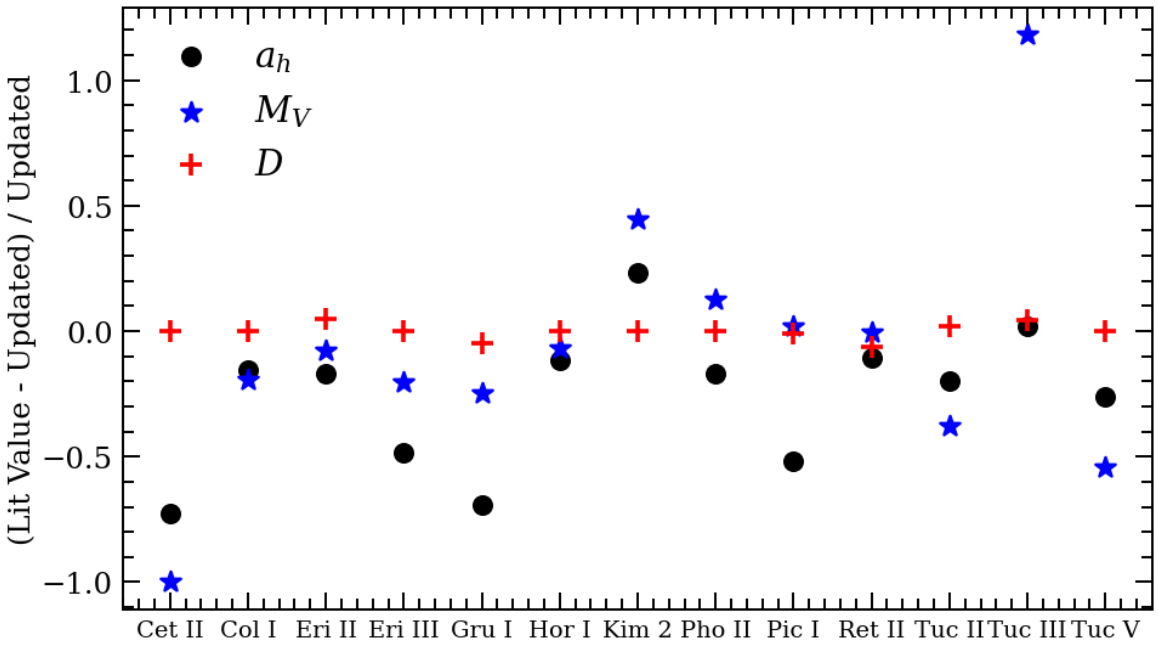

Figure 3.27: The difference between all of the objects listed in Table 3.3 and their original literature values. For readability, only a_h (the black dots), M_V (the blue star), and D (the distance in kpc, the red plus) are listed here.

Figure 3.28 shows the range of α for all UFDs that have IMF measurements. It is clear that though they all are shallower than the Salpeter IMF, there's still significant variation among them. It should also be noted that although the uncertainties aren't reported here, most are only significantly different than the Salpeter IMF to 1σ.

Figure 3.29 explores the potential relationship between average metallicity and IMF. There is a hint of a correlation in this figure, but it really points toward the need for more UDF IMFs. It has been speculated before that there may also be a correlation between distance and slope (70). Although Ret II and Tuc III have a steeper slop than the furthest UFDs (Hercules, Leo IV, and CVn II), they are not the steepest as compared to some others that they are closer than. Again, it proves necessary for more UFDs to be analyzed to make definitive statements. Hopefully when JWST and the Vera Rubin Observatory come online, we will be able to probe deeper on a few of these objects that are just slightly too faint to have the proper mass range.

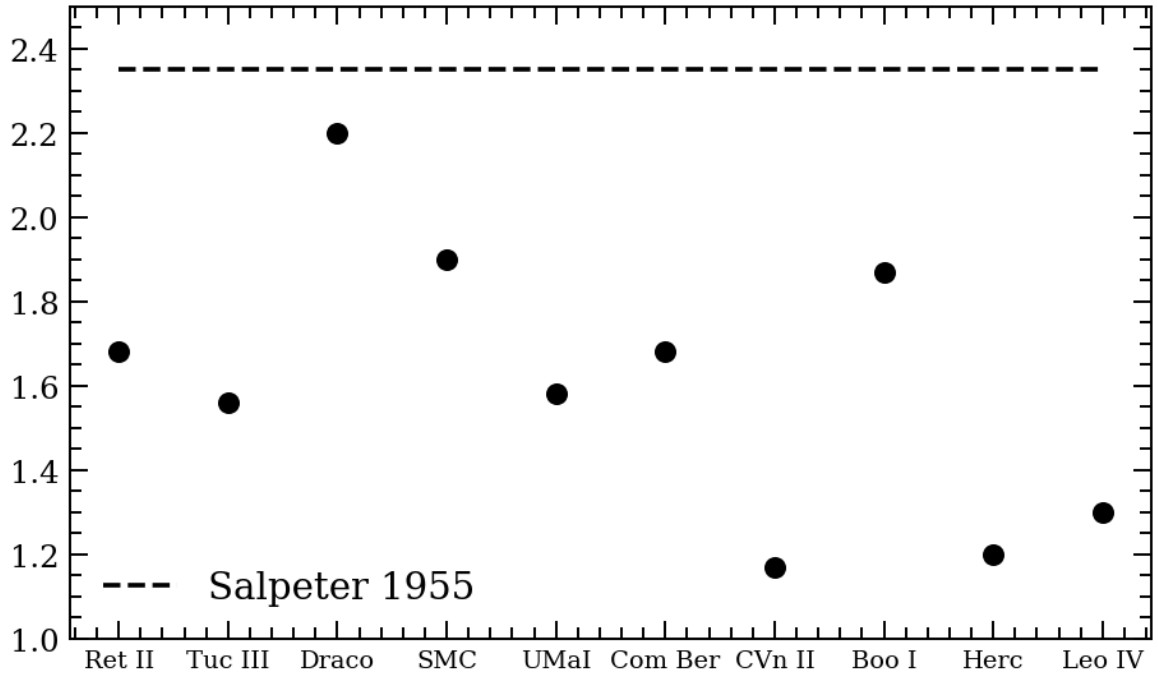

Figure 3.28: Comparison of all the dwarf galaxies with IMF measurements (power-law form). The dashed line is the Salpeter IMF.

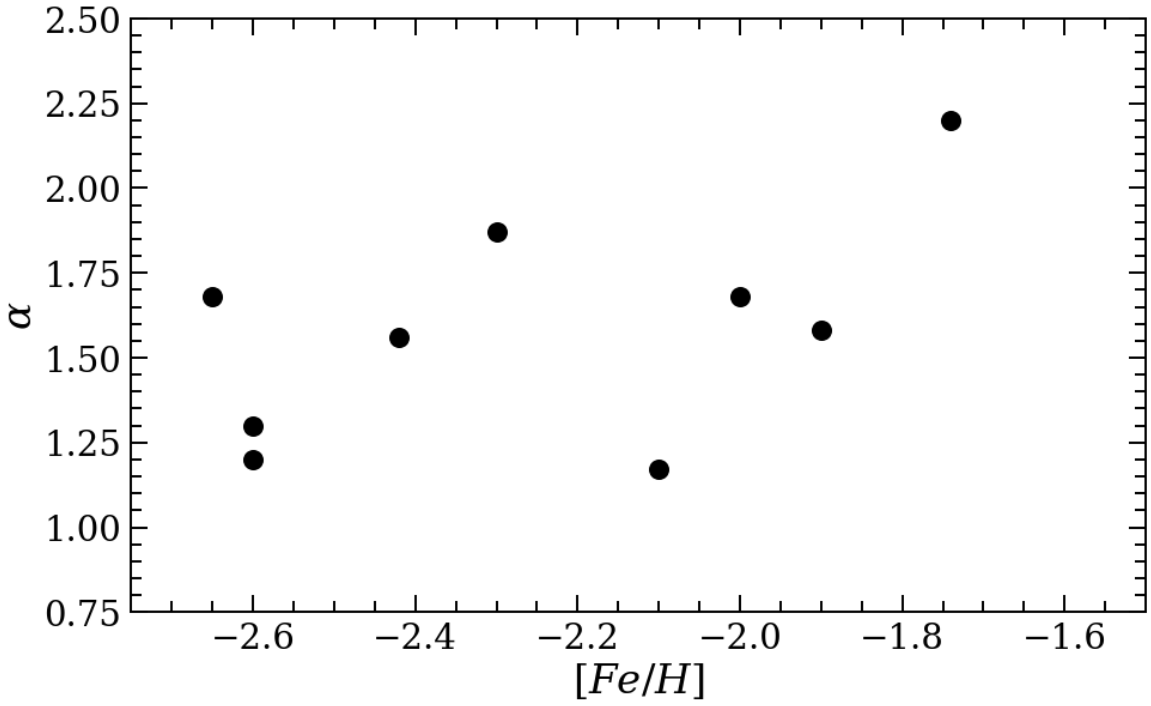

Figure 3.29: IMF slope vs. average metallicity of all the dwarf galaxies with IMF measurements (power-law form).

4. SUMMARY AND CONCLUSIONS

With this thesis, I have contributed to the larger astronomy community by improving our understanding of the physical properties of local Ultra-faint Dwarf galaxies. I have added to the small, but growing, catalog of IMF information for UFDs. Given the small number of objects within the UFD population it is ever imperative that they are characterized accurately and precisely. The open questions in the field that I addressed were two-fold in most cases: what is the nature of a target object and does our method work given the noise and small size of our targets.

4.1 The Nature of UFD Candidates

In Chapter 2, I used targeted, deep follow-up photometry to explore the nature of two UFD candidates within the DES footprint, Grus I and Indus II. These objects were chosen due to their low-confidence and ambiguous nature. We used Magellan/Megacam imaging for its large FOV ($24' \times 24'$)—at the time, the largest FOV for data that deep. We obtained coadded images in g- and r-band with $\sim 0.64''$ seeing.

The first step was to obtain the data from reduced images by performing point-spread function photometry. PSF photometry was chosen due to both the crowded nature of the field and due to some tracking issues that changed the shape of the data. I was able to overcome the fitting issues due to the elongation in the g-band images of Grus I and obtain deep photometry. The resulting photometry allowed us to probe ~ 2 magnitudes fainter than was previously done. As part of the DES collaboration, I have access to phenomenal photometry. I used this photometry to calibrate the follow-up photometry to $1 - 2\%$ uncertainties. The photometry, photometric uncertainties, and spatial information from this was used in a statistical analysis to infer information about the physical properties of Grus I and Indus II.

I chose to use an MCMC algorithm to take advantage of every data point (i.e., stellar magnitudes and positions). By doing so, I avoided the need to bin data and lose information in the process. This is important due to the small size of UFDs in general and the noise associated with

probing deep into faint objects.

I utilized the toolkit called `UGaLi` to implement the MCMC algorithm. `UGaLi` was created for the search and characterization of small stellar overdensities in the Milky Way by DES. I defined the probability distribution function by an elliptical Plummer distribution for the spatial component. This was characterized by five morphological parameters. The probability distribution function of the isochrone parameters was created by forward-modeling over a grid of isochrone templates.

The results from this analysis helped determine that Grus I was a UFD and that Indus II was a false positive. Additionally, I was able to provide updated physical characteristics that shifted the position of Grus I in the size-luminosity plane.

4.2 Characterization of UFDs

In Chapter 3, I accomplished several things: I updated the physical properties of a large portion of the population of UFDs, I developed a method for inferring the slope of the IMF of UFDs, and I found the slope of a couple of UFDs. Starting with a target list of 20 objects, I used data from the latest DES Y6_GOLD to perform a similar analysis as was done in Chapter 2.

The Y6_GOLD catalog is arguably an unprecedented achievement in photometric precision and uniformity. By updating the catalog of UFD characteristics with this data set, I have provided uniform constraints on several physical relationships that help us understand these objects, classify them, and disentangle their physical properties and origins from that of other astronomical objects. There were 20 targets that fell within the DES footprint. Of those 20, I was able to provide updated characteristics on 13 objects. Of the objects that I was unable to provide updated constraints on, some (such as Indus II) are now confirmed false positives. Others (such as Cetus III) are simply too faint to be analyzed reliably.

For the objects that have updated characteristics, I also have assigned membership probabilities for each star in the FOV. These membership probabilities are used to target individual stars for spectroscopic follow-up. Spectroscopic follow-up is the most reliable way to classify a UFD and determine its metallicity and kinematics.

4.3 Characterization of the IMF

Next in Chapter 3, I determined which of the UFDs were viable IMF targets. To do this, I simulated several different data sets representing UFDs of varying size, total mass, and IMF. I used these simulated datasets to ensure that I could recover the input IMF and other physical properties. These simulated data sets were also assigned a photometric uncertainty in keeping with the Y6_GOLD data set. By doing this, I was able to determine observational limitations on our analysis.

I determined that below a magnitude of $g \sim 24$, the star galaxy separation broke down and the photometric uncertainties became too large to return appropriate results. Additionally, I determined that applying appropriate color cuts in color-magnitude space was necessary to limit background contamination. On the other hand, I found that it was best to include all bright magnitude information to properly constrain and subtract the foreground/background contamination. I also determined that it was best to have resolved stars down to at least three magnitudes below the MSTO in order to recover the IMF slope.

For this study, I chose Reticulum II and Tucana III based on their proximity, size, and how well populated they were below the MSTO. For both objects, I found an IMF slope that is shallower than the standard Salpeter IMF that is found in the MW. This implies a "bottom-light" IMF which translates to stars below the MSTO (or very low on the MS) not dominating the system. Alternatively, a "bottom-light" IMF could imply a "top-heavy" IMF. And for objects as old as these, most of those stars could be gone by now, potentially leaving behind observable signals to search for.

One of the biggest open questions in astronomy is "Is the IMF universal?" If we continue to find more UFDs with these shallower IMF slopes, while more massive and extragalactic object's seem to have steeper slopes—the answer would appear to be no. Which begs the question, what exactly determines the IMF at an objects birth? Further, how much variance in the IMF is there within these smaller populations.

Previously, IMF studies were limited to space-based data. These placed huge limitations on using the UFD population to contribute to IMF studies both in terms of telescope time and FOV.

UFDs are often much bigger than the FOV of the Hubble Space Telescope.

By accomplishing this analysis with ground-based data, I have proved undeniably that this method works. As astronomy heads into the survey data era, our photometry will get deeper and more precise. The `UGaLi` toolkit is now equipped to work immediately and with little adjustment or preparation on obtaining IMF constraints.

REFERENCES

[1] Astropy Collaboration, T. P. Robitaille, E. J. Tollerud, P. Greenfield, M. Droettboom, E. Bray, T. Aldcroft, M. Davis, A. Ginsburg, A. M. Price-Whelan, W. E. Kerzendorf, A. Conley, N. Crighton, K. Barbary, D. Muna, H. Ferguson, F. Grollier, M. M. Parikh, P. H. Nair, H. M. Unther, C. Deil, J. Woillez, S. Conseil, R. Kramer, J. E. H. Turner, L. Singer, R. Fox, B. A. Weaver, V. Zabalza, Z. I. Edwards, K. Azalee Bostroem, D. J. Burke, A. R. Casey, S. M. Crawford, N. Dencheva, J. Ely, T. Jenness, K. Labrie, P. L. Lim, F. Pierfederici, A. Pontzen, A. Ptak, B. Refsdal, M. Servillat, and O. Streicher, "Astropy: A community Python package for astronomy," , vol. 558, p. A33, Oct. 2013.

[2] Astropy Collaboration, A. M. Price-Whelan, B. M. Sipőcz, H. M. Günther, P. L. Lim, S. M. Crawford, S. Conseil, D. L. Shupe, M. W. Craig, N. Dencheva, A. Ginsburg, J. T. Vand erPlas, L. D. Bradley, D. Pérez-Suárez, M. de Val-Borro, T. L. Aldcroft, K. L. Cruz, T. P. Robitaille, E. J. Tollerud, C. Ardelean, T. Babej, Y. P. Bach, M. Bachetti, A. V. Bakanov, S. P. Bamford, G. Barentsen, P. Barmby, A. Baumbach, K. L. Berry, F. Biscani, M. Boquien, K. A. Bostroem, L. G. Bouma, G. B. Brammer, E. M. Bray, H. Breytenbach, H. Buddelmeijer, D. J. Burke, G. Calderone, J. L. Cano Rodríguez, M. Cara, J. V. M. Cardoso, S. Cheedella, Y. Copin, L. Corrales, D. Crichton, D. D'Avella, C. Deil, É. Depagne, J. P. Dietrich, A. Donath, M. Droettboom, N. Earl, T. Erben, S. Fabbro, L. A. Ferreira, T. Finethy, R. T. Fox, L. H. Garrison, S. L. J. Gibbons, D. A. Goldstein, R. Gommers, J. P. Greco, P. Greenfield, A. M. Groener, F. Grollier, A. Hagen, P. Hirst, D. Homeier, A. J. Horton, G. Hosseinzadeh, L. Hu, J. S. Hunkeler, Ž. Ivezić, A. Jain, T. Jenness, G. Kanarek, S. Kendrew, N. S. Kern, W. E. Kerzendorf, A. Khvalko, J. King, D. Kirkby, A. M. Kulkarni, A. Kumar, A. Lee, D. Lenz, S. P. Littlefair, Z. Ma, D. M. Macleod, M. Mastropietro, C. McCully, S. Montagnac, B. M. Morris, M. Mueller, S. J. Mumford, D. Muna, N. A. Murphy, S. Nelson, G. H. Nguyen, J. P. Ninan, M. Nöthe, S. Ogaz, S. Oh, J. K. Parejko, N. Parley, S. Pascual, R. Patil, A. A. Patil, A. L. Plunkett, J. X. Prochaska, T. Rastogi, V. Reddy Janga, J. Sabater, P. Sakurikar,

M. Seifert, L. E. Sherbert, H. Sherwood-Taylor, A. Y. Shih, J. Sick, M. T. Silbiger, S. Singanamalla, L. P. Singer, P. H. Sladen, K. A. Sooley, S. Sornarajah, O. Streicher, P. Teuben, S. W. Thomas, G. R. Tremblay, J. E. H. Turner, V. Terrón, M. H. van Kerkwijk, A. de la Vega, L. L. Watkins, B. A. Weaver, J. B. Whitmore, J. Woillez, V. Zabalza, and Astropy Contributors, "The Astropy Project: Building an Open-science Project and Status of the v2.0 Core Package," , vol. 156, p. 123, Sept. 2018.

[3] S. E. Koposov, V. Belokurov, G. Torrealba, and N. W. Evans, "Beasts of the Southern Wild: Discovery of Nine Ultra Faint Satellites in the Vicinity of the Magellanic Clouds.," , vol. 805, p. 130, Jun 2015.

[4] A. Drlica-Wagner, K. Bechtol, E. S. Rykoff, E. Luque, A. Queiroz, Y. Y. Mao, R. H. Wechsler, J. D. Simon, B. Santiago, B. Yanny, E. Balbinot, S. Dodelson, A. Fausti Neto, D. J. James, T. S. Li, M. A. G. Maia, J. L. Marshall, A. Pieres, K. Stringer, A. R. Walker, T. M. C. Abbott, F. B. Abdalla, S. Allam, A. Benoit-Lévy, G. M. Bernstein, E. Bertin, D. Brooks, E. Buckley-Geer, D. L. Burke, A. Carnero Rosell, M. Carrasco Kind, J. Carretero, M. Crocce, L. N. da Costa, S. Desai, H. T. Diehl, J. P. Dietrich, P. Doel, T. F. Eifler, A. E. Evrard, D. A. Finley, B. Flaugher, P. Fosalba, J. Frieman, E. Gaztanaga, D. W. Gerdes, D. Gruen, R. A. Gruendl, G. Gutierrez, K. Honscheid, K. Kuehn, N. Kuropatkin, O. Lahav, P. Martini, R. Miquel, B. Nord, R. Ogando, A. A. Plazas, K. Reil, A. Roodman, M. Sako, E. Sanchez, V. Scarpine, M. Schubnell, I. Sevilla-Noarbe, R. C. Smith, M. Soares-Santos, F. Sobreira, E. Suchyta, M. E. C. Swanson, G. Tarle, D. Tucker, V. Vikram, W. Wester, Y. Zhang, J. Zuntz, and DES Collaboration, "Eight Ultra-faint Galaxy Candidates Discovered in Year Two of the Dark Energy Survey," , vol. 813, p. 109, Nov 2015.

[5] H. Jerjen, B. Conn, D. Kim, and M. Schirmer, "On the Nature of Ultra-faint Dwarf Galaxy Candidates. III. Horologium I, Pictor I, Grus I, and Phoenix II," *arXiv e-prints*, p. arXiv:1809.02259, Sep 2018.

[6] A. Drlica-Wagner, K. Bechtol, S. Mau, M. McNanna, E. O. Nadler, A. B. Pace, T. S. Li, A. Pieres, E. Rozo, J. D. Simon, A. R. Walker, R. H. Wechsler, T. M. C. Abbott, S. Allam,

J. Annis, E. Bertin, D. Brooks, D. L. Burke, A. Carnero Rosell, M. Carrasco Kind, J. Carretero, M. Costanzi, L. N. da Costa, J. De Vicente, S. Desai, H. T. Diehl, P. Doel, T. F. Eifler, S. Everett, B. Flaugher, J. Frieman, J. Garcia-Bellido, E. Gaztanaga, D. Gruen, R. A. Gruendl, J. Gschwend, G. Gutierrez, K. Honscheid, D. J. James, E. Krause, K. Kuehn, N. Kuropatkin, O. Lahav, M. A. G. Maia, J. L. Marshall, P. Melchior, F. Menanteau, R. Miquel, A. Palmese, A. A. Plazas, E. Sanchez, V. Scarpine, M. Schubnell, S. Serrano, I. Sevilla-Noarbe, M. Smith, E. Suchyta, and G. Tarle, "Milky Way Satellite Census – I. The Observational Selection Function for Milky Way Satellites in DES Y3 and Pan-STARRS DR1," *arXiv e-prints*, p. arXiv:1912.03302, Dec 2019.

[7] A. Dotter, B. Chaboyer, D. Jevremović, V. Kostov, E. Baron, and J. W. Ferguson, "The Dartmouth Stellar Evolution Database," **??***jnlApJS*, vol. 178, pp. 89–101, Sept. 2008.

[8] A. Dotter, "MESA Isochrones and Stellar Tracks (MIST) 0: Methods for the Construction of Stellar Isochrones," **??***jnlApJS*, vol. 222, p. 8, Jan 2016.

[9] J. D. Simon, A. Drlica-Wagner, T. S. Li, B. Nord, M. Geha, K. Bechtol, E. Balbinot, E. Buckley-Geer, H. Lin, J. Marshall, B. Santiago, L. Strigari, M. Wang, R. H. Wechsler, B. Yanny, T. Abbott, A. H. Bauer, G. M. Bernstein, E. Bertin, D. Brooks, D. L. Burke, D. Capozzi, A. Carnero Rosell, M. Carrasco Kind, C. B. D'Andrea, L. N. da Costa, D. L. DePoy, S. Desai, H. T. Diehl, S. Dodelson, C. E. Cunha, J. Estrada, A. E. Evrard, A. Fausti Neto, E. Fernandez, D. A. Finley, B. Flaugher, J. Frieman, E. Gaztanaga, D. Gerdes, D. Gruen, R. A. Gruendl, K. Honscheid, D. James, S. Kent, K. Kuehn, N. Kuropatkin, O. Lahav, M. A. G. Maia, M. March, P. Martini, C. J. Miller, R. Miquel, R. Ogando, A. K. Romer, A. Roodman, E. S. Rykoff, M. Sako, E. Sanchez, M. Schubnell, I. Sevilla, R. C. Smith, M. Soares-Santos, F. Sobreira, E. Suchyta, M. E. C. Swanson, G. Tarle, J. Thaler, D. Tucker, V. Vikram, A. R. Walker, W. Wester, and DES Collaboration, "Stellar Kinematics and Metallicities in the Ultra-faint Dwarf Galaxy Reticulum II," , vol. 808, p. 95, July 2015.

[10] M. G. Walker, M. Mateo, E. W. Olszewski, S. Koposov, V. Belokurov, P. Jethwa, D. L. Nidever, V. Bonnivard, I. Bailey, John I., E. F. Bell, and S. R. Loebman, "Magellan/M2FS

Spectroscopy of Tucana 2 and Grus 1," , vol. 819, p. 53, Mar 2016.

[11] R. R. Muñoz, P. Côté, F. A. Santana, M. Geha, J. D. Simon, G. A. Oyarzún, P. B. Stetson, and S. G. Djorgovski, "A MegaCam Survey of Outer Halo Satellites. III. Photometric and Structural Parameters," , vol. 860, p. 66, Jun 2018.

[12] A. P. Ji, J. D. Simon, A. Frebel, K. A. Venn, and T. T. Hansen, "Chemical Abundances in the Ultra-faint Dwarf Galaxies Grus I and Triangulum II: Neutron-capture Elements as a Defining Feature of the Faintest Dwarfs," , vol. 870, p. 83, Jan 2019.

[13] C. E. Martínez-Vázquez, A. K. Vivas, M. Gurevich, A. R. Walker, M. McCarthy, A. B. Pace, K. M. Stringer, B. Santiago, R. Hounsell, L. Macri, T. S. Li, K. Bechtol, A. H. Riley, A. G. Kim, J. D. Simon, A. Drlica-Wagner, E. O. Nadler, J. L. Marshall, J. Annis, S. Avila, E. Bertin, D. Brooks, E. Buckley-Geer, D. L. Burke, A. Carnero Rosell, M. Carrasco Kind, L. N. da Costa, J. De Vicente, S. Desai, H. T. Diehl, P. Doel, S. Everett, J. Frieman, J. García-Bellido, E. Gaztanaga, D. Gruen, R. A. Gruendl, J. Gschwend, G. Gutierrez, D. L. Hollowood, K. Honscheid, D. J. James, K. Kuehn, N. Kuropatkin, M. A. G. Maia, F. Menanteau, C. J. Miller, R. Miquel, F. Paz-Chinchón, A. A. Plazas, E. Sanchez, V. Scarpine, S. Serrano, I. Sevilla-Noarbe, M. Smith, M. Soares-Santos, F. Sobreira, M. E. C. Swanson, G. Tarle, V. Vikram, and DES Collaboration, "Search for RR Lyrae stars in DES ultrafaint systems: Grus I, Kim 2, Phoenix II, and Grus II," , vol. 490, pp. 2183–2199, Dec. 2019.

[14] D. G. York, J. Adelman, J. Anderson, John E., S. F. Anderson, J. Annis, N. A. Bahcall, J. A. Bakken, R. Barkhouser, S. Bastian, E. Berman, W. N. Boroski, S. Bracker, C. Briegel, J. W. Briggs, J. Brinkmann, R. Brunner, S. Burles, L. Carey, M. A. Carr, F. J. Castander, B. Chen, P. L. Colestock, A. J. Connolly, J. H. Crocker, I. Csabai, P. C. Czarapata, J. E. Davis, M. Doi, T. Dombeck, D. Eisenstein, N. Ellman, B. R. Elms, M. L. Evans, X. Fan, G. R. Federwitz, L. Fiscelli, S. Friedman, J. A. Frieman, M. Fukugita, B. Gillespie, J. E. Gunn, V. K. Gurbani, E. de Haas, M. Haldeman, F. H. Harris, J. Hayes, T. M. Heckman, G. S. Hennessy, R. B. Hindsley, S. Holm, D. J. Holmgren, C.-h. Huang, C. Hull, D. Husby, S.-I. Ichikawa, T. Ichikawa, Ž. Ivezić, S. Kent, R. S. J. Kim, E. Kinney, M. Klaene, A. N. Kleinman, S. Klein-

man, G. R. Knapp, J. Korienek, R. G. Kron, P. Z. Kunszt, D. Q. Lamb, B. Lee, R. F. Leger, S. Limmongkol, C. Lindenmeyer, D. C. Long, C. Loomis, J. Loveday, R. Lucinio, R. H. Lupton, B. MacKinnon, E. J. Mannery, P. M. Mantsch, B. Margon, P. McGehee, T. A. McKay, A. Meiksin, A. Merelli, D. G. Monet, J. A. Munn, V. K. Narayanan, T. Nash, E. Neilsen, R. Neswold, H. J. Newberg, R. C. Nichol, T. Nicinski, M. Nonino, N. Okada, S. Okamura, J. P. Ostriker, R. Owen, A. G. Pauls, J. Peoples, R. L. Peterson, D. Petravick, J. R. Pier, A. Pope, R. Pordes, A. Prosapio, R. Rechenmacher, T. R. Quinn, G. T. Richards, M. W. Richmond, C. H. Rivetta, C. M. Rockosi, K. Ruthmansdorfer, D. Sand ford, D. J. Schlegel, D. P. Schneider, M. Sekiguchi, G. Sergey, K. Shimasaku, W. A. Siegmund, S. Smee, J. A. Smith, S. Snedden, R. Stone, C. Stoughton, M. A. Strauss, C. Stubbs, M. SubbaRao, A. S. Szalay, I. Szapudi, G. P. Szokoly, A. R. Thakar, C. Tremonti, D. L. Tucker, A. Uomoto, D. Vanden Berk, M. S. Vogeley, P. Waddell, S.-i. Wang, M. Watanabe, D. H. Weinberg, B. Yanny, N. Yasuda, and SDSS Collaboration, "The Sloan Digital Sky Survey: Technical Summary," , vol. 120, pp. 1579–1587, Sep 2000.

[15] The Dark Energy Survey Collaboration, "The Dark Energy Survey," *arXiv e-prints*, pp. astro–ph/0510346, Oct 2005.

[16] K. C. Chambers, E. A. Magnier, N. Metcalfe, H. A. Flewelling, M. E. Huber, C. Z. Waters, L. Denneau, P. W. Draper, D. Farrow, D. P. Finkbeiner, C. Holmberg, J. Koppenhoefer, P. A. Price, A. Rest, R. P. Saglia, E. F. Schlafly, S. J. Smartt, W. Sweeney, R. J. Wainscoat, W. S. Burgett, S. Chastel, T. Grav, J. N. Heasley, K. W. Hodapp, R. Jedicke, N. Kaiser, R. P. Kudritzki, G. A. Luppino, R. H. Lupton, D. G. Monet, J. S. Morgan, P. M. Onaka, B. Shiao, C. W. Stubbs, J. L. Tonry, R. White, E. Bañados, E. F. Bell, R. Bender, E. J. Bernard, M. Boegner, F. Boffi, M. T. Botticella, A. Calamida, S. Casertano, W. P. Chen, X. Chen, S. Cole, N. Deacon, C. Frenk, A. Fitzsimmons, S. Gezari, V. Gibbs, C. Goessl, T. Goggia, R. Gourgue, B. Goldman, P. Grant, E. K. Grebel, N. C. Hambly, G. Hasinger, A. F. Heavens, T. M. Heckman, R. Henderson, T. Henning, M. Holman, U. Hopp, W. H. Ip, S. Isani, M. Jackson, C. D. Keyes, A. M. Koekemoer, R. Kotak, D. Le, D. Liska, K. S. Long,

J. R. Lucey, M. Liu, N. F. Martin, G. Masci, B. McLean, E. Mindel, P. Misra, E. Morganson, D. N. A. Murphy, A. Obaika, G. Narayan, M. A. Nieto-Santisteban, P. Norberg, J. A. Peacock, E. A. Pier, M. Postman, N. Primak, C. Rae, A. Rai, A. Riess, A. Riffeser, H. W. Rix, S. Röser, R. Russel, L. Rutz, E. Schilbach, A. S. B. Schultz, D. Scolnic, L. Strolger, A. Szalay, S. Seitz, E. Small, K. W. Smith, D. R. Soderblom, P. Taylor, R. Thomson, A. N. Taylor, A. R. Thakar, J. Thiel, D. Thilker, D. Unger, Y. Urata, J. Valenti, J. Wagner, T. Walder, F. Walter, S. P. Watters, S. Werner, W. M. Wood-Vasey, and R. Wyse, "The Pan-STARRS1 Surveys," *arXiv e-prints*, p. arXiv:1612.05560, Dec 2016.

[17] D. Homma, M. Chiba, S. Okamoto, Y. Komiyama, M. Tanaka, M. Tanaka, M. N. Ishigaki, M. Akiyama, N. Arimoto, J. A. Garmilla, R. H. Lupton, M. A. Strauss, H. Furusawa, S. Miyazaki, H. Murayama, A. J. Nishizawa, M. Takada, T. Usuda, and S.-Y. Wang, "A New Milky Way Satellite Discovered in the Subaru/Hyper Suprime-Cam Survey," , vol. 832, p. 21, Nov. 2016.

[18] A. Drlica-Wagner, K. Bechtol, S. Allam, D. L. Tucker, R. A. Gruendl, M. D. Johnson, A. R. Walker, D. J. James, D. L. Nidever, K. A. G. Olsen, R. H. Wechsler, M. R. L. Cioni, B. C. Conn, K. Kuehn, T. S. Li, Y. Y. Mao, N. F. Martin, E. Neilsen, N. E. D. Noel, A. Pieres, J. D. Simon, G. S. Stringfellow, R. P. van der Marel, and B. Yanny, "An Ultra-faint Galaxy Candidate Discovered in Early Data from the Magellanic Satellites Survey," , vol. 833, p. L5, Dec 2016.

[19] S. Mau, W. Cerny, A. B. Pace, Y. Choi, A. Drlica-Wagner, L. Santana-Silva, A. H. Riley, D. Erkal, G. S. Stringfellow, M. Adamów, J. L. Carlin, R. A. Gruendl, D. Hernandez-Lang, N. Kuropatkin, T. S. Li, C. E. Martínez-Vázquez, E. Morganson, B. Mutlu-Pakdil, E. H. Neilsen, D. L. Nidever, K. A. G. Olsen, D. J. Sand, E. J. Tollerud, D. L. Tucker, B. Yanny, A. Zenteno, S. Allam, W. A. Barkhouse, K. Bechtol, E. F. Bell, P. Balaji, D. Crnojević, J. Esteves, P. S. Ferguson, C. Gallart, A. K. Hughes, D. J. James, P. Jethwa, L. C. Johnson, K. Kuehn, S. Majewski, Y. Y. Mao, P. Massana, M. McNanna, A. Monachesi, E. O. Nadler, N. E. D. Noël, A. Palmese, F. Paz-Chinchon, A. Pieres, J. Sanchez, N. Shipp, J. D. Simon,

M. Soares-Santos, K. Tavangar, R. P. van der Marel, A. K. Vivas, A. R. Walker, and R. H. Wechsler, "Two Ultra-Faint Milky Way Stellar Systems Discovered in Early Data from the DECam Local Volume Exploration Survey," *arXiv e-prints*, p. arXiv:1912.03301, Dec 2019.

[20] K. Bechtol, A. Drlica-Wagner, E. Balbinot, A. Pieres, J. D. Simon, B. Yanny, B. Santiago, R. H. Wechsler, J. Frieman, A. R. Walker, P. Williams, E. Rozo, E. S. Rykoff, A. Queiroz, E. Luque, A. Benoit-Lévy, D. Tucker, I. Sevilla, R. A. Gruendl, L. N. da Costa, A. Fausti Neto, M. A. G. Maia, T. Abbott, S. Allam, R. Armstrong, A. H. Bauer, G. M. Bernstein, R. A. Bernstein, E. Bertin, D. Brooks, E. Buckley-Geer, D. L. Burke, A. Carnero Rosell, F. J. Castander, R. Covarrubias, C. B. D'Andrea, D. L. DePoy, S. Desai, H. T. Diehl, T. F. Eifler, J. Estrada, A. E. Evrard, E. Fernandez, D. A. Finley, B. Flaugher, E. Gaztanaga, D. Gerdes, L. Girardi, M. Gladders, D. Gruen, G. Gutierrez, J. Hao, K. Honscheid, B. Jain, D. James, S. Kent, R. Kron, K. Kuehn, N. Kuropatkin, O. Lahav, T. S. Li, H. Lin, M. Makler, M. March, J. Marshall, P. Martini, K. W. Merritt, C. Miller, R. Miquel, J. Mohr, E. Neilsen, R. Nichol, B. Nord, R. Ogando, J. Peoples, D. Petravick, A. A. Plazas, A. K. Romer, A. Roodman, M. Sako, E. Sanchez, V. Scarpine, M. Schubnell, R. C. Smith, M. Soares-Santos, F. Sobreira, E. Suchyta, M. E. C. Swanson, G. Tarle, J. Thaler, D. Thomas, W. Wester, J. Zuntz, and DES Collaboration, "Eight New Milky Way Companions Discovered in First-year Dark Energy Survey Data," , vol. 807, p. 50, Jul 2015.

[21] B. Willman and J. Strader, ""Galaxy," Defined," , vol. 144, p. 76, Sep 2012.

[22] J. D. Simon, "The Faintest Dwarf Galaxies," *arXiv e-prints*, p. arXiv:1901.05465, Jan 2019.

[23] N. F. Martin, J. T. A. de Jong, and H.-W. Rix, "A Comprehensive Maximum Likelihood Analysis of the Structural Properties of Faint Milky Way Satellites," , vol. 684, pp. 1075–1092, Sep 2008.

[24] J. S. Bullock and M. Boylan-Kolchin, "Small-Scale Challenges to the ΛCDM Paradigm," , vol. 55, pp. 343–387, Aug. 2017.

[25] D. A. Forbes, N. Bastian, M. Gieles, R. A. Crain, J. M. D. Kruijssen, S. S. Larsen, S. Ploeckinger, O. Agertz, M. Trenti, and A. M. N. Ferguson, "Globular cluster formation

and evolution in the context of cosmological galaxy assembly: open questions," *Proceedings of the Royal Society of London Series A*, vol. 474, p. 20170616, Feb 2018.

[26] L. P. Bassino, J. C. Muzzio, and M. Rabolli, "Are Globular Clusters the Nuclei of Cannibalized Dwarf Galaxies?," , vol. 431, p. 634, Aug 1994.

[27] J. D. Simon and M. Geha, "The Kinematics of the Ultra-faint Milky Way Satellites: Solving the Missing Satellite Problem," , vol. 670, pp. 313–331, Nov 2007.

[28] N. F. Martin, R. A. Ibata, S. C. Chapman, M. Irwin, and G. F. Lewis, "A Keck/DEIMOS spectroscopic survey of faint Galactic satellites: searching for the least massive dwarf galaxies," , vol. 380, pp. 281–300, Sept. 2007.

[29] C. S. Frenk and S. D. M. White, "Dark matter and cosmic structure," *Annalen der Physik*, vol. 524, pp. 507–534, Oct. 2012.

[30] C. Wheeler, J. Oñorbe, J. S. Bullock, M. Boylan-Kolchin, O. D. Elbert, S. Garrison- Kimmel, P. F. Hopkins, and D. Kereš, "Sweating the small stuff: simulating dwarf galaxies, ultra-faint dwarf galaxies, and their own tiny satellites," , vol. 453, pp. 1305–1316, Oct. 2015.

[31] T. Sawala, C. S. Frenk, A. Fattahi, J. F. Navarro, R. G. Bower, R. A. Crain, C. Dalla Vecchia, M. Furlong, A. Jenkins, I. G. McCarthy, Y. Qu, M. Schaller, J. Schaye, and T. Theuns, "Bent by baryons: the low-mass galaxy-halo relation," , vol. 448, pp. 2941–2947, Apr 2015.

[32] A. R. Wetzel, P. F. Hopkins, J.-h. Kim, C.-A. Faucher-Giguère, D. Kereš, and E. Quataert, "Reconciling Dwarf Galaxies with ΛCDM Cosmology: Simulating a Realistic Population of Satellites around a Milky Way-mass Galaxy," , vol. 827, p. L23, Aug 2016.

[33] T. S. Li, J. D. Simon, K. Kuehn, A. B. Pace, D. Erkal, K. Bechtol, B. Yanny, A. Drlica-Wagner, J. L. Marshall, C. Lidman, E. Balbinot, D. Carollo, S. Jenkins, C. E. Martínez-Vázquez, N. Shipp, K. M. Stringer, A. K. Vivas, A. R. Walker, R. H. Wechsler, F. B. Abdalla, S. Allam, J. Annis, S. Avila, E. Bertin, D. Brooks, E. Buckley-Geer, D. L. Burke, A. Carnero Rosell, M. Carrasco Kind, J. Carretero, C. E. Cunha, C. B. D'Andrea, L. N. da Costa, C. Davis, J. De Vicente, P. Doel, T. F. Eifler, A. E. Evrard, B. Flaugher, J. Frieman, J. García-Bellido, E. Gaztanaga, D. W. Gerdes, D. Gruen, R. A. Gruendl, J. Gschwend, G. Gutierrez,

W. G. Hartley, D. L. Hollowood, K. Honscheid, D. J. James, E. Krause, M. A. G. Maia, M. March, F. Menanteau, R. Miquel, A. A. Plazas, E. Sanchez, B. Santiago, V. Scarpine, R. Schindler, M. Schubnell, I. Sevilla-Noarbe, M. Smith, R. C. Smith, M. Soares-Santos, F. Sobreira, E. Suchyta, M. E. C. Swanson, G. Tarle, D. L. Tucker, and DES Collaboration, "The First Tidally Disrupted Ultra-faint Dwarf Galaxy?: A Spectroscopic Analysis of the Tucana III Stream," , vol. 866, p. 22, Oct 2018.

[34] R. R. Muñoz, N. Padmanabhan, and M. Geha, "Measuring Sizes of Ultra-faint Dwarf Galaxies," , vol. 745, p. 127, Feb. 2012.

[35] T. M. Brown, J. Tumlinson, M. Geha, J. D. Simon, L. C. Vargas, D. A. VandenBerg, E. N. Kirby, J. S. Kalirai, R. J. Avila, M. Gennaro, H. C. Ferguson, R. R. Muñoz, P. Guhathakurta, and A. Renzini, "The Quenching of the Ultra-faint Dwarf Galaxies in the Reionization Era," , vol. 796, p. 91, Dec. 2014.

[36] B. C. Conn, H. Jerjen, D. Kim, and M. Schirmer, "On the Nature of Ultra-faint Dwarf Galaxy Candidates. I. DES1, Eridanus III, and Tucana V," , vol. 852, p. 68, Jan 2018.

[37] B. Mutlu-Pakdil, D. J. Sand, J. L. Carlin, K. Spekkens, N. Caldwell, D. Crnojević, A. K. Hughes, B. Willman, and D. Zaritsky, "A Deeper Look at the New Milky Way Satellites: Sagittarius II, Reticulum II, Phoenix II, and Tucana III," , vol. 863, p. 25, Aug 2018.

[38] E. E. Salpeter, "The Luminosity Function and Stellar Evolution.," , vol. 121, p. 161, Jan. 1955.

[39] P. Kroupa, "The Initial Mass Function of Stars: Evidence for Uniformity in Variable Systems," *Science*, vol. 295, pp. 82–91, Jan. 2002.

[40] G. Chabrier, "Galactic Stellar and Substellar Initial Mass Function," , vol. 115, pp. 763–795, Jul 2003.

[41] G. Chabrier, *The Initial Mass Function: From Salpeter 1955 to 2005*, vol. 327, p. 41. 2005.

[42] P. G. van Dokkum and C. Conroy, "A substantial population of low-mass stars in luminous elliptical galaxies," , vol. 468, pp. 940–942, Dec. 2010.

[43] P. G. van Dokkum and C. Conroy, "Confirmation of Enhanced Dwarf-sensitive Absorption

Features in the Spectra of Massive Elliptical Galaxies: Further Evidence for a Non-universal Initial Mass Function," , vol. 735, p. L13, July 2011.

[44] C. Conroy and P. G. van Dokkum, "The Stellar Initial Mass Function in Early-type Galaxies From Absorption Line Spectroscopy. II. Results," , vol. 760, p. 71, Nov. 2012.

[45] M. Geha, T. M. Brown, J. Tumlinson, J. S. Kalirai, J. D. Simon, E. N. Kirby, D. A. VandenBerg, R. R. Muñoz, R. J. Avila, P. Guhathakurta, and H. C. Ferguson, "The Stellar Initial Mass Function of Ultra-faint Dwarf Galaxies: Evidence for IMF Variations with Galactic Environment," , vol. 771, p. 29, July 2013.

[46] A. Albert, B. Anderson, K. Bechtol, A. Drlica-Wagner, M. Meyer, M. Sánchez-Conde, L. Strigari, M. Wood, T. M. C. Abbott, F. B. Abdalla, A. Benoit-Lévy, G. M. Bernstein, R. A. Bernstein, E. Bertin, D. Brooks, D. L. Burke, A. Carnero Rosell, M. Carrasco Kind, J. Carretero, M. Crocce, C. E. Cunha, C. B. D'Andrea, L. N. da Costa, S. Desai, H. T. Diehl, J. P. Dietrich, P. Doel, T. F. Eifler, A. E. Evrard, A. Fausti Neto, D. A. Finley, B. Flaugher, P. Fosalba, J. Frieman, D. W. Gerdes, D. A. Goldstein, D. Gruen, R. A. Gruendl, K. Honscheid, D. J. James, S. Kent, K. Kuehn, N. Kuropatkin, O. Lahav, T. S. Li, M. A. G. Maia, M. March, J. L. Marshall, P. Martini, C. J. Miller, R. Miquel, E. Neilsen, B. Nord, R. Ogando, A. A. Plazas, K. Reil, A. K. Romer, E. S. Rykoff, E. Sanchez, B. Santiago, M. Schubnell, I. Sevilla-Noarbe, R. C. Smith, M. Soares-Santos, F. Sobreira, E. Suchyta, M. E. C. Swanson, G. Tarle, V. Vikram, A. R. Walker, R. H. Wechsler, Fermi-LAT Collaboration, and DES Collaboration, "Searching for Dark Matter Annihilation in Recently Discovered Milky Way Satellites with Fermi-Lat," , vol. 834, p. 110, Jan 2017.

[47] D. J. Sand, J. Strader, B. Willman, D. Zaritsky, B. McLeod, N. Caldwell, A. Seth, and E. Olszewski, "Tidal Signatures in the Faintest Milky Way Satellites: The Detailed Properties of Leo V, Pisces II, and Canes Venatici II," , vol. 756, p. 79, Sep 2012.

[48] D. Crnojević, D. J. Sand, D. Zaritsky, K. Spekkens, B. Willman, and J. R. Hargis, "Deep Imaging of Eridanus II and Its Lone Star Cluster," , vol. 824, p. L14, Jun 2016.

[49] D. Kim, H. Jerjen, M. Geha, A. Chiti, A. P. Milone, G. Da Costa, D. Mackey, A. Frebel, and

B. Conn, "Portrait of a Dark Horse: a Photometric and Spectroscopic Study of the Ultra-faint Milky Way Satellite Pegasus III," , vol. 833, p. 16, Dec 2016.

[50] E. Luque, A. Queiroz, B. Santiago, A. Pieres, E. Balbinot, K. Bechtol, A. Drlica-Wagner, A. F. Neto, L. N. da Costa, M. A. G. Maia, B. Yanny, T. Abbott, S. Allam, A. Benoit-Lévy, E. Bertin, D. Brooks, E. Buckley-Geer, D. L. Burke, A. C. Rosell, M. C. Kind, J. Carretero, C. E. Cunha, S. Desai, H. T. Diehl, J. P. Dietrich, T. F. Eifler, D. A. Finley, B. Flaugher, P. Fosalba, J. Frieman, D. W. Gerdes, D. Gruen, G. Gutierrez, K. Honscheid, D. J. James, K. Kuehn, N. Kuropatkin, O. Lahav, T. S. Li, M. March, J. L. Marshall, P. Martini, R. Miquel, E. Neilsen, R. C. Nichol, B. Nord, R. Ogando, A. A. Plazas, A. K. Romer, A. Roodman, E. Sanchez, V. Scarpine, M. Schubnell, I. Sevilla-Noarbe, R. C. Smith, M. Soares-Santos, F. Sobreira, E. Suchyta, M. E. C. Swanson, G. Tarle, J. Thaler, D. Tucker, A. R. Walker, and Y. Zhang, "Digging deeper into the Southern skies: a compact Milky Way companion discovered in first-year Dark Energy Survey data," , vol. 458, pp. 603–612, May 2016.

[51] J. L. Carlin, D. J. Sand, R. R. Muñoz, K. Spekkens, B. Willman, D. Crnojević, D. A. Forbes, J. Hargis, E. Kirby, A. H. G. Peter, A. J. Romanowsky, and J. Strader, "Deep Subaru Hyper Suprime-Cam Observations of Milky Way Satellites Columba I and Triangulum II," , vol. 154, p. 267, Dec 2017.

[52] B. C. Conn, H. Jerjen, D. Kim, and M. Schirmer, "On the Nature of Ultra-faint Dwarf Galaxy Candidates. II. The Case of Cetus II," , vol. 857, p. 70, Apr 2018.

[53] E. Luque, B. Santiago, A. Pieres, J. L. Marshall, A. B. Pace, R. Kron, A. Drlica-Wagner, A. Queiroz, E. Balbinot, M. dal Ponte, A. Fausti Neto, L. N. da Costa, M. A. G. Maia, A. R. Walker, F. B. Abdalla, S. Allam, J. Annis, K. Bechtol, A. Benoit-Lévy, E. Bertin, D. Brooks, A. Carnero Rosell, M. Carrasco Kind, J. Carretero, M. Crocce, C. Davis, P. Doel, T. F. Eifler, B. Flaugher, J. García-Bellido, D. W. Gerdes, D. Gruen, R. A. Gruendl, G. Gutierrez, K. Honscheid, D. J. James, K. Kuehn, N. Kuropatkin, R. Miquel, R. C. Nichol, A. A. Plazas, E. Sanchez, V. Scarpine, R. Schindler, I. Sevilla-Noarbe, M. Smith, M. Soares-Santos, F. Sobreira, E. Suchyta, G. Tarle, and D. Thomas, "Deep SOAR follow-up photometry of

two Milky Way outer-halo companions discovered with Dark Energy Survey," , vol. 478, pp. 2006–2018, Aug 2018.

[54] B. Mutlu-Pakdil, "A Deeper Look at the New Milky Way Satellites," in *American Astronomical Society Meeting Abstracts #231*, vol. 231 of *American Astronomical Society Meeting Abstracts*, p. 412.03, Jan 2018.

[55] B. McLeod, J. Geary, M. Conroy, D. Fabricant, M. Ordway, A. Szentgyorgyi, S. Amato, M. Ashby, N. Caldwell, D. Curley, T. Gauron, M. Holman, T. Norton, M. Pieri, J. Roll, D. Weaver, J. Zajac, P. Palunas, and D. Osip, "Megacam: A Wide-Field CCD Imager for the MMT and Magellan," , vol. 127, p. 366, Apr 2015.

[56] B. McLeod, J. Geary, M. Ordway, S. Amato, M. Conroy, and T. Gauron, "The MMT Megacam," in *Astrophysics and Space Science Library* (J. E. Beletic, J. W. Beletic, and P. Amico, eds.), vol. 336, p. 337, Mar 2006.

[57] M. F. Skrutskie, R. M. Cutri, R. Stiening, M. D. Weinberg, S. Schneider, J. M. Carpenter, C. Beichman, R. Capps, T. Chester, and J. Elias, "The Two Micron All Sky Survey (2MASS)," , vol. 131, pp. 1163–1183, Feb 2006.

[58] E. Bertin, "SWarp: Resampling and Co-adding FITS Images Together," Oct 2010.

[59] P. B. Stetson, "DAOPHOT: A Computer Program for Crowded-Field Stellar Photometry," , vol. 99, p. 191, Mar 1987.

[60] B. Flaugher, H. T. Diehl, K. Honscheid, T. M. C. Abbott, O. Alvarez, R. Angstadt, J. T. Annis, M. Antonik, O. Ballester, L. Beaufore, G. M. Bernstein, R. A. Bernstein, B. Bigelow, M. Bonati, D. Boprie, D. Brooks, E. J. Buckley-Geer, J. Campa, L. Cardiel-Sas, F. J. Castander, J. Castilla, H. Cease, J. M. Cela-Ruiz, S. Chappa, E. Chi, C. Cooper, L. N. da Costa, E. Dede, G. Derylo, D. L. DePoy, J. de Vicente, P. Doel, A. Drlica-Wagner, J. Eiting, A. E. Elliott, J. Emes, J. Estrada, A. Fausti Neto, D. A. Finley, R. Flores, J. Frieman, D. Gerdes, M. D. Gladders, B. Gregory, G. R. Gutierrez, J. Hao, S. E. Holland, S. Holm, D. Huffman, C. Jackson, D. J. James, M. Jonas, A. Karcher, I. Karliner, S. Kent, R. Kessler, M. Kozlovsky, R. G. Kron, D. Kubik, K. Kuehn, S. Kuhlmann, K. Kuk, O. Lahav, A. Lathrop, J. Lee, M. E. Levi,

P. Lewis, T. S. Li, I. Mandrichenko, J. L. Marshall, G. Martinez, K. W. Merritt, R. Miquel, F. Muñoz, E. H. Neilsen, R. C. Nichol, B. Nord, R. Ogando, J. Olsen, N. Palaio, K. Patton, J. Peoples, A. A. Plazas, J. Rauch, K. Reil, J. P. Rheault, N. A. Roe, H. Rogers, A. Roodman, E. Sanchez, V. Scarpine, R. H. Schindler, R. Schmidt, R. Schmitt, M. Schubnell, K. Schultz, P. Schurter, L. Scott, S. Serrano, T. M. Shaw, R. C. Smith, M. Soares-Santos, A. Stefanik, W. Stuermer, E. Suchyta, A. Sypniewski, G. Tarle, J. Thaler, R. Tighe, C. Tran, D. Tucker, A. R. Walker, G. Wang, M. Watson, C. Weaverdyck, W. Wester, R. Woods, B. Yanny, and DES Collaboration, "The Dark Energy Camera," , vol. 150, p. 150, Nov. 2015.

[61] E. Morganson, R. A. Gruendl, F. Menanteau, M. Carrasco Kind, Y. C. Chen, G. Daues, A. Drlica-Wagner, D. N. Friedel, M. Gower, M. W. G. Johnson, M. D. Johnson, R. Kessler, F. Paz-Chinchón, D. Petravick, C. Pond, B. Yanny, S. Allam, R. Armstrong, W. Barkhouse, K. Bechtol, A. Benoit-Lévy, G. M. Bernstein, E. Bertin, E. Buckley-Geer, R. Covarrubias, S. Desai, H. T. Diehl, D. A. Goldstein, D. Gruen, T. S. Li, H. Lin, J. Marriner, J. J. Mohr, E. Neilsen, C. C. Ngeow, K. Paech, E. S. Rykoff, M. Sako, I. Sevilla-Noarbe, E. Sheldon, F. Sobreira, D. L. Tucker, W. Wester, and DES Collaboration, "The Dark Energy Survey Image Processing Pipeline," , vol. 130, p. 074501, July 2018.

[62] T. M. C. Abbott, F. B. Abdalla, A. Alarcon, J. Aleksić, S. Allam, S. Allen, A. Amara, J. Annis, J. Asorey, S. Avila, D. Bacon, E. Balbinot, M. Banerji, N. Banik, W. Barkhouse, M. Baumer, E. Baxter, K. Bechtol, M. R. Becker, A. Benoit-Lévy, B. A. Benson, G. M. Bernstein, E. Bertin, J. Blazek, S. L. Bridle, D. Brooks, D. Brout, E. Buckley-Geer, D. L. Burke, M. T. Busha, A. Campos, D. Capozzi, A. Carnero Rosell, M. Carrasco Kind, J. Carretero, F. J. Castander, R. Cawthon, C. Chang, N. Chen, M. Childress, A. Choi, C. Conselice, R. Crittenden, M. Crocce, C. E. Cunha, C. B. D'Andrea, L. N. da Costa, R. Das, T. M. Davis, C. Davis, J. De Vicente, D. L. DePoy, J. DeRose, S. Desai, H. T. Diehl, J. P. Dietrich, S. Dodelson, P. Doel, A. Drlica-Wagner, T. F. Eifler, A. E. Elliott, F. Elsner, J. Elvin-Poole, J. Estrada, A. E. Evrard, Y. Fang, E. Fernandez, A. Ferté, D. A. Finley, B. Flaugher, P. Fosalba, O. Friedrich, J. Frieman, J. García-Bellido, M. Garcia-Fernandez, M. Gatti, E. Gaztanaga, D. W. Gerdes,

T. Giannantonio, M. S. S. Gill, K. Glazebrook, D. A. Goldstein, D. Gruen, R. A. Gruendl, J. Gschwend, G. Gutierrez, S. Hamilton, W. G. Hartley, S. R. Hinton, K. Honscheid, B. Hoyle, D. Huterer, B. Jain, D. J. James, M. Jarvis, T. Jeltema, M. D. Johnson, M. W. G. Johnson, T. Kacprzak, S. Kent, A. G. Kim, A. King, D. Kirk, N. Kokron, A. Kovacs, E. Krause, C. Krawiec, A. Kremin, K. Kuehn, S. Kuhlmann, N. Kuropatkin, F. Lacasa, O. Lahav, T. S. Li, A. R. Liddle, C. Lidman, M. Lima, H. Lin, N. MacCrann, M. A. G. Maia, M. Makler, M. Manera, M. March, J. L. Marshall, P. Martini, R. G. McMahon, P. Melchior, F. Menanteau, R. Miquel, V. Miranda, D. Mudd, J. Muir, A. Möller, E. Neilsen, R. C. Nichol, B. Nord, P. Nugent, R. L. C. Ogando, A. Palmese, J. Peacock, H. V. Peiris, J. Peoples, W. J. Percival, D. Petravick, A. A. Plazas, A. Porredon, J. Prat, A. Pujol, M. M. Rau, A. Refregier, P. M. Ricker, N. Roe, R. P. Rollins, A. K. Romer, A. Roodman, R. Rosenfeld, A. J. Ross, E. Rozo, E. S. Rykoff, M. Sako, A. I. Salvador, S. Samuroff, C. Sánchez, E. Sanchez, B. Santiago, V. Scarpine, R. Schindler, D. Scolnic, L. F. Secco, S. Serrano, I. Sevilla-Noarbe, E. Sheldon, R. C. Smith, M. Smith, J. Smith, M. Soares-Santos, F. Sobreira, E. Suchyta, G. Tarle, D. Thomas, M. A. Troxel, D. L. Tucker, B. E. Tucker, S. A. Uddin, T. N. Varga, P. Vielzeuf, V. Vikram, A. K. Vivas, A. R. Walker, M. Wang, R. H. Wechsler, J. Weller, W. Wester, R. C. Wolf, B. Yanny, F. Yuan, A. Zenteno, B. Zhang, Y. Zhang, J. Zuntz, and Dark Energy Survey Collaboration, "Dark Energy Survey year 1 results: Cosmological constraints from galaxy clustering and weak lensing," , vol. 98, p. 043526, Aug. 2018.

[63] N. Shipp, A. Drlica-Wagner, E. Balbinot, P. Ferguson, D. Erkal, T. S. Li, K. Bechtol, V. Belokurov, B. Buncher, and D. Carollo, "Stellar Streams Discovered in the Dark Energy Survey," , vol. 862, p. 114, Aug 2018.

[64] H. C. Plummer, "On the problem of distribution in globular star clusters," , vol. 71, pp. 460–470, Mar 1911.

[65] A. Bressan, P. Marigo, L. Girardi, B. Salasnich, C. Dal Cero, S. Rubele, and A. Nanni, "PARSEC: stellar tracks and isochrones with the PAdova and TRieste Stellar Evolution Code," , vol. 427, pp. 127–145, Nov 2012.

[66] A. Drlica-Wagner, K. Bechtol, S. Mau, M. McNanna, E. O. Nadler, A. B. Pace, T. S. Li, A. Pieres, E. Rozo, J. D. Simon, A. R. Walker, R. H. Wechsler, T. M. C. Abbott, S. Allam, J. Annis, E. Bertin, D. Brooks, D. L. Burke, A. C. Rosell, M. Carrasco Kind, J. Carretero, M. Costanzi, L. N. da Costa, J. De Vicente, S. Desai, H. T. Diehl, P. Doel, T. F. Eifler, S. Everett, B. Flaugher, J. Frieman, J. García-Bellido, E. Gaztanaga, D. Gruen, R. A. Gruendl, J. Gschwend, G. Gutierrez, K. Honscheid, D. J. James, E. Krause, K. Kuehn, N. Kuropatkin, O. Lahav, M. A. G. Maia, J. L. Marshall, P. Melchior, F. Menanteau, R. Miquel, A. Palmese, A. A. Plazas, E. Sanchez, V. Scarpine, M. Schubnell, S. Serrano, I. Sevilla-Noarbe, M. Smith, E. Suchyta, G. Tarle, and DES Collaboration, "Milky Way Satellite Census. I. The Observational Selection Function for Milky Way Satellites in DES Y3 and Pan-STARRS DR1," , vol. 893, p. 47, Apr. 2020.

[67] D. Foreman-Mackey, D. W. Hogg, D. Lang, and J. Goodman, "emcee: The MCMC Hammer," , vol. 125, p. 306, Mar 2013.

[68] J. D. Simon, "The Faintest Dwarf Galaxies," , vol. 57, pp. 375–415, Aug 2019.

[69] N. Caldwell, M. G. Walker, M. Mateo, E. W. Olszewski, S. Koposov, V. Belokurov, G. Torrealba, A. Geringer-Sameth, and C. I. Johnson, "Crater 2: An Extremely Cold Dark Matter Halo," , vol. 839, p. 20, Apr. 2017.

[70] M. Gennaro, M. Geha, K. Tchernyshyov, T. M. Brown, R. J. Avila, C. Conroy, R. R. Muñoz, J. D. Simon, and J. Tumlinson, "The Initial Mass Function in the Coma Berenices Dwarf Galaxy from Deep Near-infrared HST Observations," , vol. 863, p. 38, Aug. 2018.

[71] C. J. Grillmair, J. R. Mould, J. A. Holtzman, G. Worthey, G. E. Ballester, C. J. Burrows, J. T. Clarke, D. Crisp, R. W. Evans, I. Gallagher, John S., R. E. Griffiths, J. J. Hester, J. G. Hoessel, P. A. Scowen, K. R. Stapelfeldt, J. T. Trauger, A. M. Watson, and J. A. Westphal, "Hubble Space Telescope Observations of the Draco Dwarf Spheroidal Galaxy," , vol. 115, pp. 144–151, Jan. 1998.

[72] R. F. G. Wyse, G. Gilmore, M. L. Houdashelt, S. Feltzing, L. Hebb, I. Gallagher, John S., and T. A. Smecker-Hane, "Faint stars in the Ursa Minor dwarf spheroidal galaxy: implications for

the low-mass stellar initial mass function at high redshift," , vol. 7, pp. 395–433, Oct. 2002.

[73] J. S. Kalirai, J. Anderson, A. Dotter, H. B. Richer, G. G. Fahlman, B. M. S. Hansen, J. Hurley, I. N. Reid, R. M. Rich, and M. M. Shara, "Ultra-Deep Hubble Space Telescope Imaging of the Small Magellanic Cloud: The Initial Mass Function of Stars with M <~1 M $_{\odot}$," , vol. 763, p. 110, Feb. 2013.

[74] T. M. C. Abbott, M. Adamow, M. Aguena, S. Allam, A. Amon, S. Avila, D. Bacon, M. Banerji, K. Bechtol, M. R. Becker, G. M. Bernstein, E. Bertin, S. Bhargava, S. L. Bridle, D. Brooks, D. L. Burke, A. Carnero Rosell, M. Carrasco Kind, J. Carretero, F. J. Castander, R. Cawthon, C. Chang, A. Choi, C. Conselice, M. Costanzi, M. Crocce, L. N. da Costa, T. M. Davis, J. De Vicente, J. DeRose, S. Desai, H. T. Diehl, J. P. Dietrich, A. Drlica-Wagner, K. Eckert, J. Elvin-Poole, S. Everett, A. E. Evrard, I. Ferrero, A. Ferté, B. Flaugher, P. Fosalba, D. Friedel, J. Frieman, J. García-Bellido, L. Gelman, D. W. Gerdes, T. Giannantonio, M. Gill, D. Gruen, R. A. Gruendl, J. Gschwend, G. Gutierrez, W. G. Hartley, S. R. Hinton, D. L. Hollowood, D. Huterer, D. J. James, T. Jeltema, M. D. Johnson, S. Kent, R. Kron, K. Kuehn, N. Kuropatkin, O. Lahav, T. S. Li, C. Lidman, H. Lin, N. MacCrann, M. A. G. Maia, T. Manning, M. March, J. L. Marshall, P. Martini, P. Melchior, F. Menanteau, R. Miquel, R. Morgan, J. Myles, E. Neilsen, R. L. C. Ogando, A. Palmese, F. Paz-Chinchón, D. Petravick, A. Pieres, A. A. Plazas, C. Pond, M. Rodriguez-Monroy, A. K. Romer, A. Roodman, E. S. Rykoff, M. Sako, E. Sanchez, B. Santiago, S. Serrano, I. Sevilla-Noarbe, J. Allyn. Smith, M. Smith, M. Soares-Santos, E. Suchyta, M. E. C. Swanson, G. Tarle, D. Thomas, C. To, P. E. Tremblay, M. A. Troxel, D. L. Tucker, D. J. Turner, T. N. Varga, A. R. Walker, R. H. Wechsler, J. Weller, W. Wester, R. D. Wilkinson, B. Yanny, Y. Zhang, R. Nikutta, M. Fitzpatrick, A. Jacques, A. Scott, K. Olsen, L. Huang, D. Herrera, S. Juneau, D. Nidever, B. A. Weaver, C. Adean, V. Correia, M. de Freitas, F. N. Freitas, C. Singulani, and G. Vila-Verde, "The Dark Energy Survey Data Release 2," *arXiv e-prints*, p. arXiv:2101.05765, Jan. 2021.

[75] E. Bertin, "Automated Morphometry with SExtractor and PSFEx," in *Astronomical Data*

Analysis Software and Systems XX (I. N. Evans, A. Accomazzi, D. J. Mink, and A. H. Rots, eds.), vol. 442 of *Astronomical Society of the Pacific Conference Series*, p. 435, July 2011.

[76] E. Bertin and S. Arnouts, "SExtractor: Software for source extraction.," , vol. 117, pp. 393–404, June 1996.

[77] D. Homma, M. Chiba, S. Okamoto, Y. Komiyama, M. Tanaka, M. Tanaka, M. N. Ishigaki, K. Hayashi, N. Arimoto, J. A. Garmilla, R. H. Lupton, M. A. Strauss, S. Miyazaki, S.-Y. Wang, and H. Murayama, "Searches for new Milky Way satellites from the first two years of data of the Subaru/Hyper Suprime-Cam survey: Discovery of Cetus III," , vol. 70, p. S18, Jan. 2018.

[78] J. L. Carlin, D. J. Sand, R. R. Muñoz, K. Spekkens, B. Willman, D. Crnojević, D. A. Forbes, J. Hargis, E. Kirby, A. H. G. Peter, A. J. Romanowsky, and J. Strader, "Deep Subaru Hyper Suprime-Cam Observations of Milky Way Satellites Columba I and Triangulum II," , vol. 154, p. 267, Dec. 2017.

[79] E. Luque, A. Pieres, B. Santiago, B. Yanny, A. K. Vivas, A. Queiroz, A. Drlica-Wagner, E. Morganson, E. Balbinot, J. L. Marshall, T. S. Li, A. F. Neto, L. N. da Costa, M. A. G. Maia, K. Bechtol, A. G. Kim, G. M. Bernstein, S. Dodelson, L. Whiteway, H. T. Diehl, D. A. Finley, T. Abbott, F. B. Abdalla, S. Allam, J. Annis, A. Benoit-Lévy, E. Bertin, D. Brooks, D. L. Burke, A. C. Rosell, M. C. Kind, J. Carretero, C. E. Cunha, C. B. D'Andrea, S. Desai, P. Doel, A. E. Evrard, B. Flaugher, P. Fosalba, D. W. Gerdes, D. A. Goldstein, D. Gruen, R. A. Gruendl, G. Gutierrez, D. J. James, K. Kuehn, N. Kuropatkin, O. Lahav, P. Martini, R. Miquel, B. Nord, R. Ogando, A. A. Plazas, A. K. Romer, E. Sanchez, V. Scarpine, M. Schubnell, I. Sevilla-Noarbe, R. C. Smith, M. Soares-Santos, F. Sobreira, E. Suchyta, M. E. C. Swanson, G. Tarle, D. Thomas, and A. R. Walker, "The Dark Energy Survey view of the Sagittarius stream: discovery of two faint stellar system candidates," , vol. 468, pp. 97–108, June 2017.

[80] B. C. Conn, H. Jerjen, D. Kim, and M. Schirmer, "On the Nature of Ultra-faint Dwarf Galaxy Candidates. I. DES1, Eridanus III, and Tucana V," , vol. 852, p. 68, Jan. 2018.

[81] D. Kim and H. Jerjen, "Horologium II: A Second Ultra-faint Milky Way Satellite in the

Horologium Constellation," , vol. 808, p. L39, Aug 2015.

[82] H. Aihara, R. Armstrong, S. Bickerton, J. Bosch, J. Coupon, H. Furusawa, Y. Hayashi, H. Ikeda, Y. Kamata, H. Karoji, S. Kawanomoto, M. Koike, Y. Komiyama, D. Lang, R. H. Lupton, S. Mineo, H. Miyatake, S. Miyazaki, T. Morokuma, Y. Obuchi, Y. Oishi, Y. Okura, P. A. Price, T. Takata, M. M. Tanaka, M. Tanaka, Y. Tanaka, T. Uchida, F. Uraguchi, Y. Utsumi, S.-Y. Wang, Y. Yamada, H. Yamanoi, N. Yasuda, N. Arimoto, M. Chiba, F. Finet, H. Fujimori, S. Fujimoto, J. Furusawa, T. Goto, A. Goulding, J. E. Gunn, Y. Harikane, T. Hattori, M. Hayashi, K. G. Hełminiak, R. Higuchi, C. Hikage, P. T. P. Ho, B.-C. Hsieh, K. Huang, S. Huang, M. Imanishi, I. Iwata, A. T. Jaelani, H.-Y. Jian, N. Kashikawa, N. Katayama, T. Kojima, A. Konno, S. Koshida, H. Kusakabe, A. Leauthaud, C.-H. Lee, L. Lin, Y.-T. Lin, R. Mandelbaum, Y. Matsuoka, E. Medezinski, S. Miyama, R. Momose, A. More, S. More, S. Mukae, R. Murata, H. Murayama, T. Nagao, F. Nakata, M. Niida, H. Niikura, A. J. Nishizawa, M. Oguri, N. Okabe, Y. Ono, M. Onodera, M. Onoue, M. Ouchi, T.-S. Pyo, T. Shibuya, K. Shimasaku, M. Simet, J. Speagle, D. N. Spergel, M. A. Strauss, Y. Sugahara, N. Sugiyama, Y. Suto, N. Suzuki, P. J. Tait, M. Takada, T. Terai, Y. Toba, E. L. Turner, H. Uchiyama, K. Umetsu, Y. Urata, T. Usuda, S. Yeh, and S. Yuma, "First data release of the Hyper Suprime-Cam Subaru Strategic Program," , vol. 70, p. S8, Jan. 2018.

[83] H. Aihara, N. Arimoto, R. Armstrong, S. Arnouts, N. A. Bahcall, S. Bickerton, J. Bosch, K. Bundy, P. L. Capak, J. H. H. Chan, M. Chiba, J. Coupon, E. Egami, M. Enoki, F. Finet, H. Fujimori, S. Fujimoto, H. Furusawa, J. Furusawa, T. Goto, A. Goulding, J. P. Greco, J. E. Greene, J. E. Gunn, T. Hamana, Y. Harikane, Y. Hashimoto, T. Hattori, M. Hayashi, Y. Hayashi, K. G. Hełminiak, R. Higuchi, C. Hikage, P. T. P. Ho, B.-C. Hsieh, K. Huang, S. Huang, H. Ikeda, M. Imanishi, A. K. Inoue, K. Iwasawa, I. Iwata, A. T. Jaelani, H.-Y. Jian, Y. Kamata, H. Karoji, N. Kashikawa, N. Katayama, S. Kawanomoto, I. Kayo, J. Koda, M. Koike, T. Kojima, Y. Komiyama, A. Konno, S. Koshida, Y. Koyama, H. Kusakabe, A. Leauthaud, C.-H. Lee, L. Lin, Y.-T. Lin, R. H. Lupton, R. Mandelbaum, Y. Matsuoka, E. Medezinski, S. Mineo, S. Miyama, H. Miyatake, S. Miyazaki, R. Momose, A. More,

S. More, Y. Moritani, T. J. Moriya, T. Morokuma, S. Mukae, R. Murata, H. Murayama, T. Nagao, F. Nakata, M. Niida, H. Niikura, A. J. Nishizawa, Y. Obuchi, M. Oguri, Y. Oishi, N. Okabe, S. Okamoto, Y. Okura, Y. Ono, M. Onodera, M. Onoue, K. Osato, M. Ouchi, P. A. Price, T.-S. Pyo, M. Sako, M. Sawicki, T. Shibuya, K. Shimasaku, A. Shimono, M. Shirasaki, J. D. Silverman, M. Simet, J. Speagle, D. N. Spergel, M. A. Strauss, Y. Sugahara, N. Sugiyama, Y. Suto, S. H. Suyu, N. Suzuki, P. J. Tait, M. Takada, T. Takata, N. Tamura, M. M. Tanaka, M. Tanaka, M. Tanaka, Y. Tanaka, T. Terai, Y. Terashima, Y. Toba, N. Tominaga, J. Toshikawa, E. L. Turner, T. Uchida, H. Uchiyama, K. Umetsu, F. Uraguchi, Y. Urata, T. Usuda, Y. Utsumi, S.-Y. Wang, W.-H. Wang, K. C. Wong, K. Yabe, Y. Yamada, H. Yamanoi, N. Yasuda, S. Yeh, A. Yonehara, and S. Yuma, "The Hyper Suprime-Cam SSP Survey: Overview and survey design," , vol. 70, p. S4, Jan. 2018.

[84] T. K. Fritz, R. Carrera, G. Battaglia, and S. Taibi, "Gaia DR 2 and VLT/FLAMES search for new satellites of the LMC," , vol. 623, p. A129, Mar. 2019.

[85] A. Drlica-Wagner, K. Bechtol, S. Allam, D. L. Tucker, R. A. Gruendl, M. D. Johnson, A. R. Walker, D. J. James, D. L. Nidever, K. A. G. Olsen, R. H. Wechsler, M. R. L. Cioni, B. C. Conn, K. Kuehn, T. S. Li, Y. Y. Mao, N. F. Martin, E. Neilsen, N. E. D. Noel, A. Pieres, J. D. Simon, G. S. Stringfellow, R. P. van der Marel, and B. Yanny, "An Ultra-faint Galaxy Candidate Discovered in Early Data from the Magellanic Satellites Survey," , vol. 833, p. L5, Dec. 2016.

[86] A. Chiti, A. Frebel, J. D. Simon, D. Erkal, L. J. Chang, L. Necib, A. P. Ji, H. Jerjen, D. Kim, and J. E. Norris, "An extended halo around an ancient dwarf galaxy," *Nature Astronomy*, Feb. 2021.

APPENDIX A

HESS CMDS

Text for the Appendix follows.

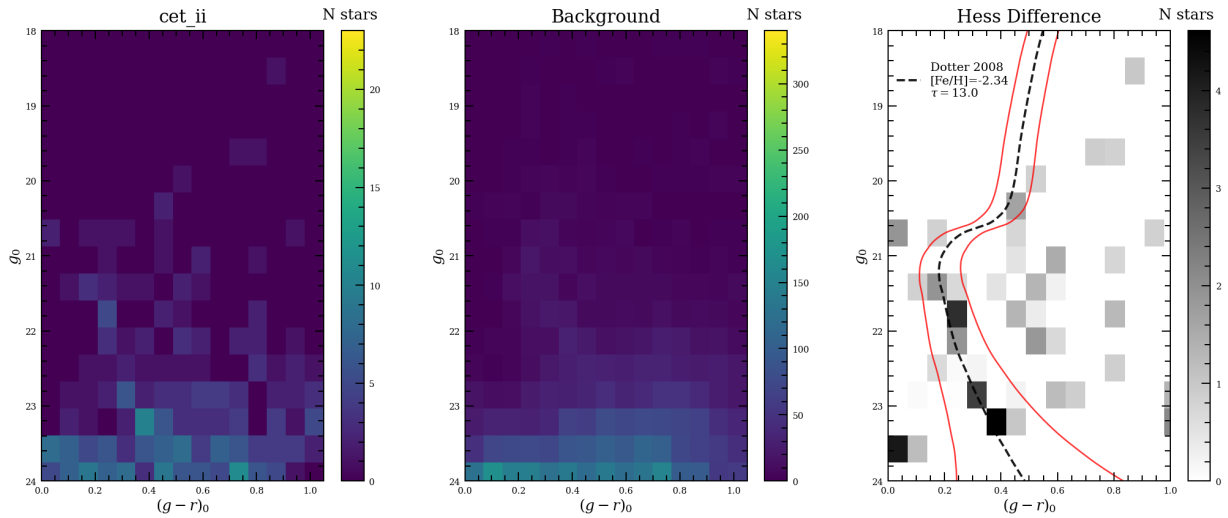

Figure A.1: The left panel is a binned CMD of Cetus II within a ROI of $2r_h$. The middle panel is a binned CMD of the background nearby. The right panel is a background subtracted Hess color magnitude diagram. The dashed line represents an old, metal poor Dotter 2008 isochrone and the red lines are DES Y6_GOLD representative spread due to photometric uncertainty.

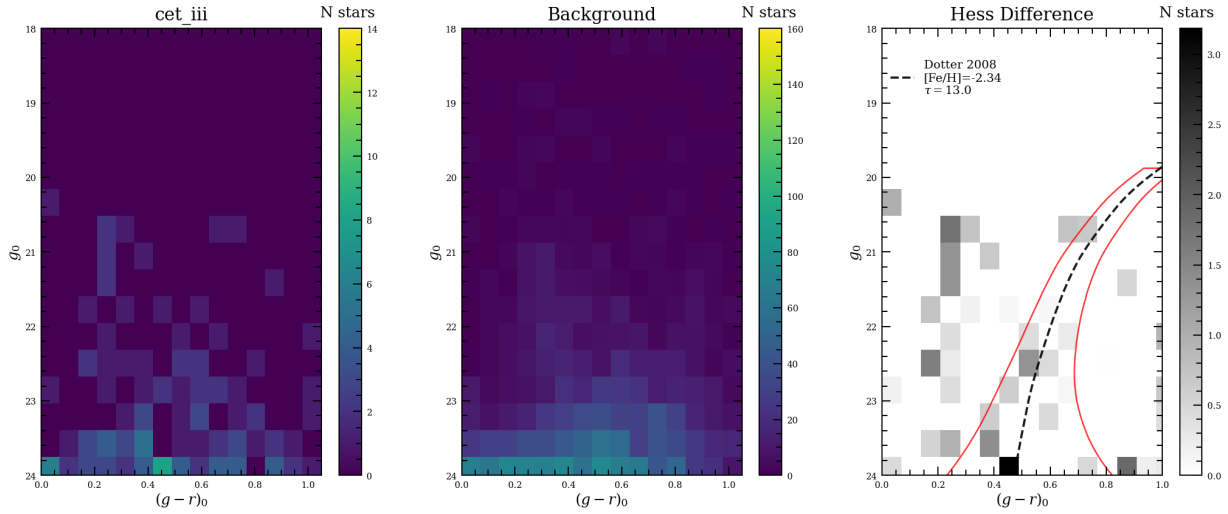

Figure A.2: A background subtracted Hess color magnitude diagram of Cetus III. This figure is similar to Figure A.1

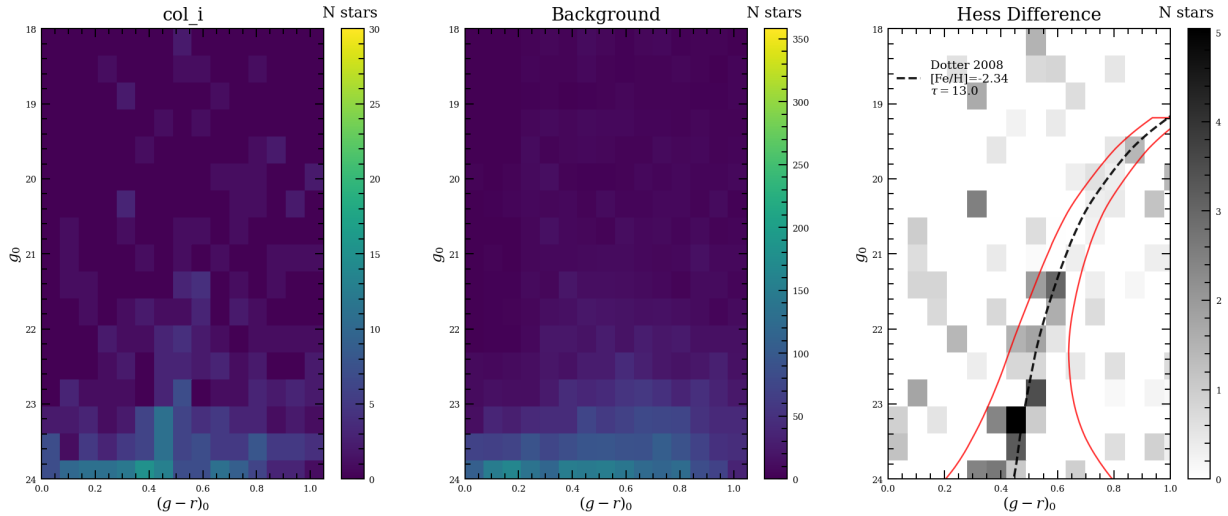

Figure A.3: A background subtracted Hess color magnitude diagram of Columba I. This figure is similar to Figure A.1

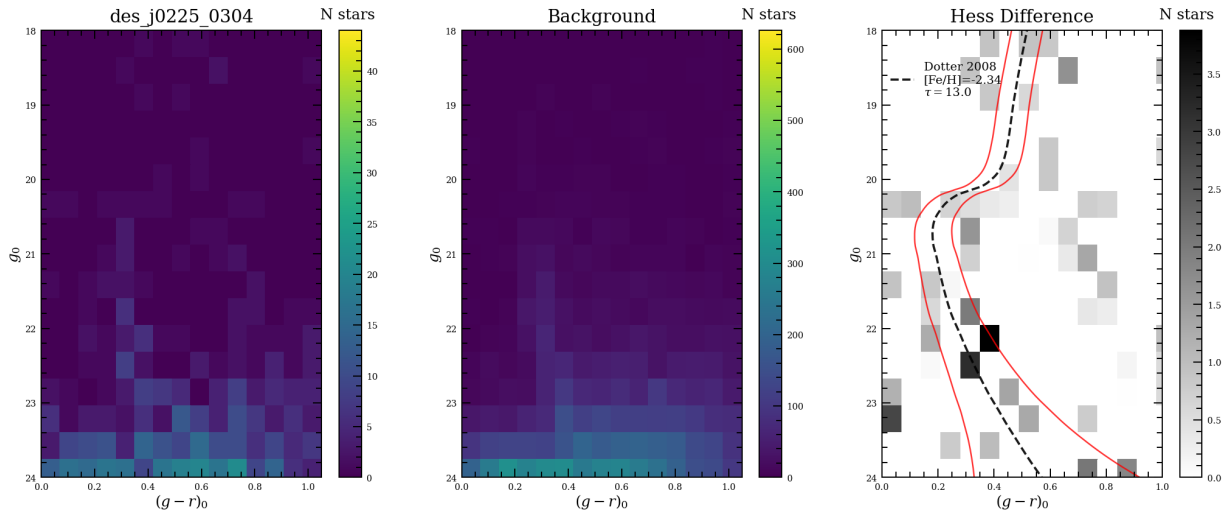

Figure A.4: A background subtracted Hess color magnitude diagram of DES 0225 0304. A background subtracted Hess color magnitude diagram of Columba I. This figure is similar to Figure A.1

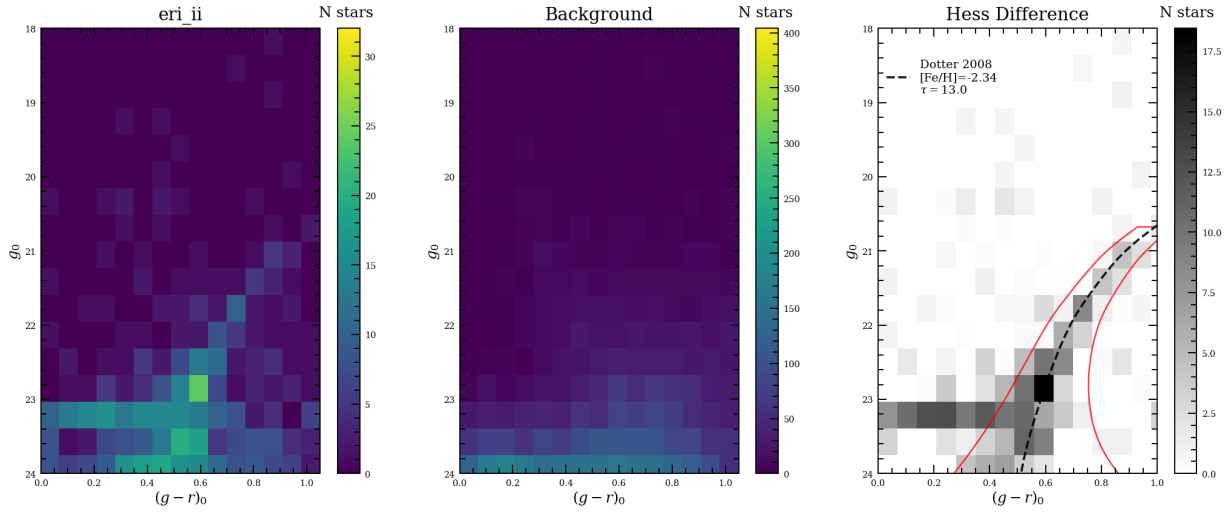

Figure A.5: A background subtracted Hess color magnitude diagram of Eridanus II. This figure is similar to Figure A.1

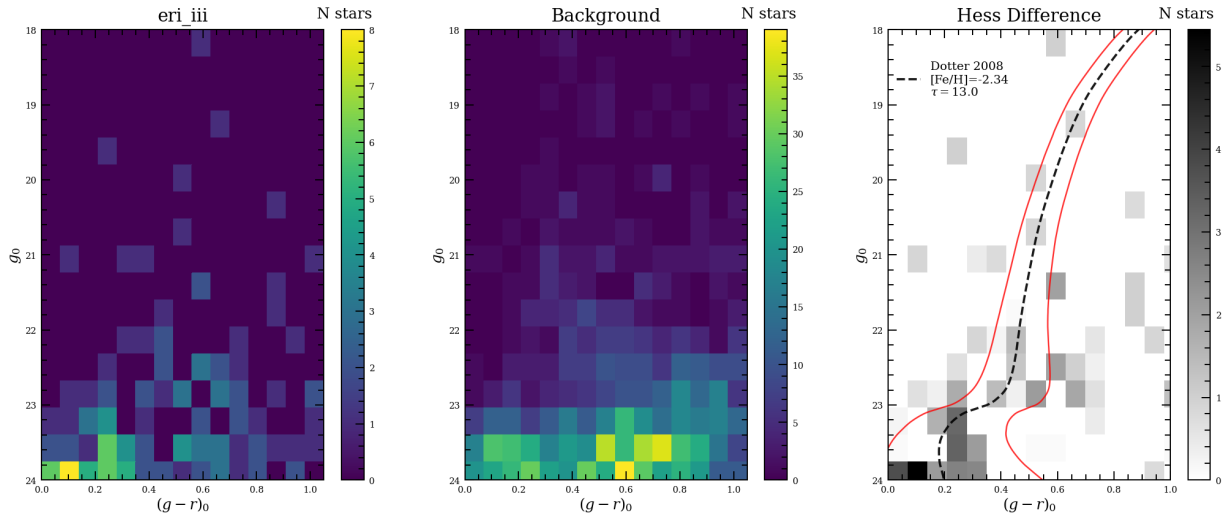

Figure A.6: A background subtracted Hess color magnitude diagram of Eridanus III. This figure is similar to Figure A.1

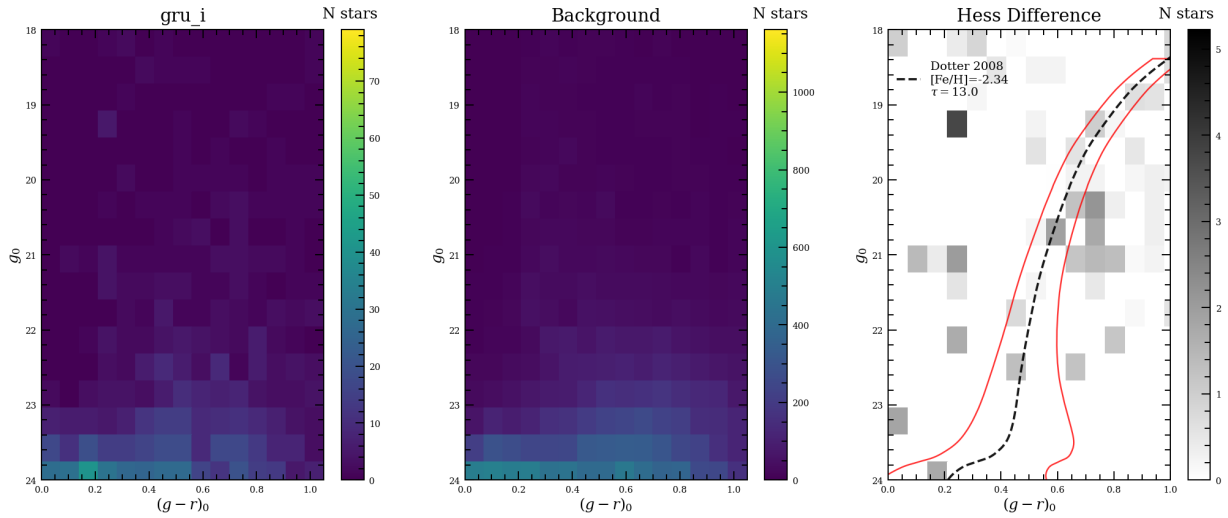

Figure A.7: A background subtracted Hess color magnitude diagram of Grus I. This figure is similar to Figure A.1

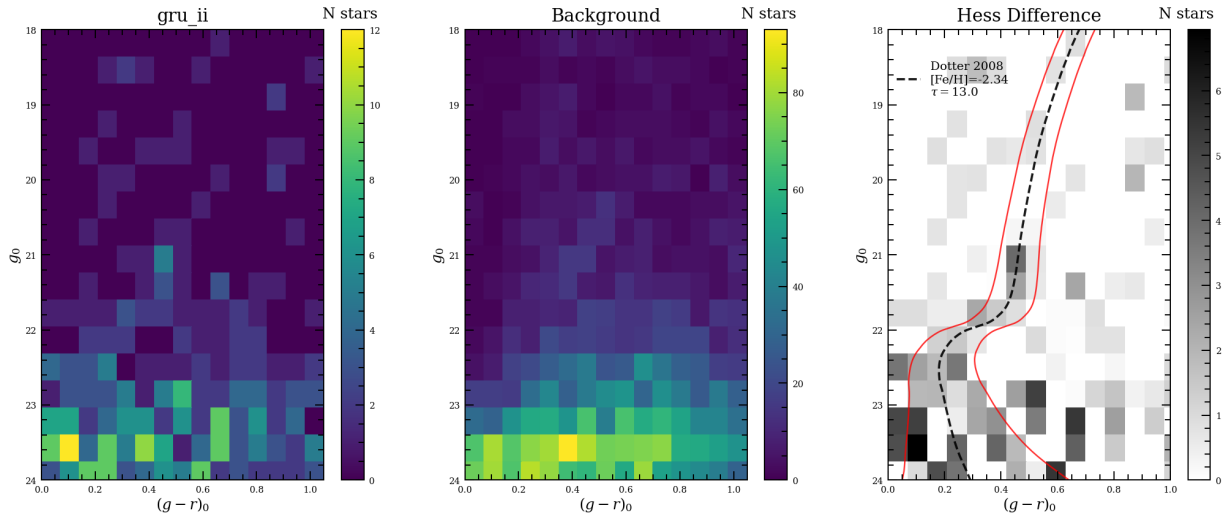

Figure A.8: A background subtracted Hess color magnitude diagram of Grus II. This figure is similar to Figure A.1

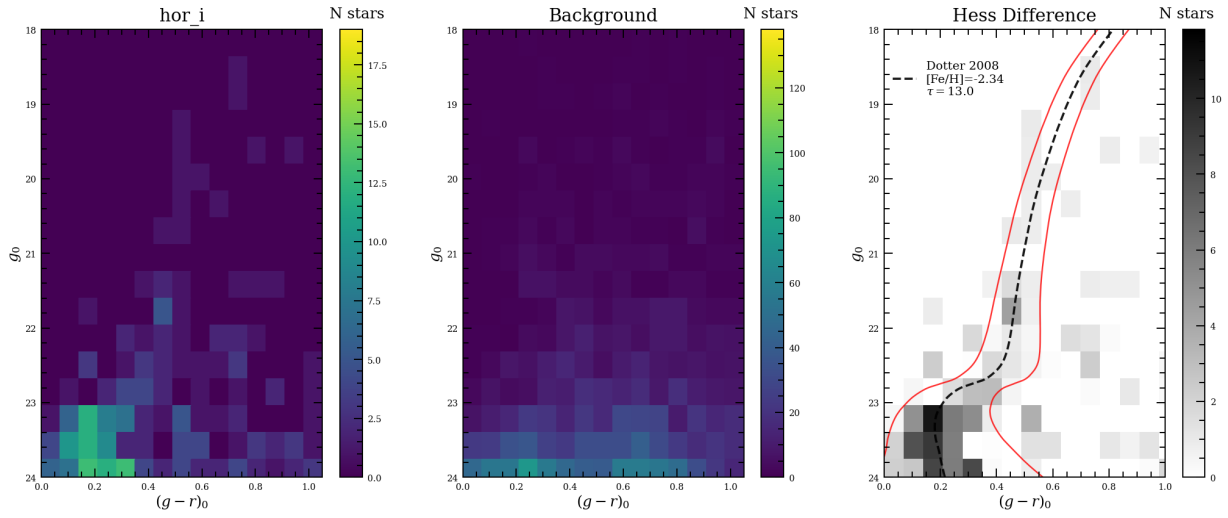

Figure A.9: A background subtracted Hess color magnitude diagram of Horologium I. This figure is similar to Figure A.1

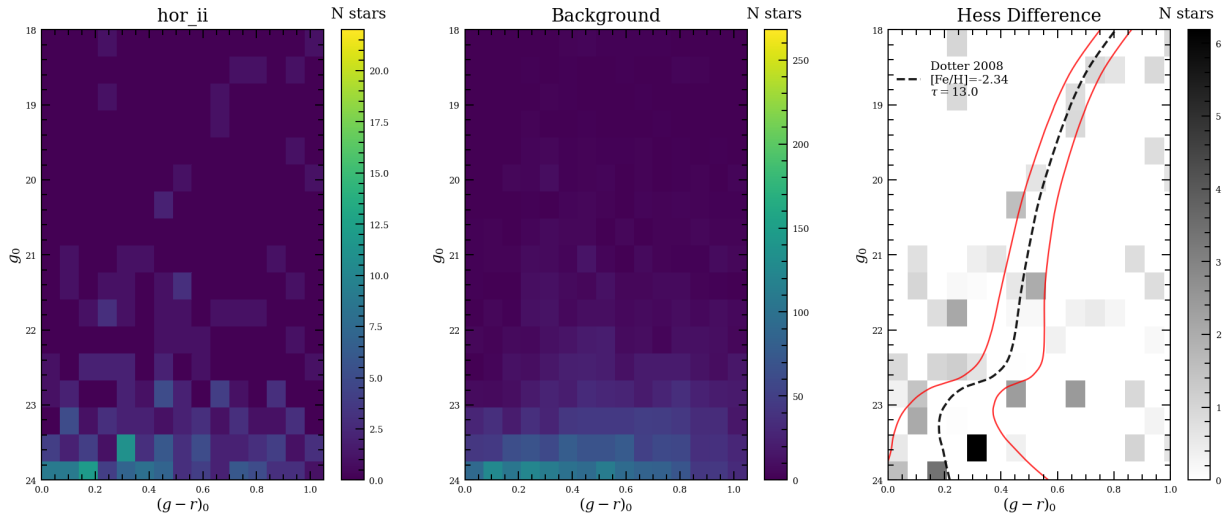

Figure A.10: A background subtracted Hess color magnitude diagram of Horologium II. This figure is similar to Figure A.1

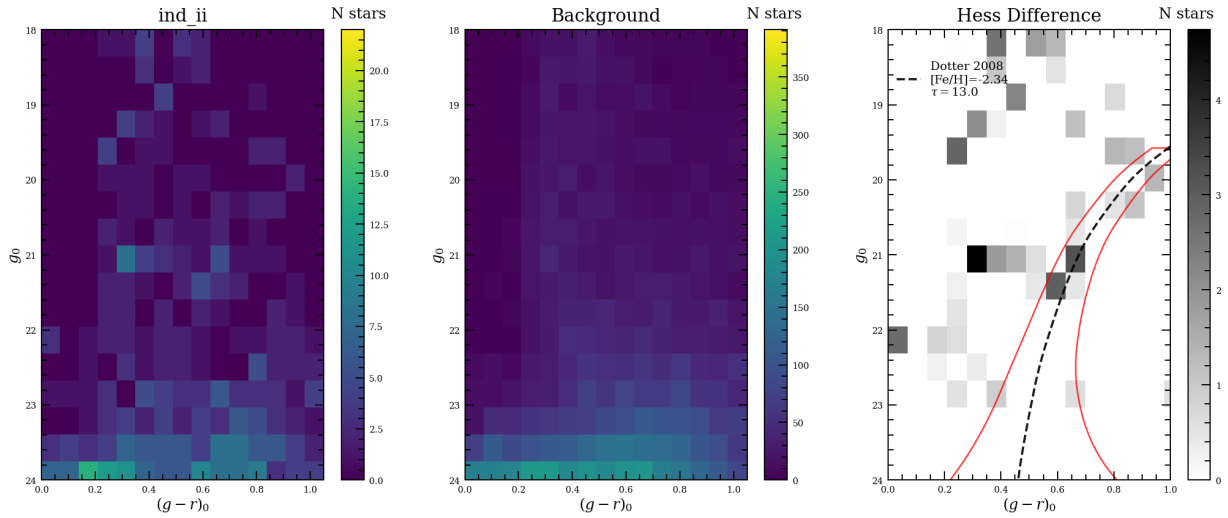

Figure A.11: A background subtracted Hess color magnitude diagram of Indus II. This figure is similar to Figure A.1

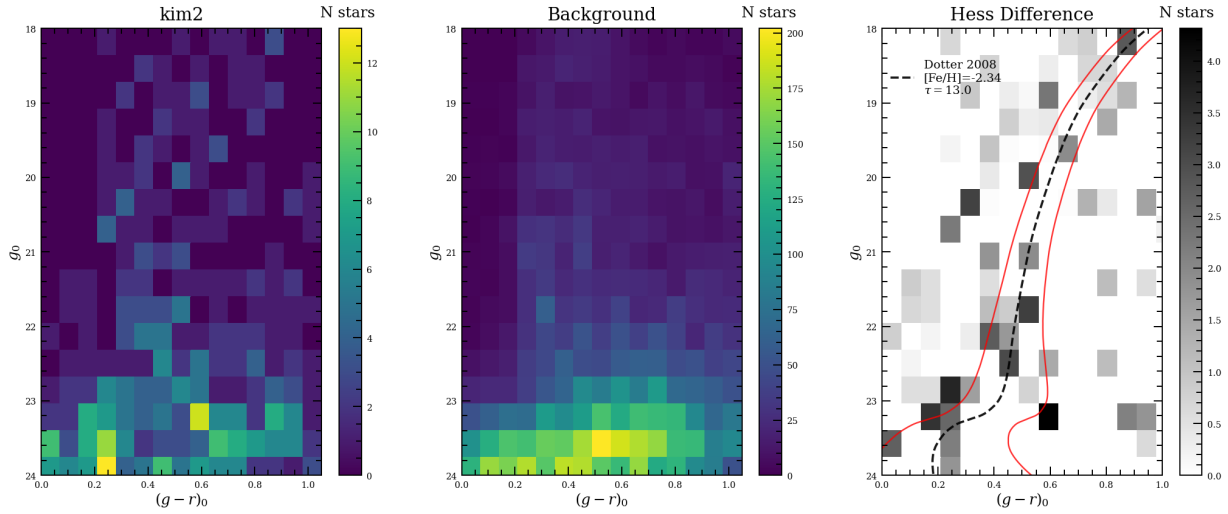

Figure A.12: A background subtracted Hess color magnitude diagram of Indus II. This figure is similar to Figure A.1

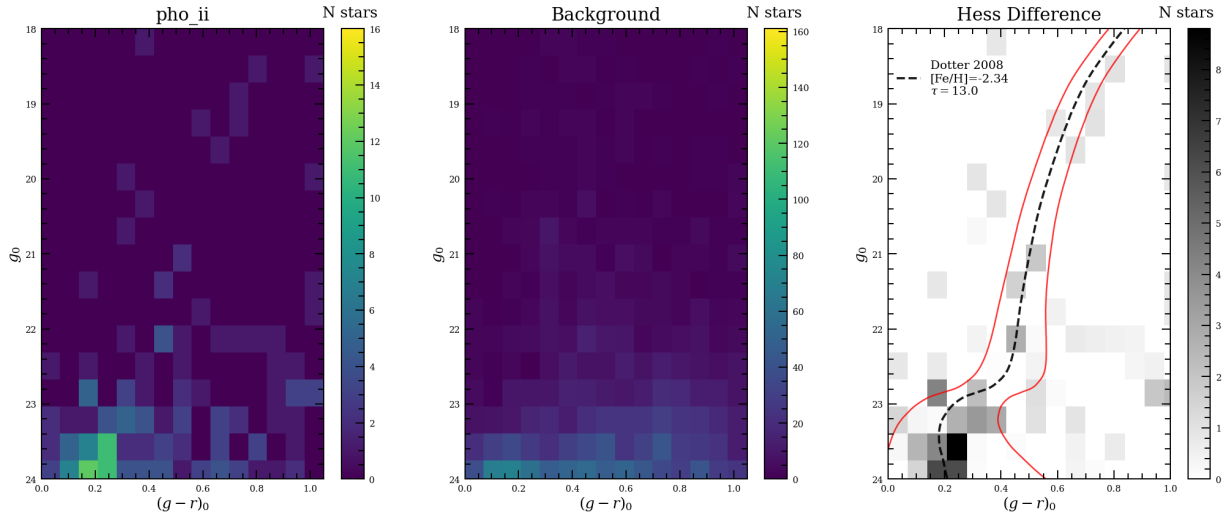

Figure A.13: A background subtracted Hess color magnitude diagram of Phoenix II. This figure is similar to Figure A.1

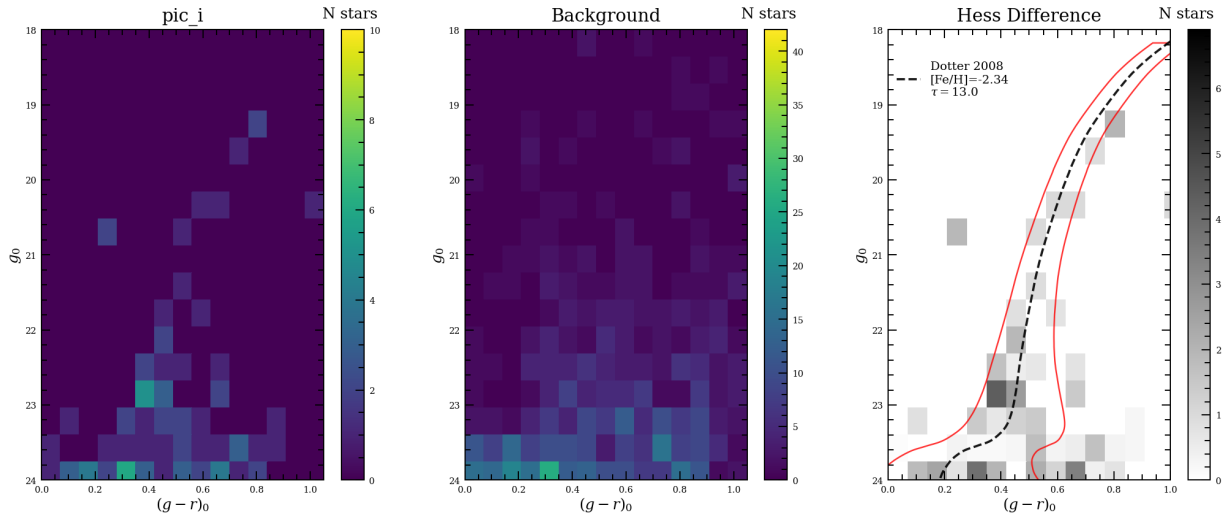

Figure A.14: A background subtracted Hess color magnitude diagram of Pictoris I. This figure is similar to Figure A.1

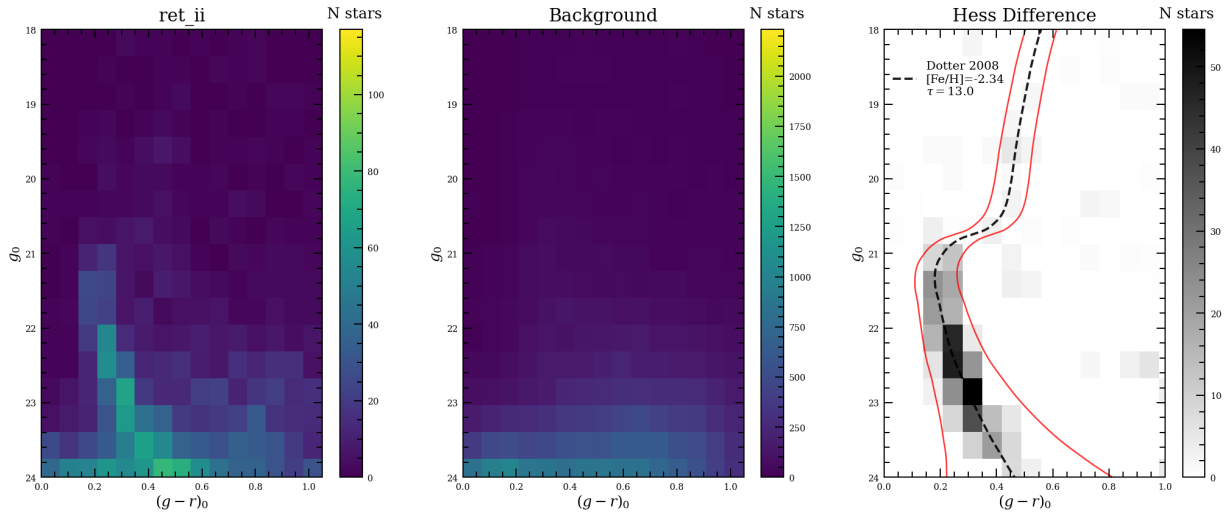

Figure A.15: A background subtracted Hess color magnitude diagram of Reticulum II. This figure is similar to Figure A.1

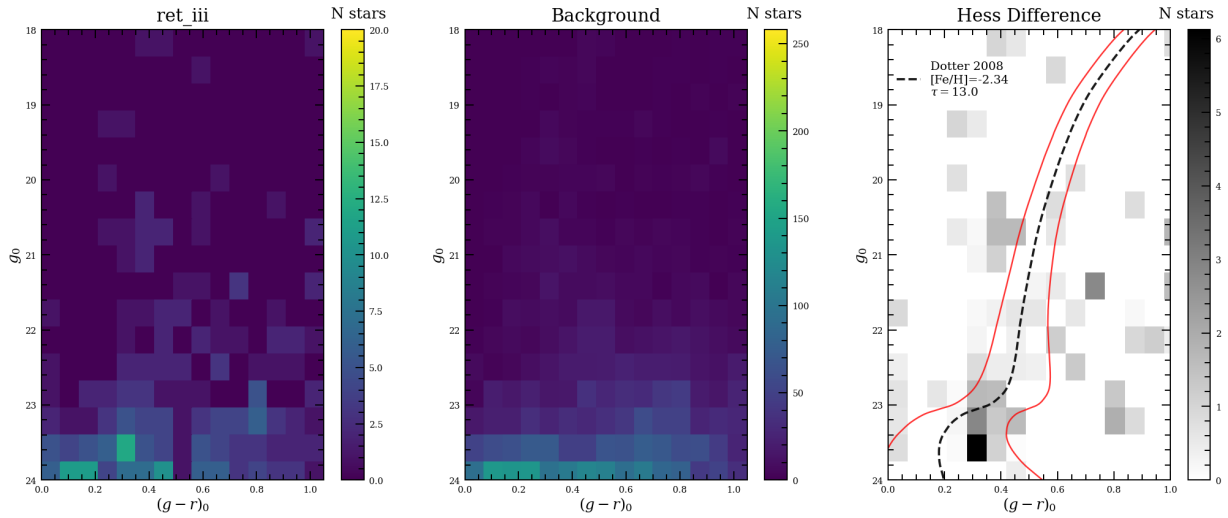

Figure A.16: A background subtracted Hess color magnitude diagram of Reticulum III. This figure is similar to Figure A.1

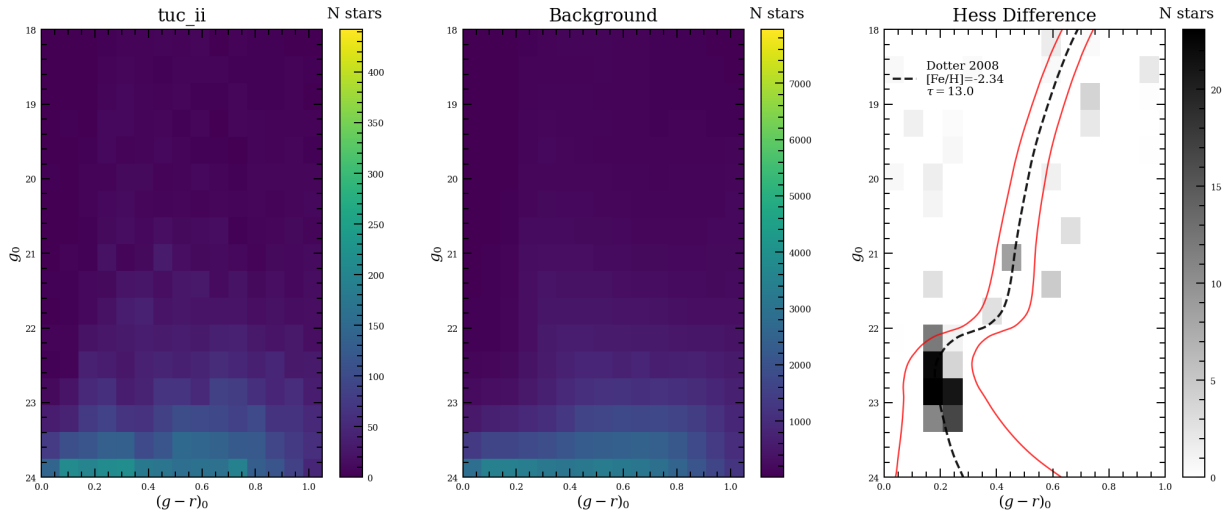

Figure A.17: A background subtracted Hess color magnitude diagram of Tucana II. This figure is similar to Figure A.1

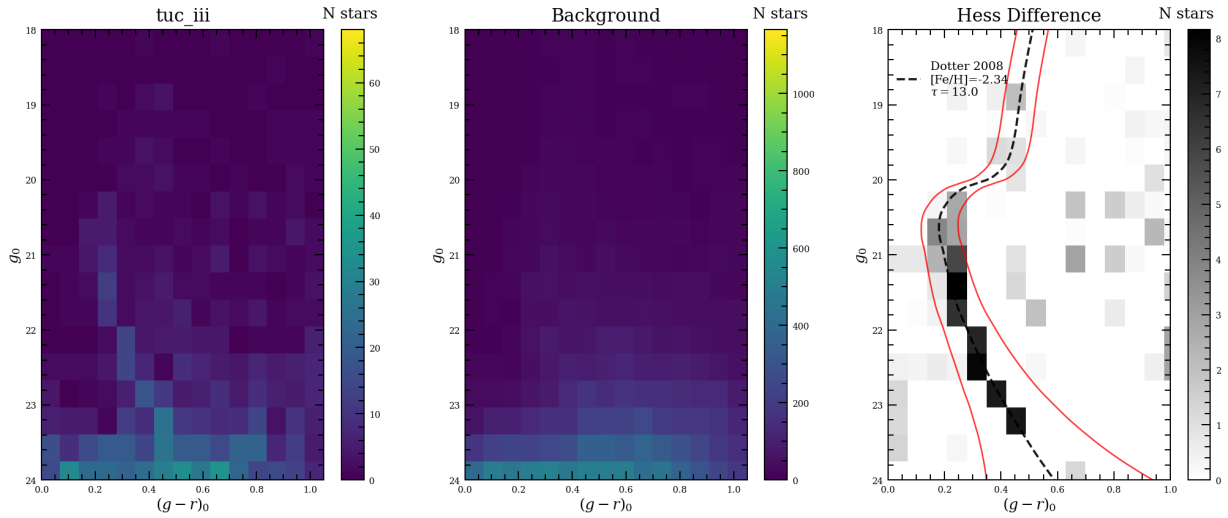

Figure A.18: A background subtracted Hess color magnitude diagram of Tucana III. This figure is similar to Figure A.1

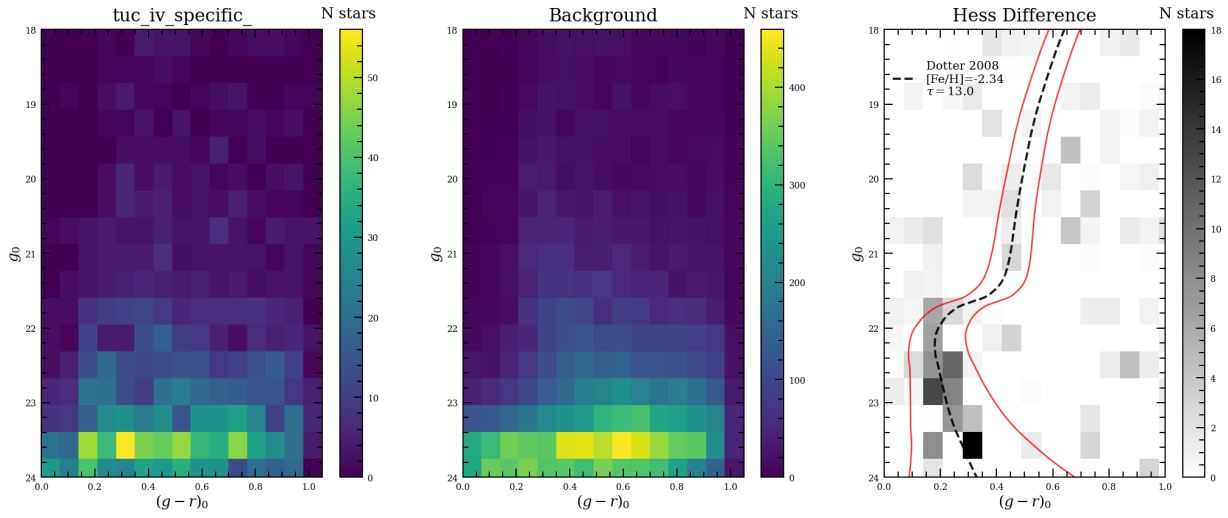

Figure A.19: A background subtracted Hess color magnitude diagram of Tucana IV. This figure is similar to Figure A.1

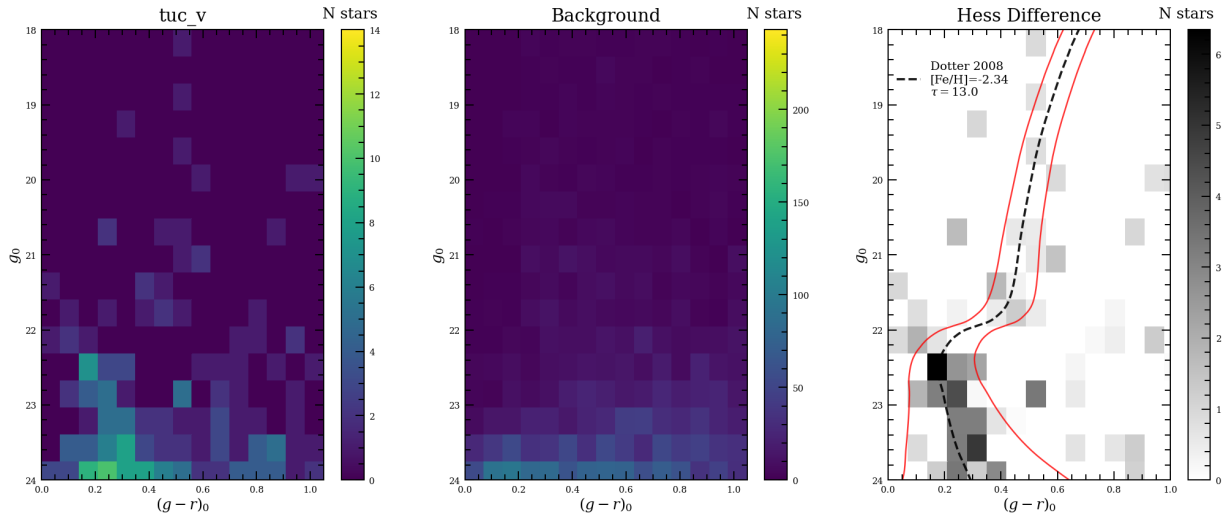

Figure A.20: A background subtracted Hess color magnitude diagram of Tucana V. This figure is similar to Figure A.1